Canada

WIND TUNNEL INVESTIGATION OF DYNAMIC STALL OF AN NACA 0018 AIRFOIL OSCILLATING IN PITCH

by

R.H. Wickens
National Aeronautical Establishment

AERONAUTICAL NOTE
NAE-AN-27
NRC NO. 24262

85-3231/

NATIONAL AERONAUTICAL ESTABLISHMENT

SCIENTIFIC AND TECHNICAL PUBLICATIONS

AERONAUTICAL REPORTS:

Aeronautical Reports (LR): Scientific and technical information pertaining to aeronautics considered important, complete, and a lasting contribution to existing knowledge.

Mechanical Engineering Reports (MS): Scientific and technical information pertaining to investigations outside aeronautics considered important, complete, and a lasting contribution to existing knowledge.

AERONAUTICAL NOTES (AN): Information less broad in scope but nevertheless of importance as a contribution to existing knowledge.

LABORATORY TECHNICAL REPORTS (LTR): Information receiving limited distribution because of preliminary data, security classification, proprietary, or other reasons.

Details on the availability of these publications may be obtained from:

Publications Section,
National Research Council Canada,
National Aeronautical Establishment,
Bldg. M-16, Room 204,
Montreal Road,
Ottawa, Ontario
K1A 0R6

ÉTABLISSEMENT AÉRONAUTIQUE NATIONAL

PUBLICATIONS SCIENTIFIQUES ET TECHNIQUES

RAPPORTS D'AÉRONAUTIQUE

Rapports d'aéronautique (LR): Informations scientifiques et techniques touchant l'aéronautique jugées importantes, complètes et durables en termes de contribution aux connaissances actuelles.

Rapports de génie mécanique (MS): Informations scientifiques et techniques sur la recherche externe à l'aéronautique jugées importantes, complètes et durables en termes de contribution aux connaissances actuelles.

CAHIERS D'AÉRONAUTIQUE (AN): Informations de moindre portée mais importantes en termes d'accroissement des connaissances.

RAPPORTS TECHNIQUES DE LABORATOIRE (LTR): Informations peu disséminées pour des raisons d'usage secret, de droit de propriété ou autres ou parce qu'elles constituent des données préliminaires.

Les publications ci-dessus peuvent être obtenues à l'adresse suivante:

Section des publications
Conseil national de recherches Canada
Établissement aéronautique national
Im. M-16, pièce 204
Chemin de Montréal
Ottawa (Ontario)
K1A 0R6

UNLIMITED
UNCLASSIFIED

WING TUNNEL INVESTIGATION OF DYNAMIC STALL OF AN NACA 0018 AIRFOIL OCSILLATING IN PITCH

ÉTUDE EN SOUFFLERIE DU DÉCROCHAGE AÉRODYNAMIQUE D'UN PROFIL NACA 0018 OSCILLANT EN TANGAGE

by/par

R.H. Wickens

National Aeronautical Establishment

AERONAUTICAL NOTE
NAE-AN-27
NRC NO. 24262

OTTAWA
FEBRUARY 1985

R.J. Templin, Head/Chef
Low Speed Aerodynamics Laboratory/
Laboratoire d'aérodynamique à basse vitesse

G.M. Lindberg
Director/Directeur

SUMMARY

This report presents aerodynamic data on an NACA 0018 airfoil oscillating in pitch in the NAE 2m X 3m Low Speed Tunnel. The purpose of the test was to simulate the dynamic aerodynamic behaviour of a Vertical Axis Wind Turbine blade section at the equatorial plane under the dynamic stall conditions which may occur at low ratios of tip speed to wind speed.

Measurements were made of wing surface pressure time histories at various chordwise locations, during a complete cycle of oscillation. The dynamic effects on nose suction pressures were seen to increase their magnitude and to delay flow breakdown to a higher angle of attack.

Integration of wing pressures furnished normal and chordwise forces during the angle of attack cycle. The behaviour of these parameters showed that dynamic stall for wing angles of attack up to 30 degrees, occurred about 5 degrees later than for the equivalent steady flow case. This phenomenon resulted in an increase in normal force of about 20% and an increase in chordwise force of about 40% when the wing is pitching to 30 degrees.

RÉSUMÉ

Le présent rapport contient des données aérodynamiques sur un profil NACA 0018 oscillant en tangage dans la soufflerie à basse vitesse de 2 m X 3 m de l'ÉAN. L'essai avait pour objet de simuler le comportement aérodynamique dynamique d'un profil de pale d'éolienne à axe vertical dans le plan équatorial dans des conditions de décrochage dynamique, lequel peut se produire à de faibles rapports de vitesse d'extrémité de pale sur la vitesse du vent.

Des mesures de pression-temps ont été prises en différents points de la corde du profil au cours d'une oscillation complète. Les effets dynamiques des pressions d'aspiration s'exerçant sur le nez du profil augmentaient alors pour retarder la détérioration de l'écoulement laminaire aux angles d'attaque supérieurs.

L'intégration des pressions s'exerçant sur le profil a donné des forces normales et qui s'exerçaient dans le sens de la corde en fonction de l'angle d'attaque. Ces paramètres ont indiqué que le décrochage dynamique pour des angles d'attaque du profil allant jusqu'à 30 degrés se produisait environ 5 degrés plus tard que dans le cas d'un profil équivalent dont l'écoulement n'était pas perturbé. Ce phénomène s'est traduit par une augmentation d'environ 20 % de la force normale et de 40 % environ de la force s'exerçant dans le sens de la corde lorsque le profil oscille jusqu'à 30 degrés en tangage.

CONTENTS

		Page
	SUMMARY	(iii)
	ILLUSTRATIONS	(v)
	SYMBOLS	(vii)
1.0	INTRODUCTION	1
2.0	CHARACTERISTICS OF UNSTEADY FLOW THROUGH THE ROTOR	1
3.0	WIND TUNNEL SIMULATION OF DYNAMIC AERODYNAMIC EFFECTS	2
4.0	THE OSCILLATING AIRFOIL EXPERIMENT	3
	4.1 Model	3
	4.2 Hydraulic Actuator	3
	4.3 Pressure Measurements	4
	4.4 Data Acquisition and Reduction	4
	4.5 Calculation of Pressure Sensitivities	5
	4.6 Sampling and Averaging of the Data	5
5.0	CALCULATION OF PRESSURE COEFFICIENTS	6
	5.1 Integration of Wing Pressure Coefficients	6
	5.2 Wing Instantaneous Lift and Drag Coefficients	6
6.0	EXPERIMENTAL RESULTS	7
	6.1 Wind Tunnel Test Program	7
	6.2 Time Variation of Tunnel Static and Dynamic Pressure	7
	6.3 Pressure Time Histories on the Wing	7
	6.4 Airfoil Instantaneous Surface Pressure Distributions	8
	6.5 Airfoil Normal and Cord Force Coefficients	9
	6.6 Comparison between Steady and Unsteady Airfoil Characteristics	10
7.0	CONCLUSIONS	10
8.0	REFERENCES	11

TABLES

Table		Page
I	Scanivalve Port Nos. and Wing Tap Co-Ordinates	13
II	Wall Pressure Locations (Relative to Wing Quarter-Chord) (North Wall)	14

ILLUSTRATIONS

Figure		Page
1	.....	15
2	.....	16
3	Time Histories of Wing Angle of Attack for Various Simulated Turbine Speed Ratios	17
4	General Arrangement of Oscillating Wing Model in the 2m X 3m Wind Tunnel	18
5	Static Pressure Locations on the Wing and Walls	19
6	Wind Tunnel Dynamic and Static Pressure Time Histories During One Cycle	20
7	Wing Pressure Time Histories, $\alpha_m = \pm 30°$, $R\Omega/V = 2$, $f = 0.55$ hz	21
8	Wing Pressure Time Histories, $\alpha_m = \pm 20°$, $R\Omega/V = 3$, $f = 0.55$ hz	22
9	Wing Pressure Time Histories, $\alpha_m = \pm 15°$, $R\Omega/V = 4$, $f = 0.55$ hz	23
10	Wing Pressure Time Histories, $\alpha_m = \pm 12°$, $R\Omega/V = 5$, $f = 0.55$ hz	24
11a	Wing Chordwise Pressures During Positive Half-Cycle, $\alpha_m = \pm 30°$, $R\Omega/V = 2$, $f = 0.55$ hz	25-27
11b	Wing Chordwise Pressures During Negative Half-Cycle, $\alpha_m = \pm 30°$, $R\Omega/V = 2$, $f = 0.55$ hz	28-30
12a	Wing Thicknesswise Pressures During Positive Half-Cycle, $\alpha_m = \pm 30°$, $R\Omega/V = 2$, $f = 0.55$ hz	31-33
12b	Wing Thicknesswise Pressures During Negative Half-Cycle, $\alpha_m = \pm 30°$, $R\Omega/V = 2$, $f = 0.55$ hz	34-36
13a	Wing Chordwise Pressures During Positive Half-Cycle, $\alpha_m = \pm 20°$, $R\Omega/V = 3$, $f = 0.55$ hz	37-38
13b	Wing Chordwise Pressures During Negative Half-Cycle, $\alpha_m = \pm 20°$, $R\Omega/V = 3$, $f = 0.55$ hz	39-40
14a	Wing Thicknesswise Pressures During Positive Half-Cycle, $\alpha_m = \pm 20°$, $R\Omega/V = 3$, $f = 0.55$ hz	41-42
14b	Wing Thicknesswise Pressures During Negative Half-Cycle, $\alpha_m = \pm 20°$, $R\Omega/V = 3$, $f = 0.55$ hz	43-44
15a	Wing Chordwise Pressures During Positive Half-Cycle, $\alpha_m = \pm 15°$, $R\Omega/V = 4$, $f = 0.55$ hz	45

ILLUSTRATIONS (Cont'd)

Figure		Page
15b	Wing Chordwise Pressures During Negative Half-Cycle, $\alpha_m = \pm 15^\circ$, $R\Omega/V = 4$, f = 0.55 hz	46
16a	Wing Thicknesswise Pressures During Positive Half-Cycle, $\alpha_m = \pm 15^\circ$, $R\Omega/V = 4$, f = 0.55 hz	47
16b	Wing Thicknesswise Pressures During Negative Half-Cycle, $\alpha_m = \pm 15^\circ$, $R\Omega/V = 4$, f = 0.55 hz	48
17a	Wing Chordwise Pressures During Positive Half-Cycle, $\alpha_m = \pm 12^\circ$, $R\Omega/V = 5$, f = 0.55 hz	49
17b	Wing Chordwise Pressures During Negative Half-Cycle, $\alpha_m = \pm 12^\circ$, $R\Omega/V = 5$, f = 0.55 hz	50
18a	Wing Thicknesswise Pressures During Positive Half-Cycle, $\alpha_m = \pm 12^\circ$, $R\Omega/V = 5$, f = 0.55 hz	51
18b	Wing Thicknesswise Pressures During Negative Half-Cycle, $\alpha_m = \pm 12^\circ$, $R\Omega/V = 5$, f = 0.55 hz	52
19	Airfoil Force Coefficients C_N, C_T, Derived from Pressure Distributions $V_T/V = 2.0$, $\alpha max = \pm 30^\circ$, f = 0.55 hz	53
20	Airfoil Force Coefficients C_N, C_T, Derived from Pressure Distributions $V_T/V = 3.0$, $\alpha max = \pm 20^\circ$, f = 0.55 hz	54
21	Airfoil Force Coefficients C_N, C_T, Derived from Pressure Distributions $V_T/V = 4.0$, $\alpha max = \pm 15^\circ$, f = 0.55 hz	55
22	Airfoil Force Coefficients C_N, C_T, Derived from Pressure Distributions $V_T/V = 5.0$, $\alpha max = \pm 15^\circ$, f = 0.55 hz	56
23	Oscillating Airfoil Lift Coefficient C_L	57
24	Octillating Airfoil Drag Coefficient C_D	58
25	Pitching Moment Coefficient about Quarter-Chord	59
26	Comparison Between Static and Dynamic Wing Pressure Distributions $V_T/V = 2.0$, $\alpha max = \pm 30^\circ$	60
27	Comparison Between Static and Dynamic Wing Pressure Distributions $V_T/V = 5.0$, $\alpha max = \pm 12^\circ$	61
28	Comparison Between Static and Dynamic Wing Normal and Chord Force Coefficients C_N, C_T, $V_T/V = 2.0$, $\alpha max = \pm 30^\circ$	62

SYMBOLS

Symbol	Definition
α	angle of attack
c	airfoil chord
C_{pa}	airfoil surface pressure coefficient
C_p	airfoil normal force coefficient
C_t	airfoil chordwise force coefficient
$C_{m\,c/4}$	airfoil pitching moment coefficient about the quarter-chord
E_i	channel output voltage (i = 1 to 6)
K_i	channel calibration factor (i = 1 to 6)
p_r	reference pressure (atmospheric)
p_a	airfoil pressure
p_s	static pressure
p_t	total pressure
p_{ws}	wall pressure (south)
p_{wn}	wall pressure (north)
R	radius of VAWT rotor
t	time
T	period of one oscillation or one rotor revolution
V	wind speed
V_t	VAWT rotor tip speed at the equator
V_b	relative airflow velocity at the equator
θ	azimuth angle of the VAWT rotor

WIND TUNNEL INVESTIGATION OF DYNAMIC STALL OF AN NACA 0018 AIRFOIL OSCILLATING IN PITCH

1.0 INTRODUCTION

In the sphere of renewable energy, wind power is considered to be one of the more appropriate ways of meeting some of the future energy needs of Canada's remote areas, and also those of underdeveloped countries. A major contribution has been made in this field by the Low Speed Aerodynamics Laboratory of the NAE, in the re-discovery and development of the Darreius Vertical Axis Wind Turbine (VAWT), and has resulted in the laboratory playing an important role in the National Wind Energy Program.

The efforts of many years work have resulted in contributions to the basic science of the VAWT, with particular reference to aerodynamic performance. Several wind turbine test installations are currently running successfully in remote parts of Canada, the largest being the 230 kw and 500 kw machines on the Magdalen and Prince Edward Islands. The results of these experiments, in which the benefits of feeding wind-generated electricity into existing hydro networks as well as the assessment of the aerodynamic characteristics of a large machine, have provided basic research and design data for future turbines. The development of an even larger turbine, on the south shore of the St. Lawrence River in Quebec is now underway, and it is expected to be in operation in 1986.

The Magdalen Islands wind turbine is of the constant speed type. The rotor, consisting of two blades, is 80 feet (24.4 m) in diameter at the equator, and 120 feet (36.6 m) high. Its rotational speed of 36 rpm approximately, results in an equatorial tip speed of about 150 ft/sec (45.7 m/sec). Figure 1 shows a view of the turbine and a typical power characteristic curve in which power coefficient C_p is plotted against speed ratio V_t/V.

The various operating ranges of the constant speed turbine are indicated by hatched areas on the power curve; best efficiency occurs in the speed ratio range between 4 and 7. In this operating range, a simple momentum theory has been found to give satisfactory agreement with experimental data, and various codes, based on the multiple stream tube theories of References (3) and (4) are now routinely used to compute rotor performance. At lower values of the speed ratio ($1 < V_t/V < 4$), the turbine is operating in an environment where the angle of attack of the blade sections are at or above static stall, and where dynamic effects, resulting from cyclic changes of airflow are at a maximum. Dynamic aerodynamic effects, particularly as they affect the airfoil chord force coefficients, are considered to have a significant effect on turbine maximum power output and the extent to which this might be true is illustrated in Figure 1, in which dynamic stall effects have been included in the theoretical predictions. At speed ratios greater than 6 the turbine power diminishes rapidly, the flow state is considered to be in a state of breakdown, and the simple axial momentum theories no longer apply.

As a result of this perceived importance of dynamic stall effects on the rotor, an experimental wind tunnel program was initiated in order to understand more fully a very complex phenomenon, and also to obtain dynamic normal and chord force data suitable for use in more advanced computational codes.

2.0 CHARACTERISTICS OF UNSTEADY FLOW THROUGH THE ROTOR

Due to the cyclic nature of the relative airflow acting at a blade section, fluctuations in both angle of attack and dynamic pressure will occur, resulting in large variations in blade sectional load. The probability of encountering these dynamic effects is high over the entire range of operation of the rotor, but maximum angles of attack occur at all speed ratios near 2 to 6 over the downwind portion of the blade cycle. The variation of angle of attack over one revolution and for various speed ratios are shown in Figure 2. At a speed ratio of 2, the maximum angle of attack is 30 degrees, and velocity fluctuates by 60%. At a speed ratio of 5, the maximum angle of attack is 12 degrees, but the

velocity variation reaches 100%. These calculations have not included any secondary effects such as those induced by the turbine wake. The configuration of the trailing vortex system downwind of the rotor is cycloidal in form and its resulting intersection with the rotating blades complicate the aerodynamic model, and may result in additional dynamic loads. A water tunnel study of a single blade vertical axis configuration confirmed in a qualitative way, the cyclic nature of the flow through the rotor, dynamic stall effects, and a region of intersection on the advancing blade side. This is also shown in Figure 2 in which a large vortex-like disturbance has been shed into the flow at the maximum angle of attack position. Due to the low Reynolds number of this investigation, it is difficult to correlate this disturbance with dynamic stall. The vortex formation does however occur once per revolution, and suggests that rapid changes of blade loading are taking place.

3.0 WIND TUNNEL SIMULATION OF DYNAMIC AERODYNAMIC EFFECTS

The problems associated with on-site measurement of fluctuating aerodynamic forces or pressures on an operational wind turbine blade were considered to be numerous and probably insurmountable with current resources and priorities. A more acceptable alternative in which the aerodynamic parameters could be more accurately controlled, was a wind tunnel test in which the dynamic aerodynamic effects on a segment of the turbine blade could be measured under quasi-two-dimensional unsteady conditions. Whether or not this technique accurately represents the real flow at the blade is open to question however, and the measurement of actual blade pressures will ultimately be required.

Accordingly it was proposed to oscillate a two-dimensional airfoil in the 2m × 3m wind tunnel in an angle of attack time history which simulates the local operational conditions at the equatorial plane. Surface pressures measured at a mid-span location would furnish information related to the chordwise loading on the blade, and also the normal and chordwise forces.

Although dynamic stall on the wind turbine occurs under conditions in which both angle of attack and dynamic pressure are changing, (as in Fig. 2) it would only be possible to simulate non-steady angle of attack variations in the wind tunnel with the tunnel speed kept constant.

Referring to Figure 2 the azimuthal variation of angle of attack and blade velocity (neglecting induced effects) are given by the following relations:

$$\text{Sin}\,\alpha = \frac{-\text{Sin}\,\theta}{[(1+\lambda^2) + 2\lambda\,\text{Cos}\,\theta]^{1/2}} \tag{1}$$

$$\frac{V_b}{V} = [(1+\lambda^2) + 2\lambda\,\text{Cos}\,\theta]^{1/2} \tag{2}$$

where $\lambda = \frac{V_T}{V}$, and V_b is the resultant flow velocity at the blade section.

The dimensionless coefficient τ is also defined which, in effect, measures the number of chord lengths of air which have passed over the blade during one revolution.

$$\tau = \frac{1}{C}\int_0^T V_b \cdot dt \tag{3}$$

where T is the period of one revolution.

In terms of the geometric parameters R/c, V_t/V, and V_b/V the time parameter τ is as follows:

$$\tau = \frac{(R/c)}{\lambda} \int_0^{\theta} \frac{V_b}{V} \, d\theta \qquad (4)$$

Equation (4) taken with Equation (1) for local angle of attack, when computed for equivalent values of the azimuth angle, gives an angle of attack time history which would have to be imposed on the wing in order to simulate the simultaneous variation of both aerodynamic parameters.

Figure 3 shows wing angle of attack time histories determined in this way for turbine speed ratios of 2, 3, 4 and 5. For the speed ratio of 2 in which the turbine is well into the dynamic stall regime, and the maximum angle of attack is 30 degrees and the distortion of the cycle is considerable when compared with a simple sine wave. Thus as the blade passes from the advancing to retreating sides of the rotor azimuth, α at first increases slowly to a maximum and then diminishes rapidly through zero and begins the negative half of the cycle. When maximum negative α is achieved at the same rapid rate the wing returns to zero at the initial slow rate.

As the speed ratio increases, maximum α decreases as also does the large difference between the slow and fast portions of the cycle.

4.0 THE OSCILLATING AIRFOIL EXPERIMENT

The experimental program consisted of the aerodynamic investigation of the instantaneous pressure and dynamic stall, due to non-steady motions in pitch, of a NACA 0018 airfoil; the wing section was two-dimensional, and spanned the floor and the ceiling of the 2m X 3m low speed wind tunnel. The angle of attack time history was periodic and approximated the azimuthal aerodynamic flow at the equatorial plane as already described in Section 3.0.

Pressures were measured on both the model and wind tunnel walls, and the time history of these pressures were recorded for locations along the chord and wall belts. The wind speed which represented the equatorial tip speed of the Magdalen Islands Turbine, was 150 ft/sec (45.7 m/sec). The wing frequency was constant at 0.55 hz.

4.1 Model

The wing section used in this experiment was the NACA 0018, and was a segment of the actual aluminum extruded blade profile as used on the Magdalen Islands VAWT. The fidelity of the profile to the standard NACA form as specified in Reference (5), was not exact. The quality of the surface finish was also below the usual standard for wind tunnel models, due spanwise waviness and striations resulting from the extrusion process.

The airfoil was mounted in a vertical plane and was free to rotate about its quarter-cord location. The lower attachment point consisted of a free bearing, located beneath the tunnel floor. The upper bearing was located on the roof turntable and supported the lever mechanism which was connected to a hydraulic drive. A general arrangement of the wing installation is shown in Figure 4.

4.2 Hydraulic Actuator

The hydraulic actuator and control system was designed by Davis Engineering Ltd. of Ottawa, and was used as a driving mechanism for the oscillatory airfoil tests. A technical description of the actuator can be found in Reference (6). The oscillatory mechanism consists of a hydraulic servo actuator, an electronic controller and a 3000 psi, 2 gpm hydraulic power pack.

The major system component is the servo-actuator which oscillates the airfoil through a lever arm attached to a shaft on the wing. This device is mounted on a bed-plate which also carries the associated reservoirs, valves and restrictors. The entire assembly is fastened to the upper external wind tunnel structure. The linear motion of the actuator is converted to rotary motion by means of the lever arm. The position of the wing pinion shaft is measured by a rotary transducer.

The servo-actuator controls the position of the airfoil and forces the hydraulic actuator to follow an externally-programmed demand signal. This is accomplished by comparing the demanded wing position with the actual position as sensed by the rotary transducer mounted in the shaft. The resultant error signal is then translated into a drive current to the servo valve; this in turn produces the appropriate hydraulic flow to the actuator, thus minimizing the wing position error.

Under the dynamic conditions required by the VAWT simulation, the hydraulic drive produced an airfoil motion which was within 1% of the demanded motion.

4.3 Pressure Measurements

Surface pressure measurements along the wing chord were made at the mid-span position. These locations are shown schematically in Figure 5 and in Table I. Each of the pressure locations, 45 in all, were connected to the header of a Scanivalve which was located within the model and rotated with it. The tubing lengths were kept to a length of about 2 to 3 feet (61 to 91.5 cm).

Since the dynamic effects of the tubing on fluctuating pressures is considered to be important in measurements such as this, a preliminary investigation was made as to possible corrections to the pressures which might be necessary. On the basis of Reference (10) and also as a result of using a dynamic signal compensator on the output voltages, it was concluded that there were no serious errors at the model frequency of this experiment.

As a result of possible unknown dynamic influences due to the wind tunnel walls, pressures were also measured on each side wall opposite the model. The location of the wall pressures is indicated in the schematic diagram of Figure 5, and also in Table II. The wall belt pressures were also connected to a Scanivalve.

In anticipation of significant fluctuations in the tunnel flow, both tunnel static and total pressures were measured separately using a standard pitot tube placed at the working section entrance plane. Again, due to expected variations in tunnel flow all pressures were referenced to atmospheric pressure taken outside the working section. This pressure P_T is on the reference side of the Scanivalve transducers. Thus flow dynamic pressure, referred to flow static pressure is determined as follows:

$$P_T - P_s = (P_T - P_R) - (P_s - P_R) \tag{5}$$

and airfoil pressure coefficient C_{pa}, also defined with respect to flow instantaneous static pressure is:

$$C_{pa} = \frac{(P_A - P_R) - (P_s - P_R)}{(P_T - P_s)} \tag{6}$$

Angle of attack was measured relative to the working section centre line. Positive α was defined as nose right (i.e. toward the south wall) when looking upstream from above (see Fig. 4).

4.4 Data Acquisition and Reduction

The electrical output from the five pressure tranducers and the rotary transformer was transcribed on to six channels of a RACAL FM tape recorder. Since the Scanivalve accesses the pressures sequentially, it was necessary to record for each of the wall locations (north and south) and the wing, a time record of pressure which was long enough to encompass several oscillation cycles.

Tunnel static pressure, total pressure and wing angle were recorded simultaneously and continuously. Thus for each of 45 wing pressure locations, and 21 wall pressure locations, a time record was produced which could be correlated with both tunnel flow conditions and wing angle.

It was necessary to calibrate each pressure channel, and this was done by connecting the working section total pressure as a reference value to port #01 on each Scanivalve. With the wing motionless and set at zero incidence, the tunnel was run at a nominal dynamic pressure of 27 psf (corresponding to 150 ft/sec (45.7 m/sec)), and the pressure signal was recorded on all five pressure channels. The actual total and static pressures relative to atmosphere, were measured independently using a Betz Manometer. Their values, for a tunnel pressure of 27 psf were 28.146 psf and 1.091 psf respectively.

Angle of attack was calibrated in a similar way by setting the wing to a known value and recording the signal transmitted by the rotary transducer on channel 6.

Following the conversion of the RACAL analogue signals to digital form, the data were processed to furnish the desired pressure and force coefficients.

4.5 Calculation of Pressure Sensitivities

Calibration of each channel transducer took place at the beginning of each run with the wing set at zero degrees. The differences between wind on and wind off portions of the time record were related to the separately measured tunnel total and static pressures already specified. Calculation of pressure sensitivities for each channel was as follows:

Channel 1 — Wall pressure (south)

$$K1 = 28.146/(E_{101} - E_{100})$$

Channel 2 — Wall pressure (north)

$$K2 = 28.146/(E_{201} - E_{200})$$

Channel 3 — Airfoil pressure

$$K3 = 28.146/(E_{301} - E_{300})$$

Channel 4 — Total pressure

$$K4 = 28.146/(E_{401} - E_{400})$$

Channel 5 — Static pressure

$$K5 = 1.091/(E_{501} - E_{500})$$

where K1, K2, K3, K4, K5 are the respective pressure sensitivities. The corresponding values of E_{n01} and E_{n00} are the wind off and wind on output voltage magnitudes, with the wing set to zero incidence.

The angle of attack sensitivity K6 was determined in a similar way.

4.6 Sampling and Averaging of the Data

During the analogue to digital processing the sampling rate was 250 per second and about 20 seconds of information, corresponding to 10 wing oscillations, was taken for each Scanivalve port position. After editing, five complete cycles in the middle of the time record were averaged to minimize any random fluctuations which might be present.

The angle of attack channel 6, was used to correlate all other channels with a known time base, since its amplitude and frequency were controlled and unchanging.

5.0 CALCULATION OF PRESSURE COEFFICIENTS

Wall pressure (south)

$$C_{pws}(t) = (K1*(E_1 - E_{100}) - (p_s - p_r))/(p_t - p_s)$$

Wall pressure (north)

$$C_{pwn}(t) = (K2*(E_2 - E_{200}) - (p_s - p_r))/(p_t - p_s)$$

Airfoil pressure

$$C_{pa}(t) = (K3*(E_3 - E_{300}) - (p_s - p_r))/(p_t - p_s)$$

where the static pressure is

$$(p_s - p_r) = K5*(E_5 - E_{500})$$

and total pressure is

$$(p_t - p_r) = K6*(E_6 - E_{600})$$

and the instantaneous flow dynamic pressure is

$$(p_t - p_s) = (p_t - p_r) - (p_s - p_r)$$

5.1 Integration of Wing Pressure Coefficients

The wing pressure coefficients for each of the 45 ports of the Scanivalve are integrated over the chordwise and thickness dimensions to give coefficients of normal force C_n, chord force C_t and pitching moment C_m. (Wing co-ordinates are listed in Table I).

Normal Force

$$C_n = \sum_{i=3}^{25} C_{pa}*dx - \sum_{26}^{47} C_{pa}*dx$$

Chord Force

$$C_t = \sum_{i=3}^{14} C_{pa}*dy - \sum_{15}^{36} C_{pa}*dy + \sum_{37}^{47} C_{pa}*dy$$

Pitching Moment (1/4 chord)

$$C_{mc/4} = \sum_{i=3}^{25} (0.25 - x)*C_{pa}*dx - \sum_{26}^{47} (0.25 - x)*C_{pa}*dx$$

5.2 Wing Instantaneous Lift and Drag Coefficients

$$C_l = C_n*\mathrm{Cos}\alpha + C_t*\mathrm{Sin}\alpha \qquad C_d = -(C_n*\mathrm{Sin}\alpha - C_t*\mathrm{Cos}\alpha)$$

6.0 EXPERIMENTAL RESULTS

6.1 Wind Tunnel Test Program

The wind tunnel test program of the Oscillating Airfoil was run at a constant nominal dynamic pressure of 27 psf; and a constant pitch frequency of 0.55 hz. A slow pitch rate was also done in order to furnish steady aerodynamic characteristics of the airfoil.

The simulation of the dynamic variation of angle of attack and resultant velocity time histories was done for turbine speed ratios of 2, 3, 4 and 5. These values correspond to maximum angles of attack above and below stall, and represent the various performance regions of VAWT operation (Fig. 1).

Measured data is presented in the form of pressure coefficients C_p at various locations on the wing and walls. These coefficients show the time history of the unsteady pressures as the wing pitches through its angle of attack program. Also constructed are the conventional chordwise and thicknesswise pressure distributions throughout the pitch cycle. These pressures when integrated, furnish normal and chord force coefficients under dynamic aerodynamic flow conditions.

The data as presented in this report is uncorrected for any of the usual blockage and flow curvature effects. The discussion of the application of conventional wind tunnel corrections in unsteady type of airfoil experiments similar to the present case can be found in Reference (7). It was suggested that although this type of corrective method can be satisfactorily applied to lift, it produces large errors in drag due to the difficulty in resolving the difference between two large quantities; namely C_n and C_t particularly near maximum lift.

In this experiment the wall pressures were measured at the same time as the wing pressures, so that the instantaneous influence of the walls could, in principle, be determined from wall signature techniques for steady flow such as those described in References (8) and (9). Unsteady wall effects even at the low frequencies of this experiment may not be quasi-steady however, and secondary flows may require further correction. Accordingly, it was thought that a complete analysis of the problem would be outside the scope of this report but could be addressed in a future investigation.

6.2 Time Variation of Tunnel Static and Dynamic Pressure

The time variation of tunnel dynamic and static pressures in the flow at the working section entrance plane is presented in Figure 6 for one cycle of oscillation. For a wing oscillation of 30 degrees corresponding to a turbine speed ratio of 2, and a wing angle of attack well beyond stall (αmax = 30) the peak to peak variation of dynamic pressure was 6% of the nominal reference value of 27 psf. The mean value of dynamic pressure appears to be elevated about 6% above the reference value. The corresponding variation of static pressure was 6% of tunnel dynamic pressure, and its mean value was also elevated well above the reference value. For a maximum angle of attack of 12 degrees ($V_t/V = 5$), variations in both tunnel dynamic and static pressures are small and their mean values are close to the reference pressures. These pressure variations and their fluctuations, particularly at angles of attack beyond stall, are probably a measure of blockage resulting from both conventional sources and oscillation effects on the tunnel average flow.

6.3 Pressure Time Histories on the Wing

The time histories of surface pressures on the wing, $C_{p\alpha}$, are presented in the form of carpet plots for the four turbine speed ratios ($V_t/V = 2, 3, 4, 5$) which were simulated in this experiment. In this form of presentation, (Figs. 7 to 10), both surfaces of the symmetrical airfoil pressures (i.e. north and south) are presented and the time histories for each port are offset so as to illustrate the progression of unsteady aerodynamic effects along the airfoil chord. The time base represents one complete cycle of oscillation.

Figure 7 shows pressure distributions for $V_t/V = 2$ ($\alpha max = 30$). Under static conditions with the wing fixed at 30 degrees, the flow would be completely separated, with high negative pressures appearing only over a small portion of the rounded nose. This figures shows, however that the negative peak pressures are much larger in magnitude under dynamic conditions than those for fixed incidence, and that these pressures are maintained at a high level well aft of the nose until close to maximum angle of attack. This suggests that flow breakdown and stall is delayed under dynamic conditions. Surface pressures on the rear portions of the airfoil after flow breakdown has occurred correspond to ambient static pressure although their time histories indicate a negative pressure peak close to maximum angle of attack. Without an extensive flow investigation it is difficult to explain this suction pressure on the rear of the airfoil; the effect of separated flow on the end walls, could be important in this regard, producing strong vortex-induced velocities acting on the rear of the airfoil.

The time history of pressures near the nose of the airfoil during the slow portion of the cycle, indicates a rapid rise in negative pressure which peaks just before αmax. Beyond αmax pressure falls rapidly, as angle of attack decreases during the fast portion of the cycle and flow recovery is re-established on the suction side of the airfoil. As the wing incidence passes through zero and becomes negative, the pressures reverse sign reaching a maximum positive value of 1.0 as stagnation pressure is encountered.

It can be seen from the time histories that pressures near the nose experience two maxima in both suction and positive pressure levels as they pass alternately through regions of maximum surface velocity and stagnation respectively.

As the maximum angle of attack decreases (increasing speed ratio), the pressure peaks near the nose of the airfoil gradually decrease in magnitude but still exhibit the double maxima as the stagnation point oscillates from side to side. Suction pressure is also maintained further along the wing chord, indicating that the flow separation is confined mainly to the trailing edge region. In Figure 10 for example, $\alpha max = 12$, the variation of suction pressure on the forward portion of the airfoil reaches maximum values of 4.0; a value close to that of the fixed airfoil.

6.4 Airfoil Instantaneous Surface Pressure Distributions

Figures 11 and 12 show the chordwise and thicknesswise pressure distributions on the surface of the airfoil at a number of angle of attack positions during a complete cycle of oscillation. In Figure 11, $V_t/V = 2$, $\alpha max = 30$, the pressure distributions show the development of leading edge suction, lift and flow breakdown as the airfoil pitches slowly to maximum positive incidence, and then returns quickly through zero to maximum negative incidence, followed by slow return to zero.

The chordwise pressures represent aerodynamic flows at all of the speed ratios and illustrate the effect of maximum pitch incidence on growth of lift and, in particular, the development of flow separation and reattachment.

Pressure coefficients plotted across the thickness of the airfoil are shown in Figure 12. These graphs illustrate clearly the origin of the leading suction force and its growth with incidence. The magnitude of the net force acting along the wing chord is determined from the differences between the positive and negative loops in the pressure diagrams of Figure 12. This is illustrated diagrammatically as follows.

At zero incidence the area of the positive loops, which produce an upwind force, approximately balance the negative loop of positive pressures which act at the nose, and result in a downwind or drag force. The net drag at zero incidence is determined by this balance of pressures and the skin friction drag which is normally determined by wake traverse.

As incidence increases the area of the positive pressure loop, composed of those pressures originating on the suction side of the wing, increases steadily, and result in a large upwind pressure force. This force is still active after the wing has stalled due to the fact that the oncoming flow which has impinged on the leading edge and is still able to negotiate the nose curvature without separating. This phenomenon is considerably enhanced under dynamic conditions and the behaviour of the unsteady leading edge boundary layer is presumably a key factor in the understanding of airfoil dynamic stall. At a maximum incidence of 30 degrees, the suction pressures are still active and a net upwind force exists, although much diminished.

When the airfoil pitches to a smaller maximum incidence, corresponding to higher speed ratios, it does not experience a complete stall and the dynamic characteristics were not noticeably different from those of steady flow. The leading edge pressures embodied in the positive loop of the pressure diagram produce an upwind force which also prevails after flow breakdown has occurred on the airfoil (Figs. 15 to 18).

6.5 Airfoil Normal and Chord Force Coefficients

Figures 19 to 22 show the behaviour of airfoil normal and chord force coefficients derived from integration of the instantaneous chordwise and thicknesswise pressures. The maximum values of C_n and C_t depend upon the maximum angle to which the wing pitches. For a speed ratio of 2(αmax = 30), C_{nmax} occurs, nears 18 degrees and has a value of 1.38. The corresponding value of C_{tmax} is 0.4. Both values of C_n and C_t are considerably higher than the equivalent steady values, due to dynamic stall effects.

The normal and chord force coefficients shown in Figure 19 exhibit characteristics of both hystereses and non-symmetry which are not present in the same form in the steady airfoil characteristics. There is no satisfactory explanation for this vehaviour at this time. The normal and chord force characteristics for smaller maximum angles of pitch (higher speed ratios) produce lower values of C_n and C_t, and do not exhibit the significant hysteresis and non-symmetry of the stalled airfoil.

Figures 23 and 24 show the airfoil instantaneous lift and drag coefficients derived from the integrated pressure forces and plotted against incidence. The wing achieved a maximum C_l of 1.4 at an angle of attack of 20 degrees (αmax = 30). This may be compared favourably with a steady value of 1.16 in which the wing stalls at 15 degrees. At a lower value of maximum incidence (αmax = 12, Fig. 23b), C_{lmax} = 1, and the lift curve exhibits almost no hysteresis. The lift slope for a maximum angle of 12 degrees was 0.08 per degree. The lift slope for αmax = 30 in which dynamic stall occurred, was on the average, less than for the unstalled case pitching to a maximum angle of 12 degrees.

The drag coefficient C_d is plotted in Figure 24 for maximum pitch angles above and below stall (αmax = 30 and 12). Drag increases rapidly with incidence and when the airfoil is stalled, but has a lower value on the fast return portion of the pitch cycle, thus corresponding to the hysteresis in lift. Drag at zero incidence is not believed to be accurately determined in this experiment, however a value as determined from wake measurements with the wing fixed is C_{do} = 0.01.

Wing pitching moment coefficient (about wing quarter-chord), is plotted in Figure 25 for maximum wing pitch angles of 30 and 12 degrees respectively. Positive moment is in the direction of increasing angle of attack. The pitching moment curve in Figure 25a, α = 30 degrees, exhibits neutral stability between plus and minus 15 degrees. When the wing is stalled and at angles greater than 25 degrees, a large negative moment exists and some hysteresis is present. The general shape of the moment characteristic is anti-symmetric, but less so in the negative angle range (see also the C_n and C_t curves, Fig. 19).

At smaller maximum angles below stall the pitching moment is quite small, but still exhibits a slight anti-symmetry with larger values in the negative angle range. The large negative moments which occur after stall have been attributed to free vortices which have been shed regularly from the leading edge and pass over the aft portions of the chord. This increases local loading and causes the wing to pitch down. The vortices are also related to the augmentation of both lift and drag during the dynamic stall phase. These large negative moments are also present under steady flow conditions, as shown in Figure 25a.

6.6 Comparison between Steady and Unsteady Airfoil Characteristics

Measurements of airfoil section pressures under steady flow conditions were made in a separate experiment. Figure 26a shows at an angle of attack of 20 degrees, a comparison between a steady chordwise pressure distribution and a dynamic chordwise pressure distribution when the airfoil was pitching to αmax = 30 degrees. The increase of maximum suction pressure at the nose was from 4.0 to 7.0. Similarly the positive loop in Figure 26b indicates a considerable increase in the upwind suction force at this incidence.

Similar graphs for the unstalled airfoil (αmax = 12) show a much more modest increase in suction pressure at due to dynamic effects at the incidence for maximum lift (Fig. 27).

The integrated values of C_n and C_t may also be compared. The steady value of C_n is not too different from the corresponding dynamic value except after stall occurs. The dynamic effects seem to produce a much larger hysteresis and asymmetry. In the case of the leading edge force C_t the difference between static and dynamic load is larger and the asymmetry between positive and negative angular ranges is much more pronounced (Fig. 28).

7.0 CONCLUSIONS

The following conclusions can be made regarding the data presented for the NACA 0018 airfoil oscillating in pitch to various maximum angles of attack. The purpose of the test was two-fold: (a) to simulate the dynamic aerodynamic behaviour of a VAWT blade section at the equator in a quasi-two-dimensional flow environment, and (b) to investigate the characteristics of the airfoil under dynamic stall conditions which occur at turbine speed ratios (V_t/V) of 3 or less.

Measurements were made of wing surface pressures and flow static and total pressures, relative to a fixed atmospheric reference. The time histories of one complete cycle of oscillation were obtained from the average of five cycles of data. Pressure coefficients were computed and integrated to give normal and chordwise force coefficients.

1) The pressure time histories on the wing were characterized by intervals of high suction pressure which occurred twice per cycle near the nose as the wing oscillated from side to side. These twin pressure peaks which occurred on both sides of the airfoil diminished to a single configuration as the chordwise stations further rearward experience suction only once per cycle.

2) Dynamic stall occurred near an angle of attack of 20 degrees when the wing was pitching to αmax = 30 degrees. The normal stalling angle under steady flow conditions at the same Reynolds number was 15 degrees. Nose suction hung on for some time after flow breakdown and complete separation did not occur even at 30 degrees incidence as evidenced by the high suction peaks at the nose. There was no clear evidence from the wing pressure time history carpets, of a pressure wave induced by a free vortex travelling downwind over the chord of the wing.

   At angles of attack, which under steady flow conditions would not produce stalling, the wing pressures are not significantly increased by the dynamic motion of the airfoil although the suction peaks at the nose were maintained.

3) Integrated values of the wing normal and chordwise force show that dynamic stall occurs much later than for steady flow resulting in an increase of normal force of about 20% and an increase in chordwise force of about 40%, when the wing is pitching to 30 degrees.

When the wing was pitched to maximum angles of attack well beyond the steady stalling angle, a considerable degree of hysteresis was present. This characteristic diminished with maximum angle of attack, and was not present for angles of attack below stall.

4) Observation of the instantaneous chordwise and thicknesswise pressure distributions show how the growth of both the normal and chordwise components of wing force originate, and a comparison with steady flow pressures indicates that the increase of leading edge suction pressure is about 50% when the wing is pitching to a maximum angle of 30 degrees. At lower maximum pitch angles, particularly below steady stall, the dynamic effects on suction pressure are small.

5) The data were not corrected for blockage or flow curvature effects, although the measurement of the instantaneous wall pressures were obtained, and may allow further investigation of this complex subject.

The variation of flow dynamic pressure when the wing was pitching to a maximum angle of 30 degrees, was about 6% of the mean value which itself was elevated the same amount above the (so-called) empty tunnel value. This elevation and variation of dynamic pressure was attributed to a blockage effect probably dynamic in orifin and which diminished with reduced airfoil maximum pitch angle.

8.0 REFERENCES

1. South, P.; Watts, A. — *Operational and Economic Status and Requirements of Large Scale Wind Systems.* Magdalen Islands Field Test. Paper presented at the US Department of Energy workshop, Monterey, California, March 1979.

2. Rangi, R.S.; South, P. — *Wind Power and the Vertical-Axis Wind Turbine Developed at the National Research Council.* Quarterly Bulletin No. DME/NAE 1974(2), National Research Council Canada, Ottawa.

3. Templin, R.J. — *Aerodynamic Performance Theory for the NRC Vertical-Axis Wind Turbine.* NAE Laboratory Technical Report LTR-LA-160, National Research Council Canada, Ottawa.

4. Klimas, P.C. — *Darreius Rotor Aerodynamics.* Transactions of the ASME Journal of Solar Energy Engineering Vol. 104, May 1982.

5. Abbot, I.H. — *Theory of Wing Sections.* Dover ed., 1959.

6. Reference manual for the Wind Tunnel Actuator and Servo-Actuator. Davis Engineering Ltd., Ottawa, Ont.

7. McAllister, K.W.; Carr, L.W.; McCroaky, W.J. — *Dynamic Stall Experiments on the NACA 0012 Airfoil.* NASA TP 1100.

8. Hackett,J.E.
Wilsden, D.J.
Stevens, W.A.
Pressure Signature and Other Tunnel Constraint Correction Methods for High Angle of Attack Tests.
AGARD FDP subcommittee on wind tunnels and testing techniques, Chattanooga, Tenn., USA, 1980.

9. Mokry, M.
Chan, Y.Y.
Jones, D.J.
Ohman, L.H.
Two-Dimensional Wind Tunnel Wall Interference.
AGARD AG-281.

10. Irwin, H.P.A.H.
Cooper, K.R.
Correction of Distortion in Fluctuating Pressure Measurements.
NAE Laboratory Technical Report LTR-LA-222, National Research Council Canada, Ottawa.

TABLE I

SCANIVALVE PORT NOS. AND WING TAP CO-ORDINATES

Port No.	Wing Co-Ordinate x/c	y/c
0		
1	Atmospheric - Reference	
2	Total Pressure	
3	0.946	-0.0131
4	0.883	-0.0226
5	0.821	-0.0367
6	0.759	-0.0462
7	0.698	-0.0560
8	0.635	-0.0642
9	0.573	-0.0718
10	0.511	-0.0780
11	0.463	-0.0821
12	0.405	-0.0860
13	0.343	-0.0884
14	0.298	-0.0900
15	0.256	-0.0895
16	0.215	-0.0868
17	0.174	-0.0830
18	0.122	-0.0740
19	0.098	-0.0690
20	0.077	-0.0635
21	0.057	-0.0565
22	0.038	-0.0480
23	0.0196	-0.0350
24	0.0063	-0.0170
25	0	0
26	0.0063	0.0170
27	0.0196	0.0350
28	0.038	0.0480
29	0.057	0.0565
30	0.077	0.0635
31	0.098	0.0690
32	0.122	0.0740
33	0.174	0.0830
34	0.215	0.0868
35	0.256	0.0895
36	0.298	0.0900
37	0.343	0.0884
38	0.405	0.0860
39	0.463	0.0821
40	0.511	0.0780
41	0.573	0.0718
42	0.635	0.0642
43	0.698	0.0560
44	0.759	0.0462
45	0.821	0.0367
46	0.883	0.0226
47	0.946	0.0131

TABLE II

WALL PRESSURE LOCATIONS (RELATIVE TO WING QUARTER-CHORD) (NORTH WALL)

Port No.	xw/c
3	-2.58
4	-1.92
5	-1.59
6	-1.26
7	-0.93
8	-0.60
9	-0.27
10	+0.06
11	0.39
12	0.72
13	1.05
14	1.38
15	1.71
16	2.04
17	2.37
18	2.70
19	3.03
20	3.36
21	3.69

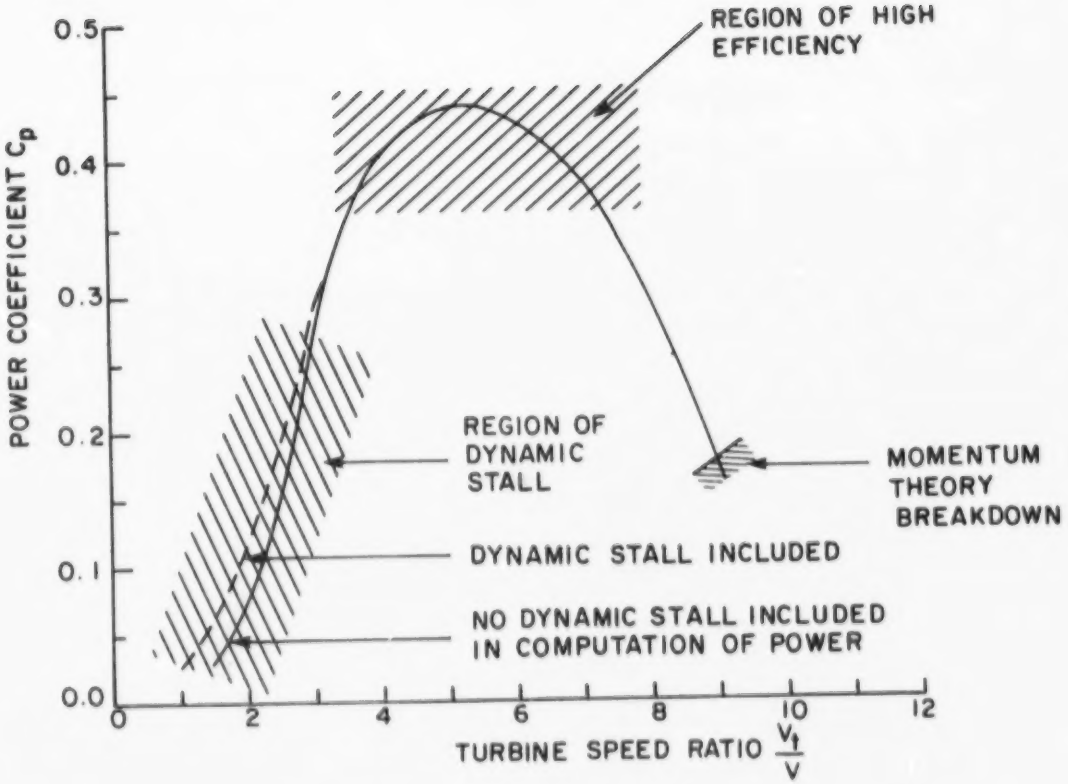

(a) WIND TURBINE POWER CHARACTERISTICS

(b) TURBINE INSTALLATION – MAGDALEN ISLANDS

FIG. 1

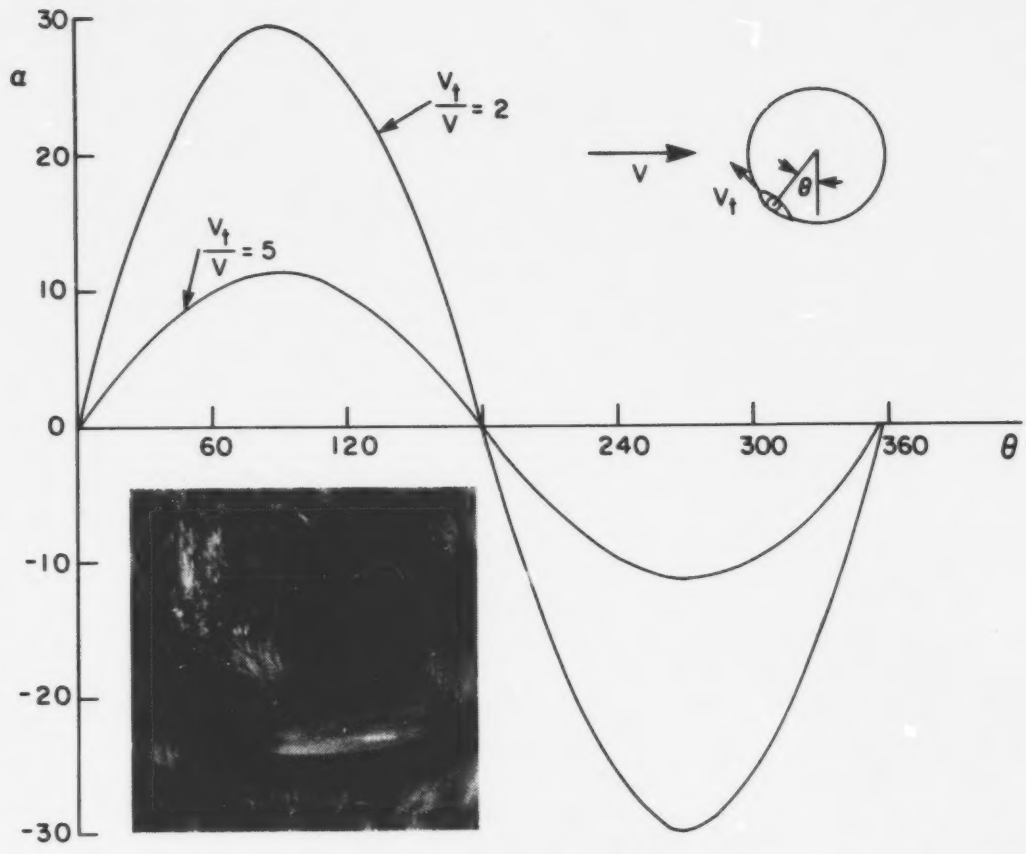

(a) ANGLE OF ATTACK OF THE BLADE ELEMENT

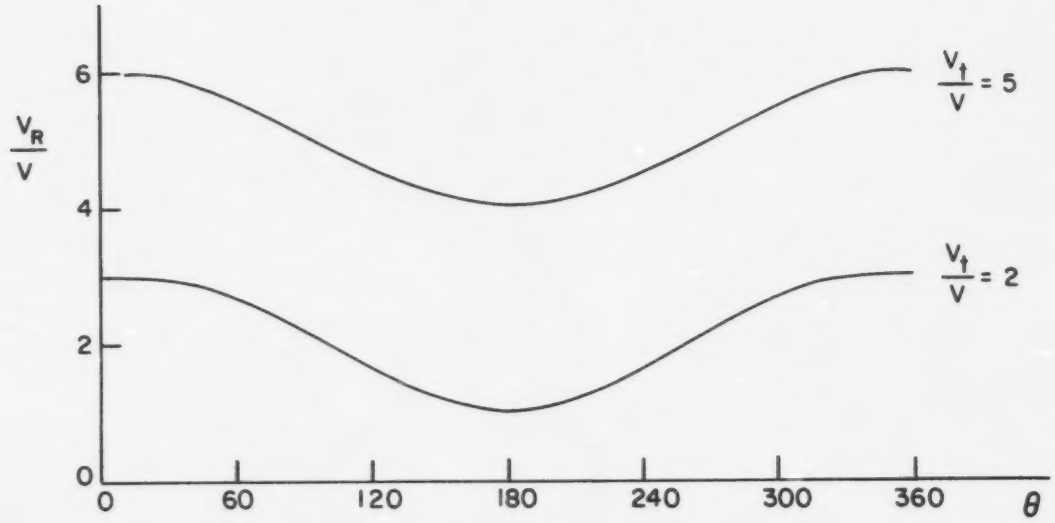

(b) RESULTANT VELOCITY AT THE BLADE ELEMENT

FIG. 2

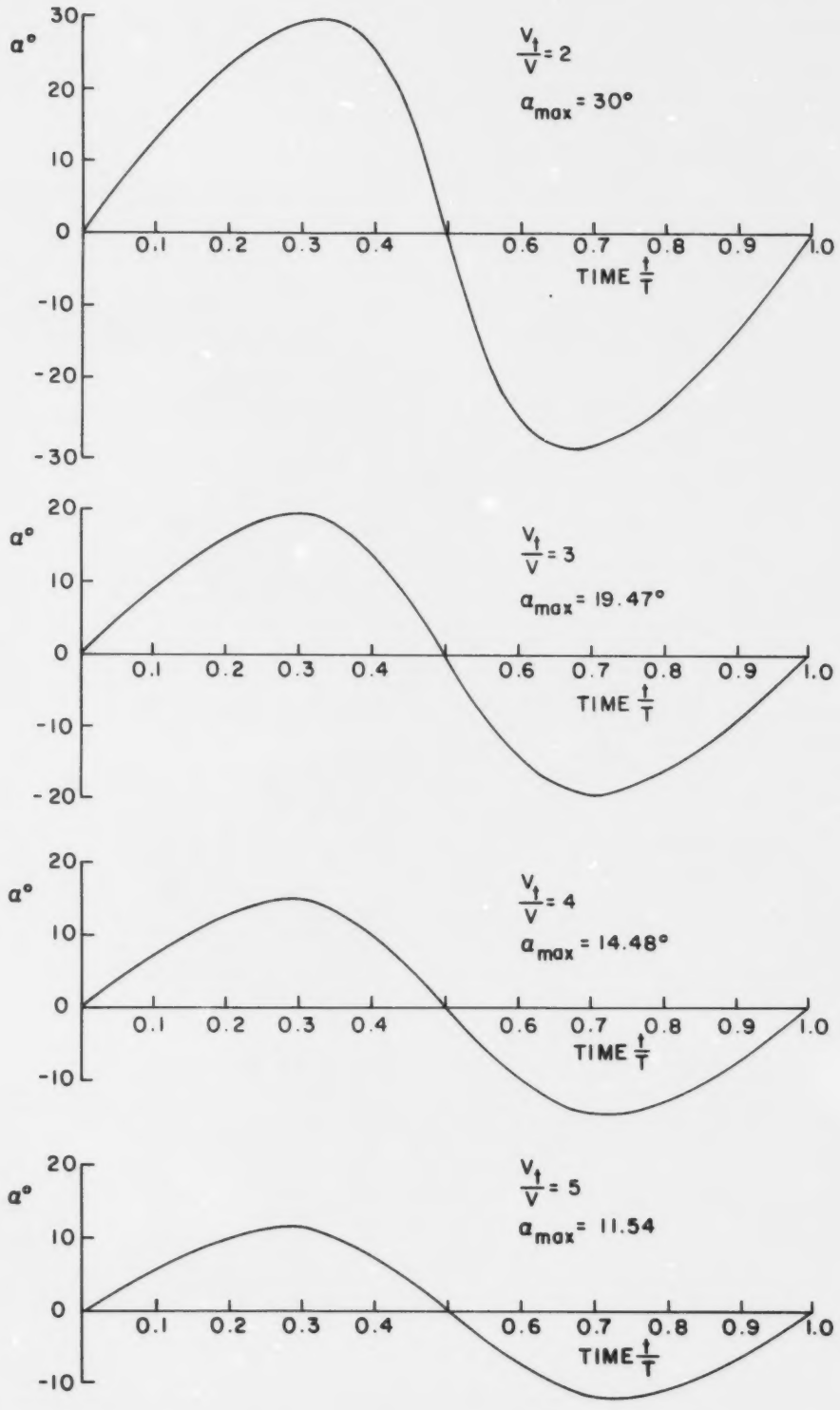

FIG. 3: TIME HISTORIES OF WING ANGLE OF ATTACK FOR VARIOUS SIMULATED TURBINE SPEED RATIOS

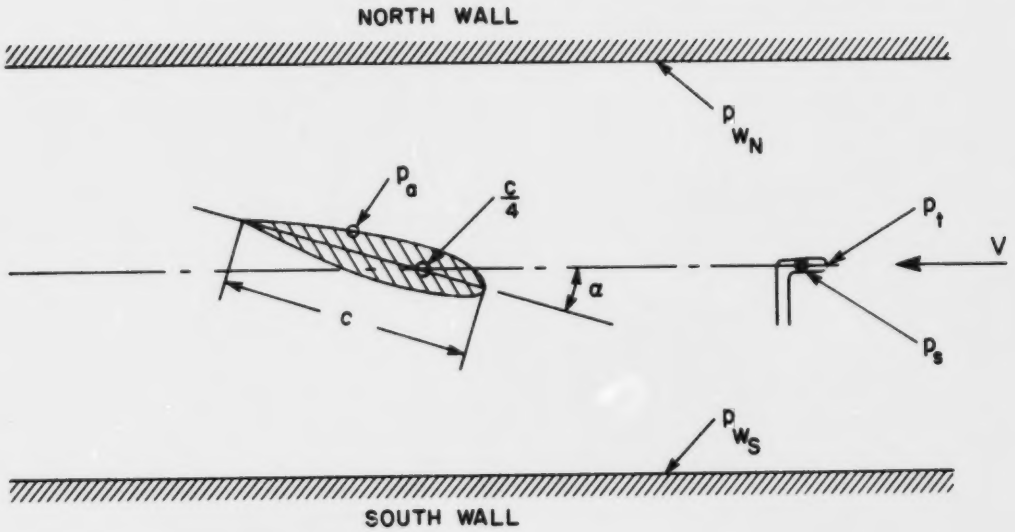

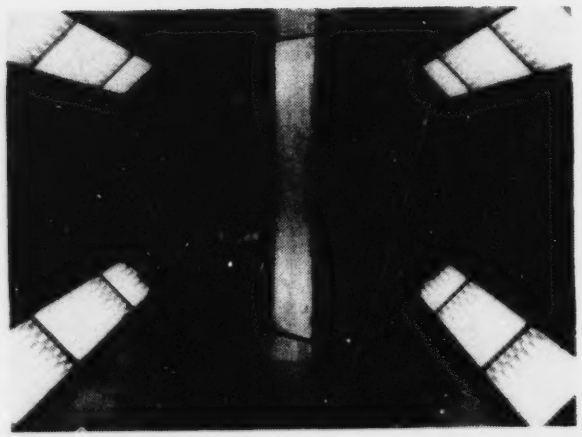

(a) WING INSTALLATION IN 2m X 3m TUNNEL

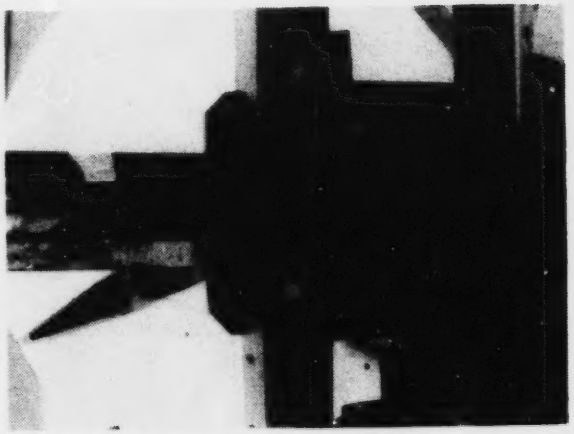

(b) OSCILLATION MECHANISM

FIG. 4: GENERAL ARRANGEMENT OF OSCILLATING WING MODEL IN THE 2m X 3m WIND TUNNEL

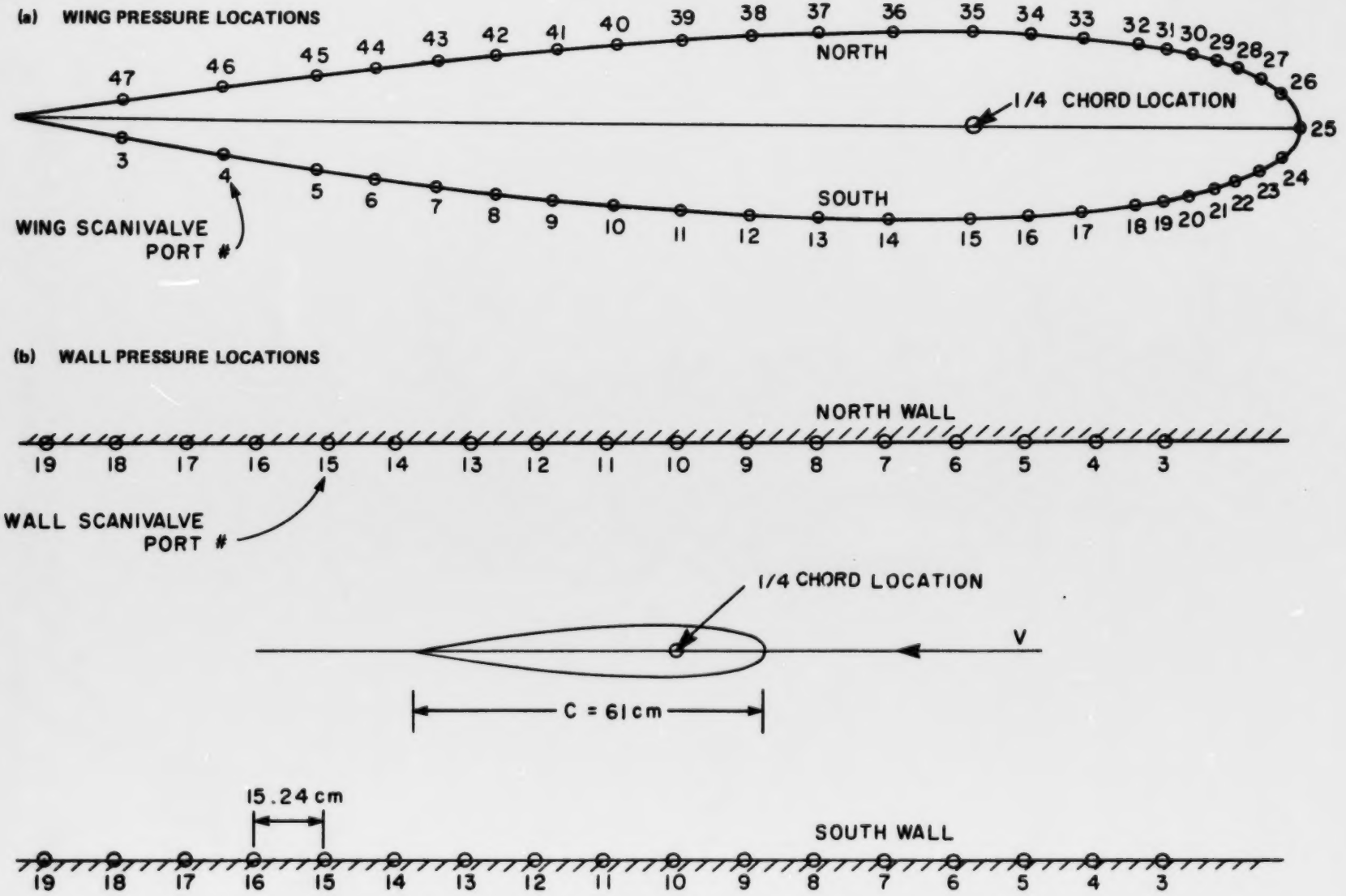

FIG. 5: STATIC PRESSURE LOCATIONS ON THE WING AND WALLS

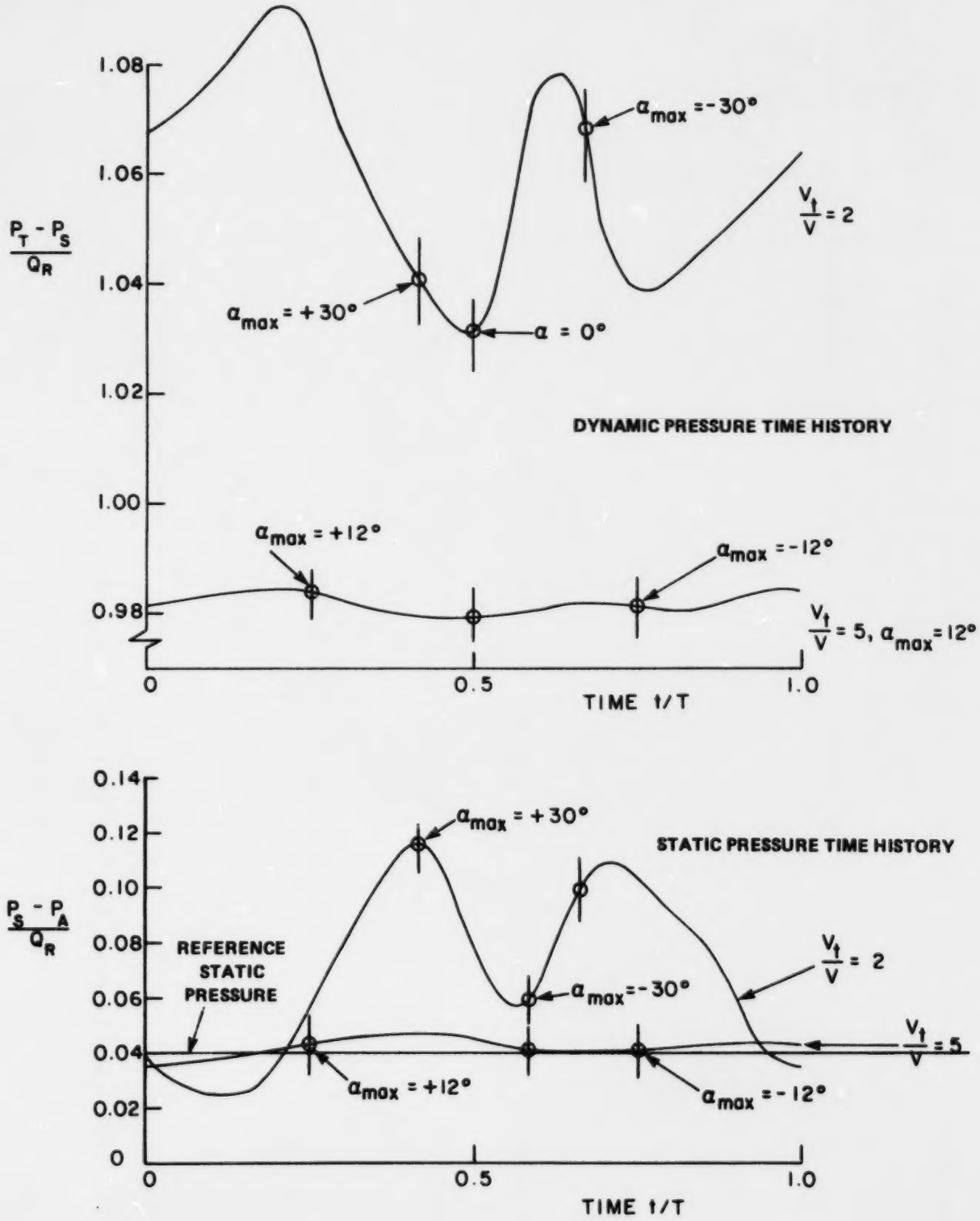

FIG. 6: WIND TUNNEL DYNAMIC AND STATIC PRESSURE TIME HISTORIES DURING ONE CYCLE

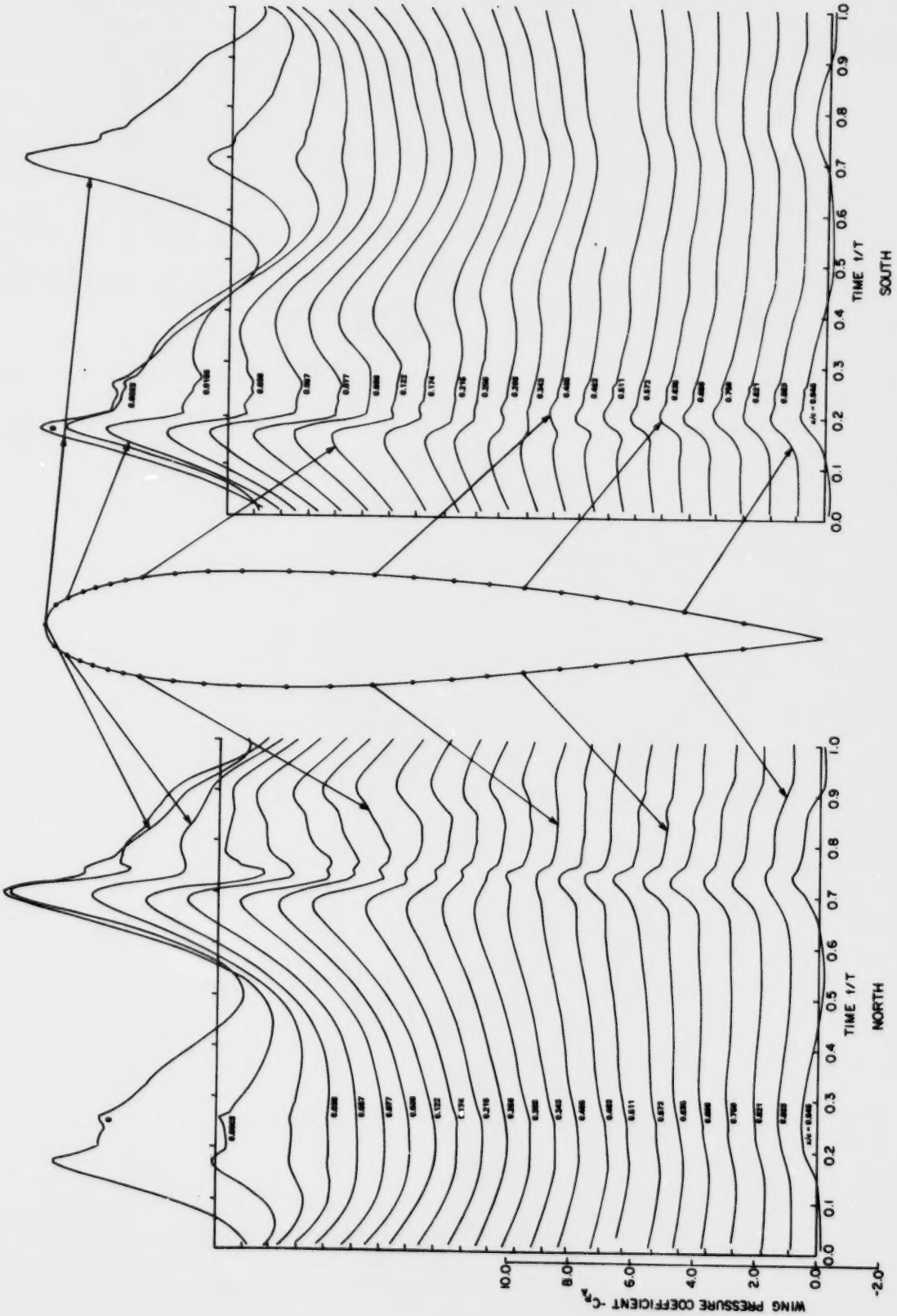

FIG. 7: WING PRESSURE TIME HISTORIES, $\alpha_m = \pm 30°$, $\frac{R\Omega}{V} = 2$, f = 0.55 hz

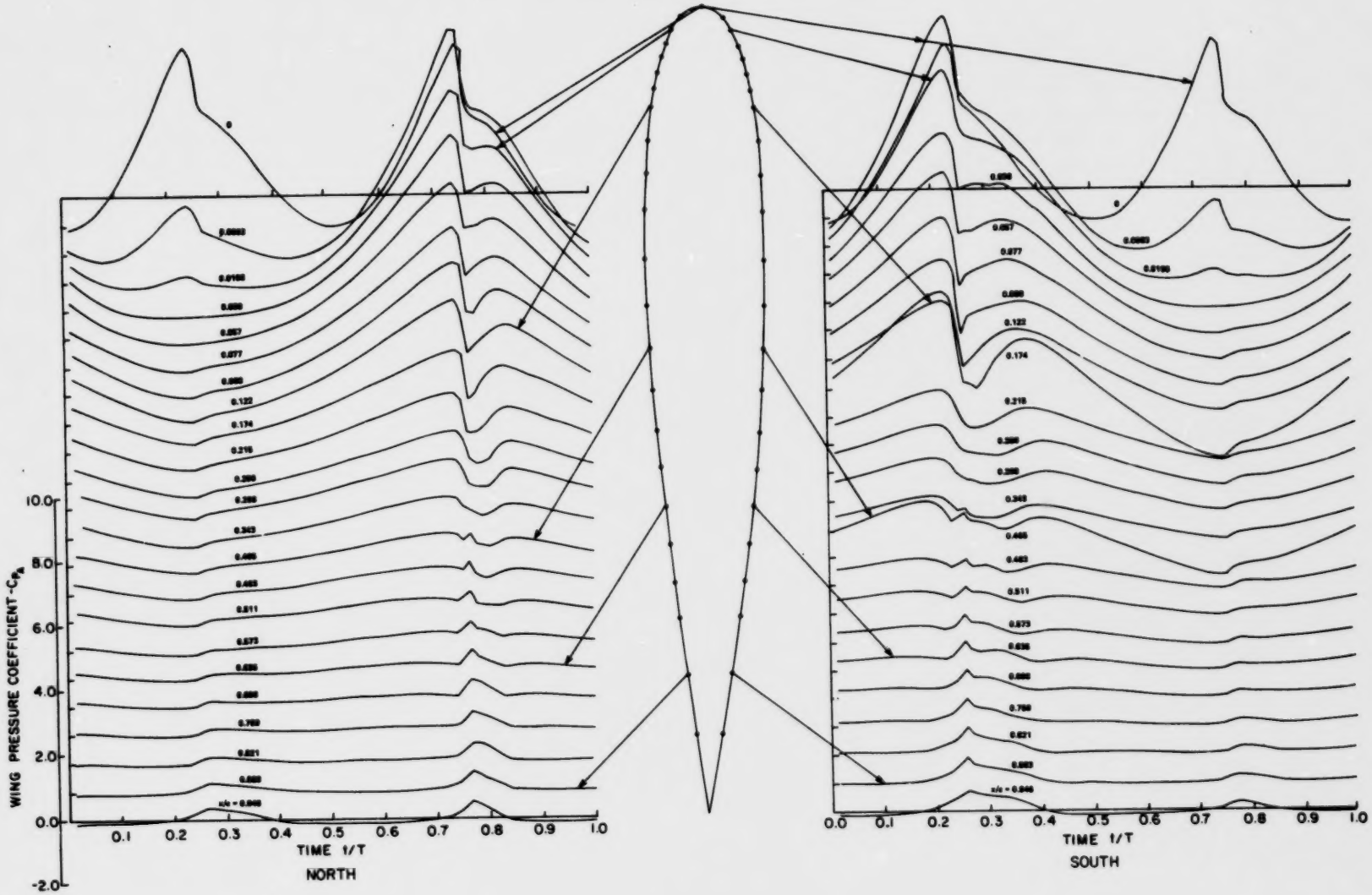

FIG. 8: WING PRESSURE TIME HISTORIES, $\alpha_m = \pm 20°$, $\frac{R\Omega}{V} = 3$, f = 0.55 hz

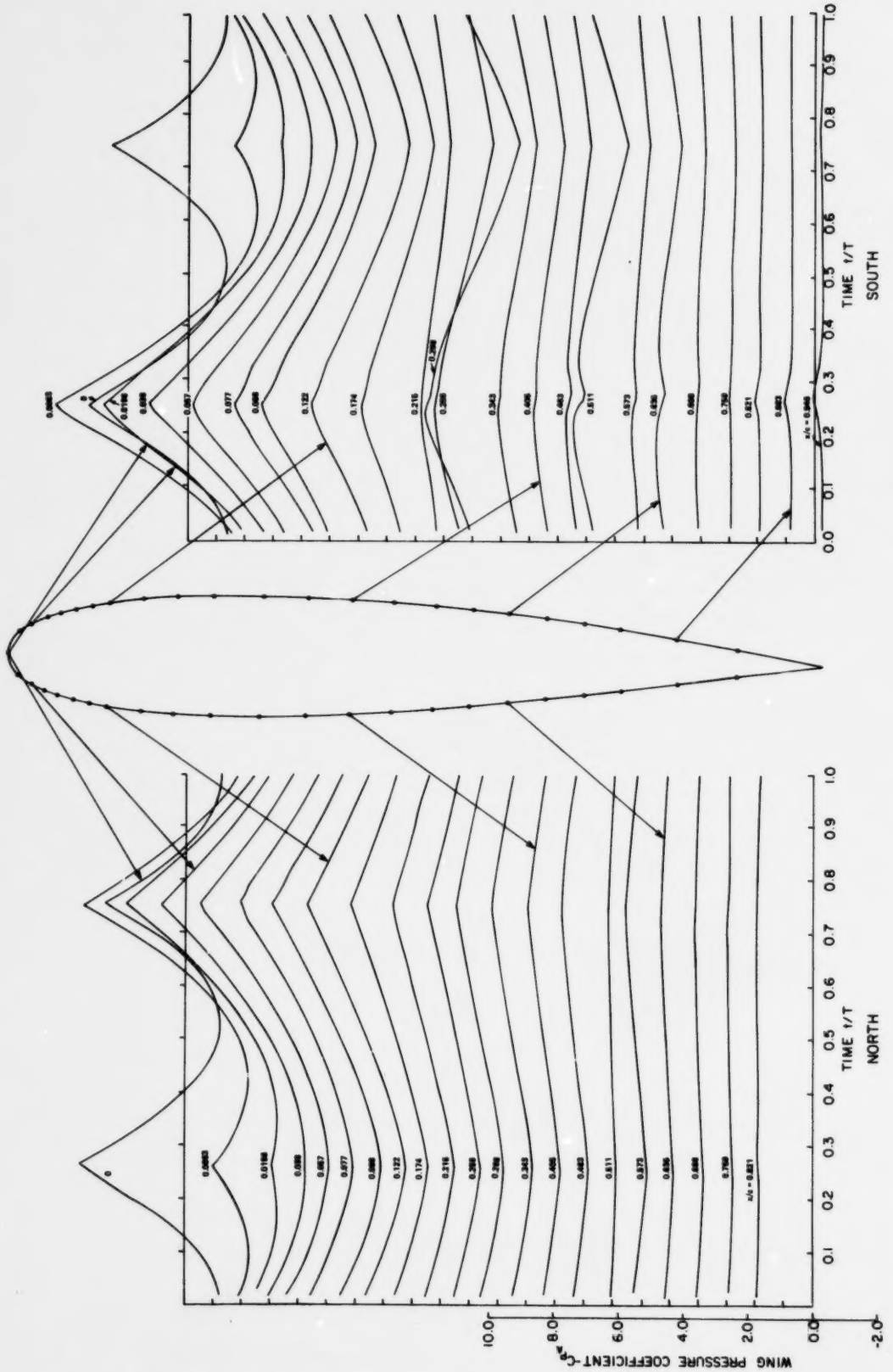

FIG. 9: WING PRESSURE TIME HISTORIES, $\alpha_m = \pm 15°$, $\frac{R\Omega}{V} = 4$, f = 0.55 hz

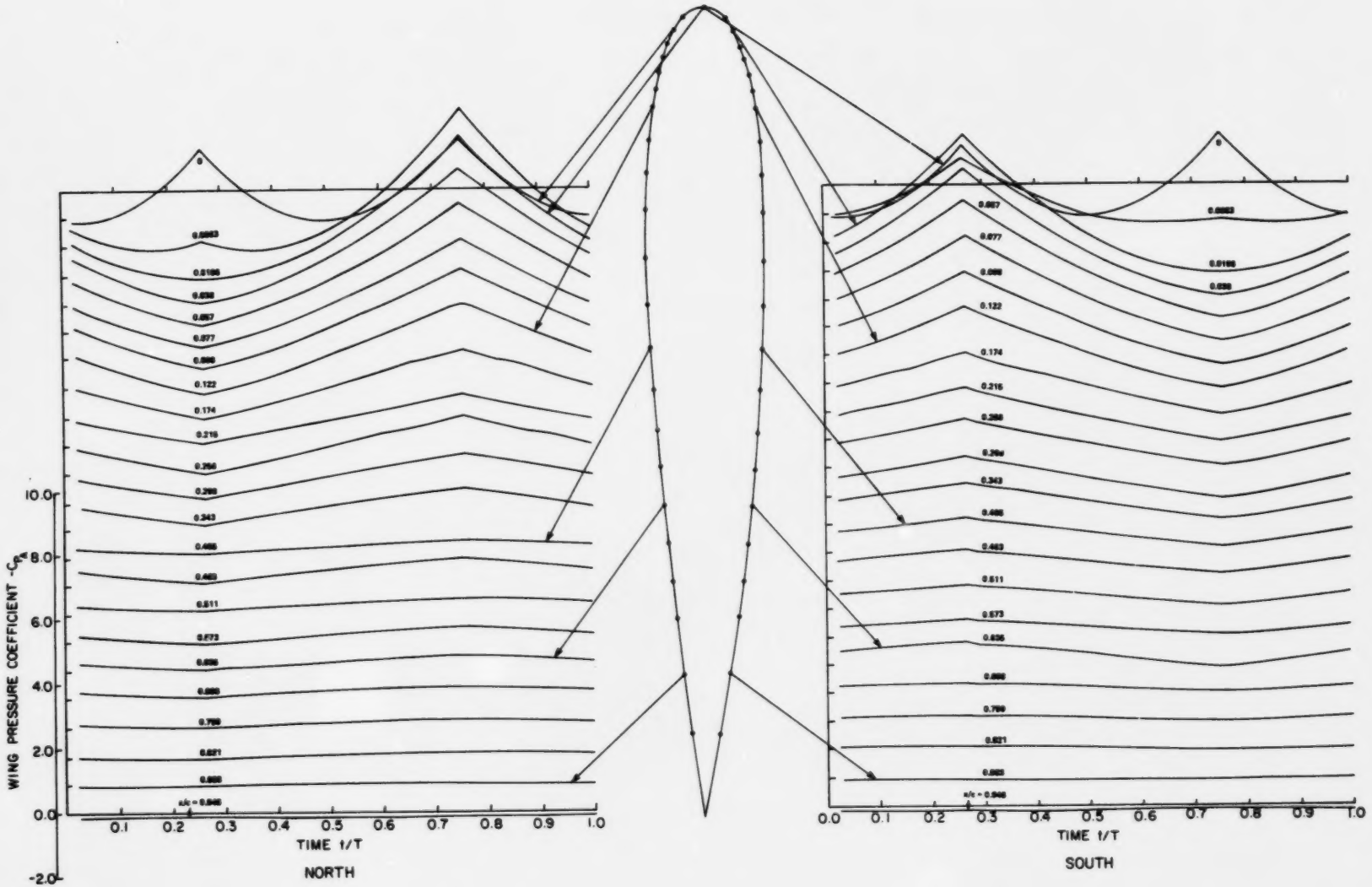

FIG. 10: WING PRESSURE TIME HISTORIES, $\alpha_m = \pm 12°$, $\frac{R\Omega}{V} = 5$, f = 0.55 hz

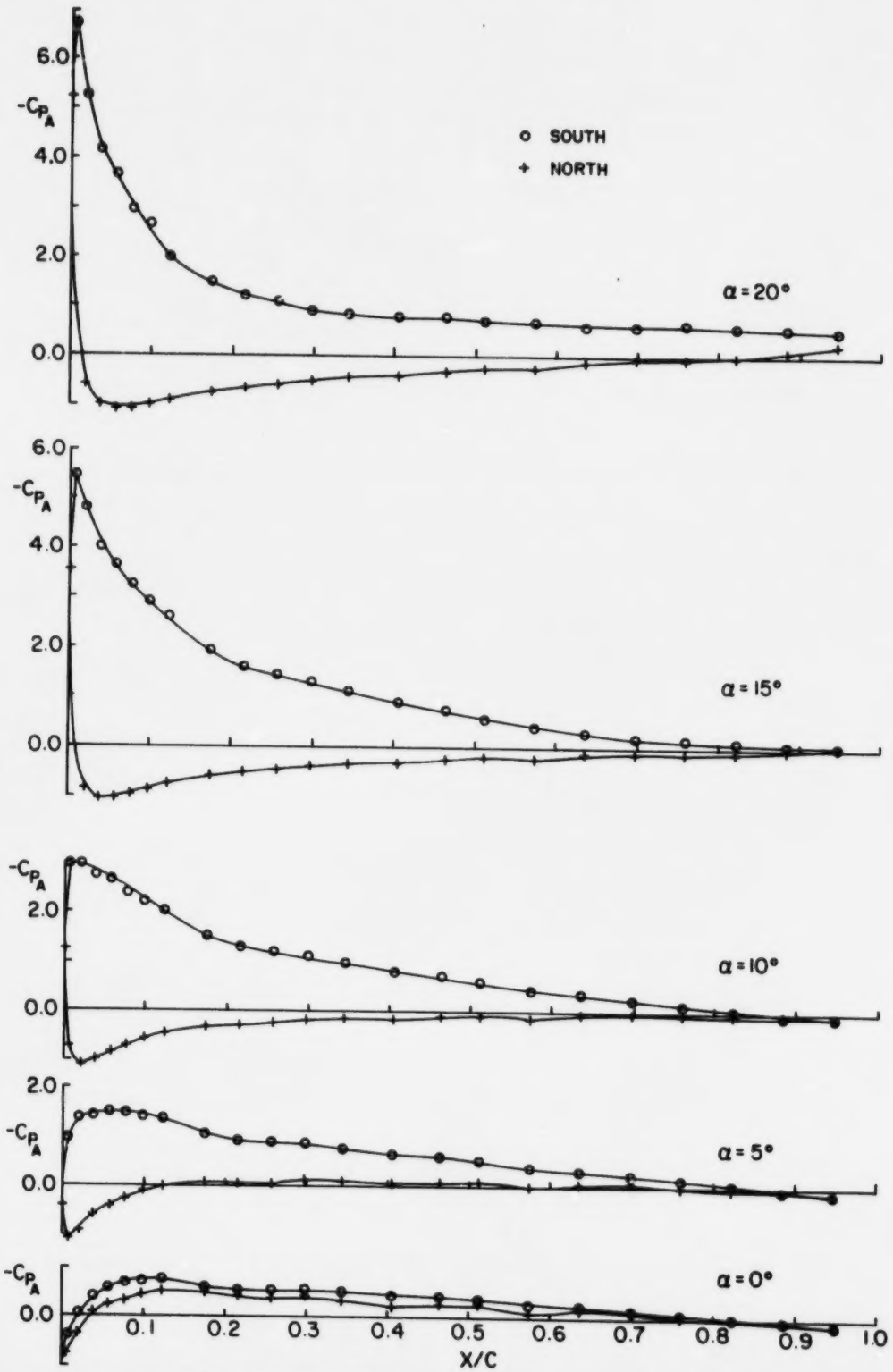

FIG. 11a: WING CHORDWISE PRESSURES DURING POSITIVE HALF-CYCLE, $\alpha_m = \pm 30°$, $\frac{R\Omega}{V} = 2$, f = 0.55 hz (Cont'd)

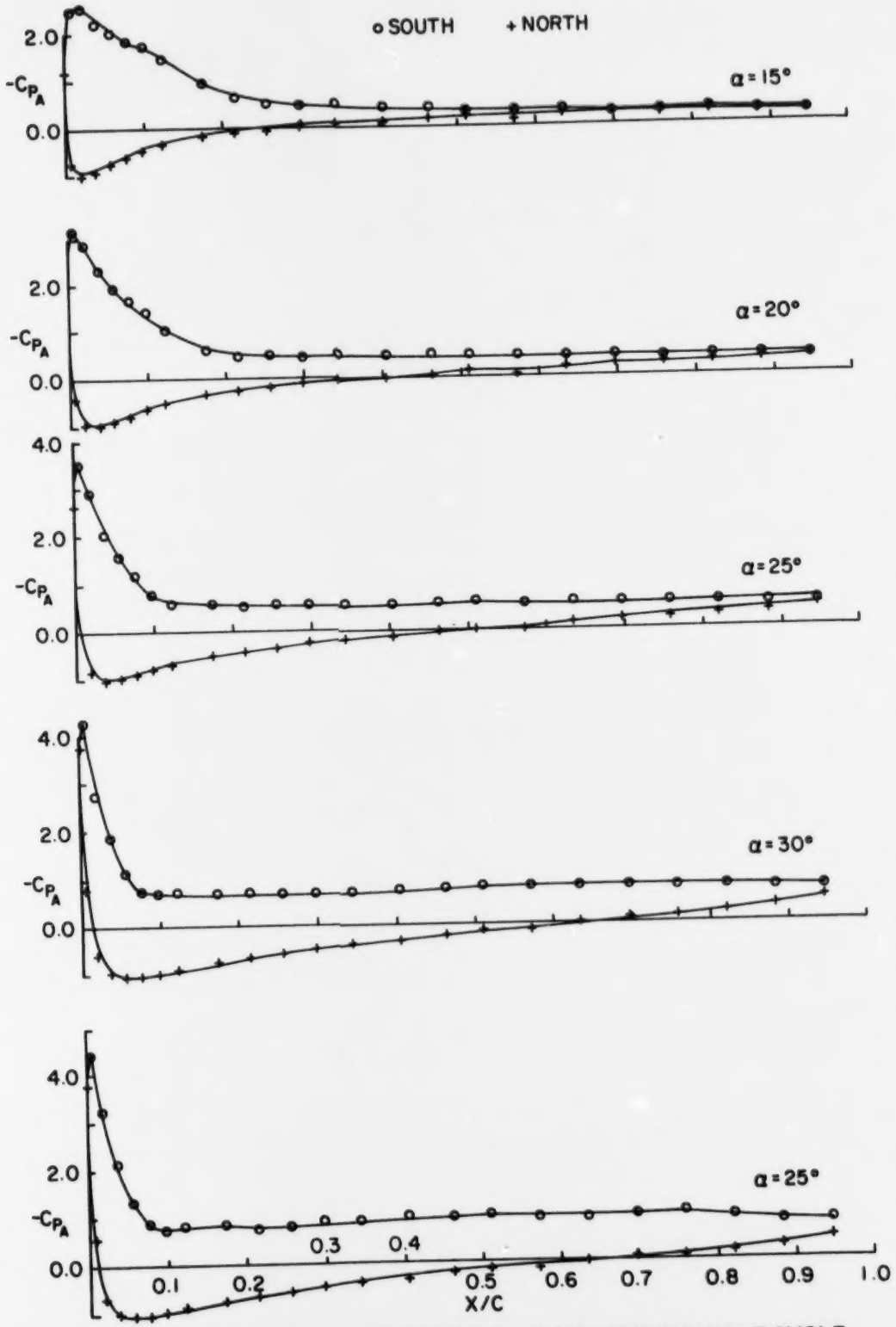

FIG. 11a: WING CHORDWISE PRESSURES DURING POSITIVE HALF-CYCLE, $\alpha_m = \pm 30°$, $\frac{R\Omega}{V} = 2$, f = 0.55 hz (Cont'd)

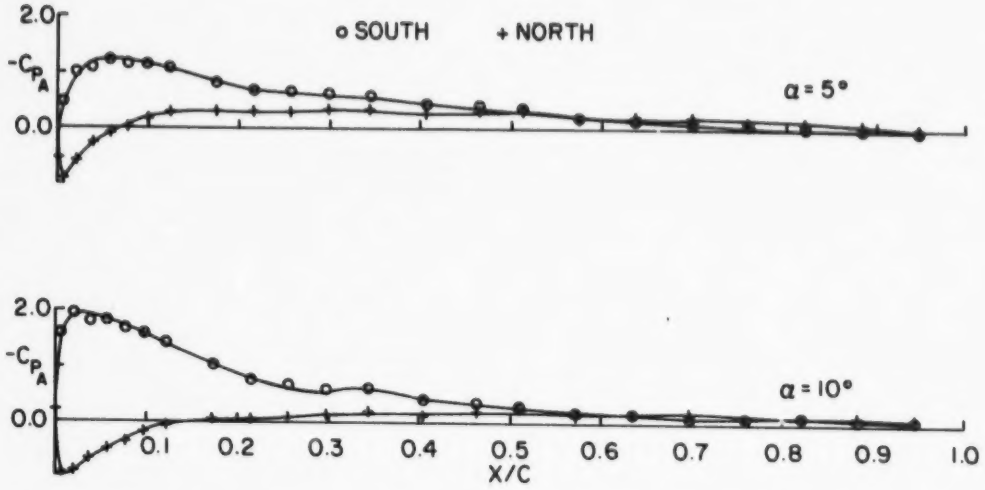

FIG. 11a: WING CHORDWISE PRESSURES DURING POSITIVE HALF-CYCLE,

$$\alpha_m = \pm 30°, \frac{R\Omega}{V} = 2, f = 0.55 \text{ hz}$$

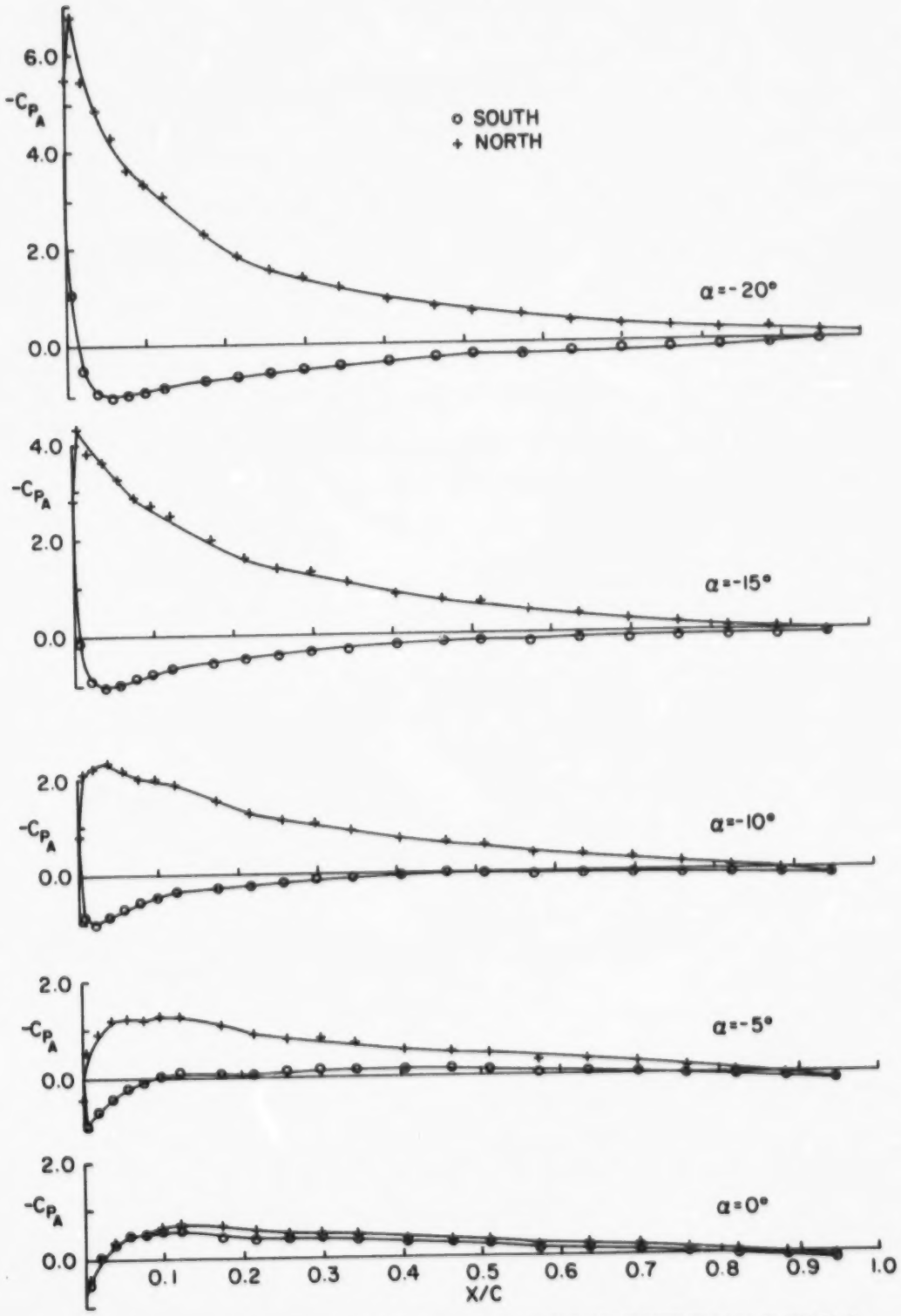

FIG. 11b: WING CHORDWISE PRESSURES DURING NEGATIVE HALF-CYCLE, $\alpha_m = \pm 30°$, $\frac{R\Omega}{V} = 2$, f = 0.55 hz (Cont'd)

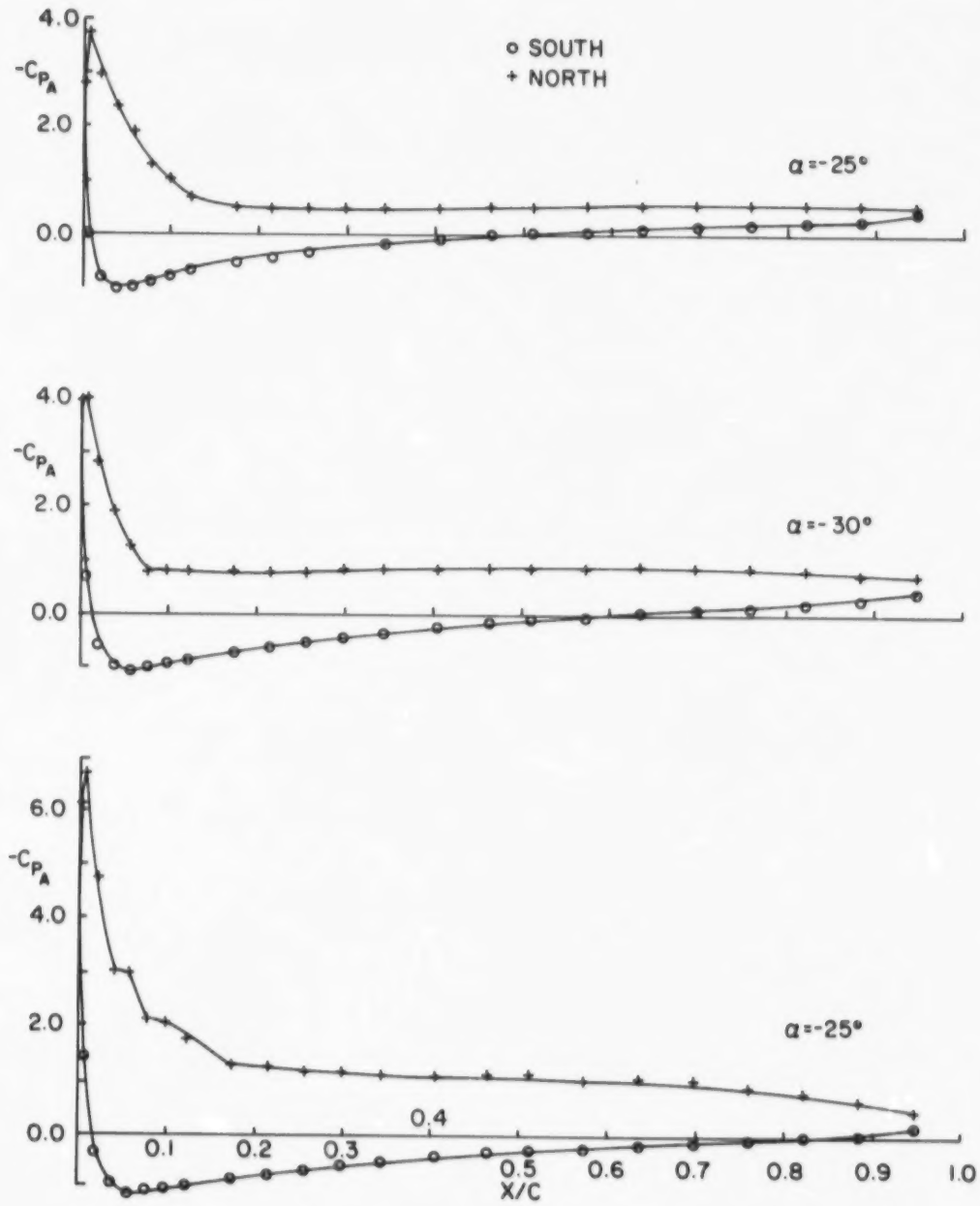

FIG. 11b: WING CHORDWISE PRESSURES DURING NEGATIVE HALF-CYCLE, $\alpha_m = \pm 30°$, $\frac{R\Omega}{V} = 2$, f = 0.55 hz (Cont'd)

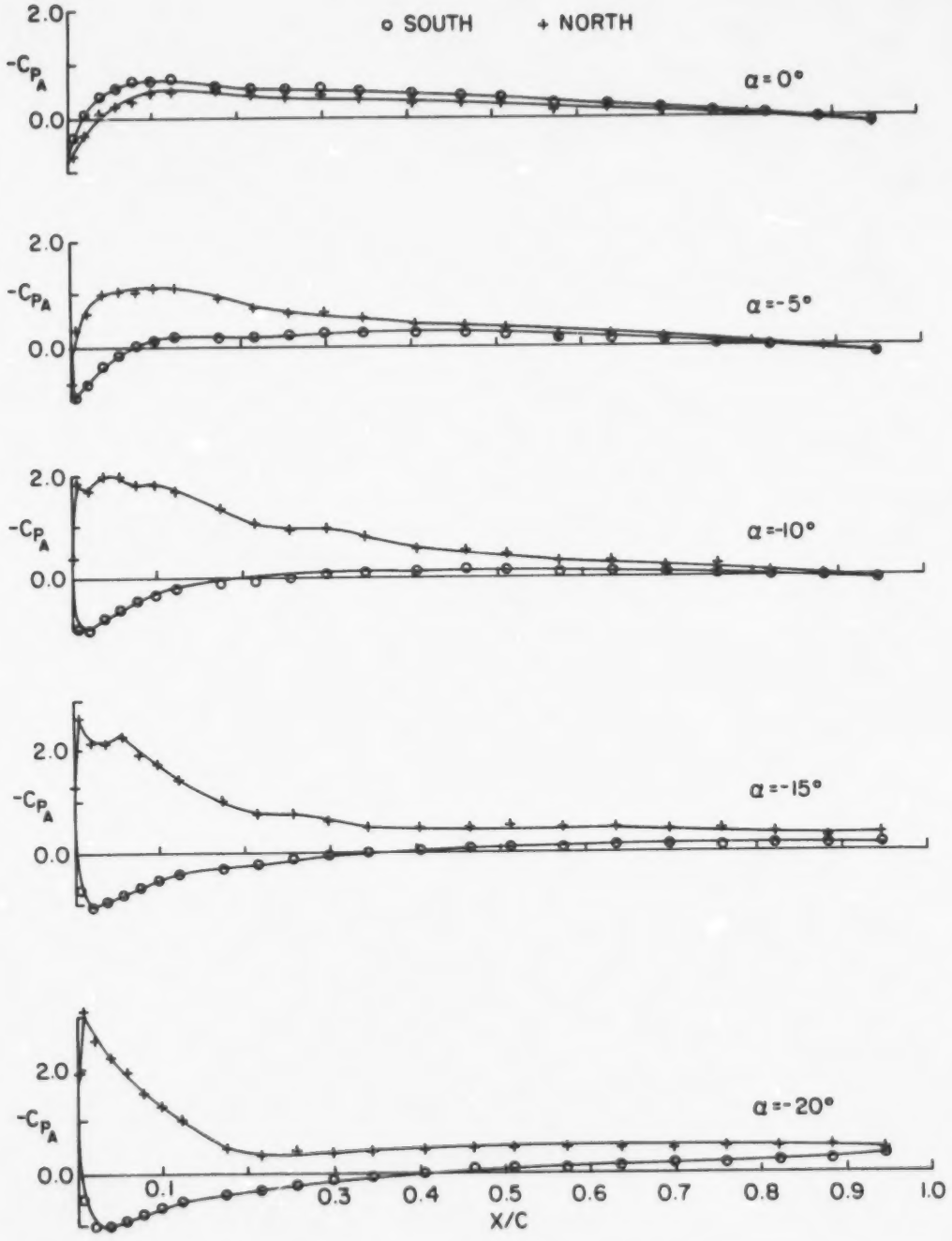

FIG. 11b: WING CHORDWISE PRESSURES DURING NEGATIVE HALF-CYCLE, $\alpha_m = \pm 30°$, $\frac{R\Omega}{V} = 2$, f = 0.55 hz

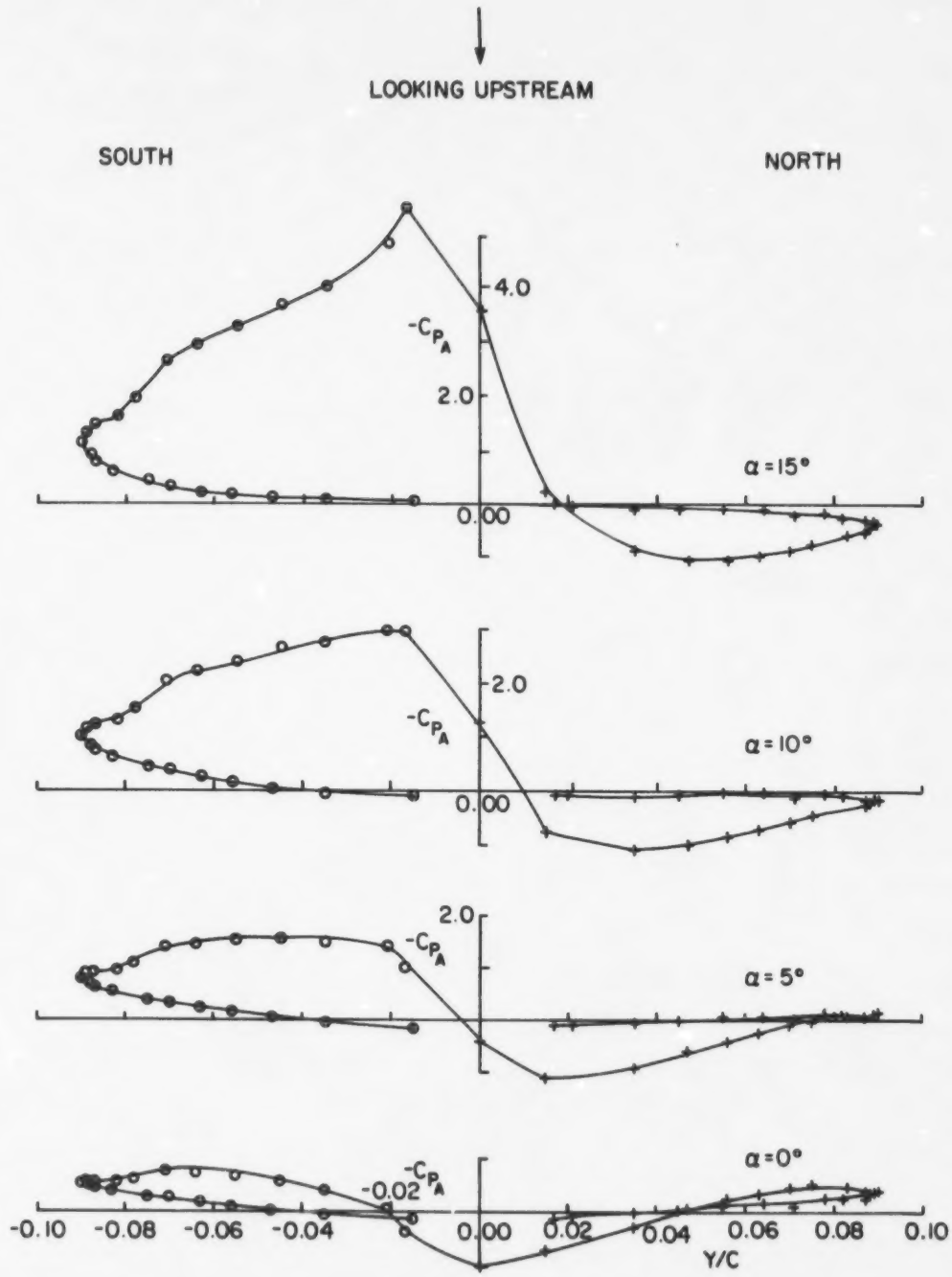

FIG. 12a: WING THICKNESSWISE PRESSURES DURING POSITIVE HALF-CYCLE, $\alpha_m = \pm 30°$, $\frac{R\Omega}{V} = 2$, f = 0.55 hz (Cont'd)

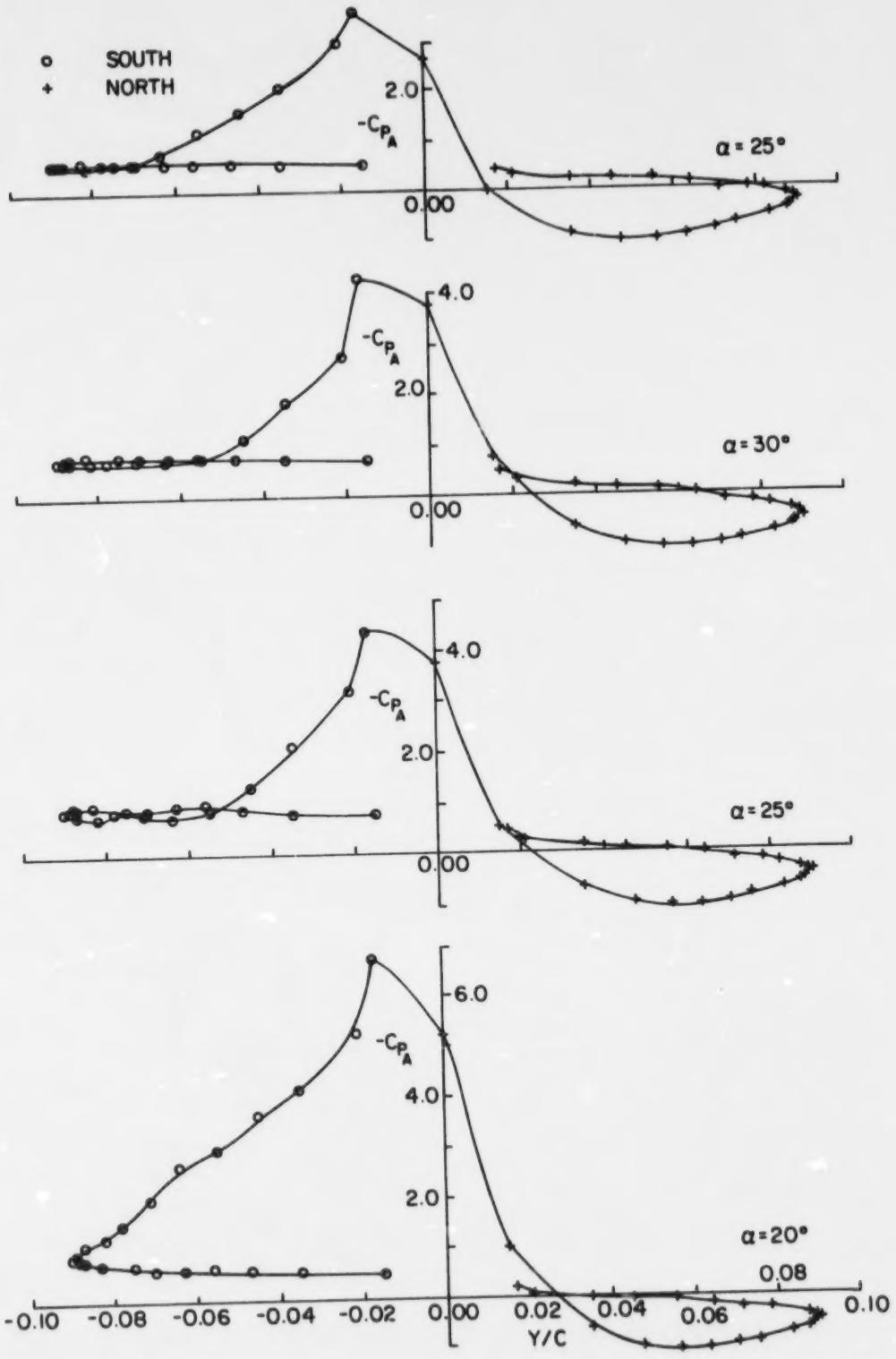

FIG. 12a: WING THICKNESSWISE PRESSURES DURING POSITIVE HALF-CYCLE, $\alpha_m = \pm 30°$, $\frac{R\Omega}{V} = 2$, f = 0.55 hz (Cont'd)

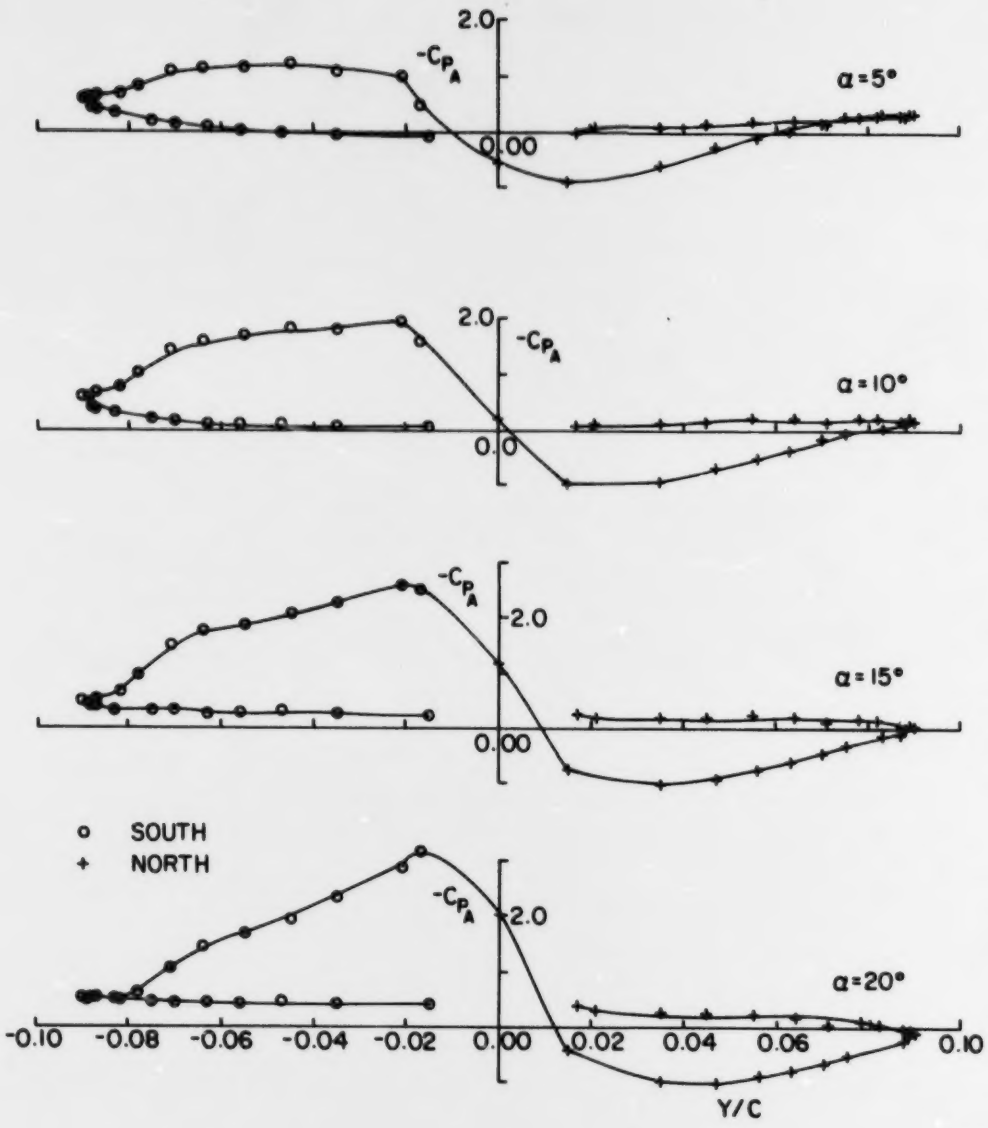

FIG. 12a: WING THICKNESSWISE PRESSURES DURING POSITIVE HALF-CYCLE,

$\alpha_m = \pm 30°$, $\frac{R\Omega}{V} = 2$, **f = 0.55 hz**

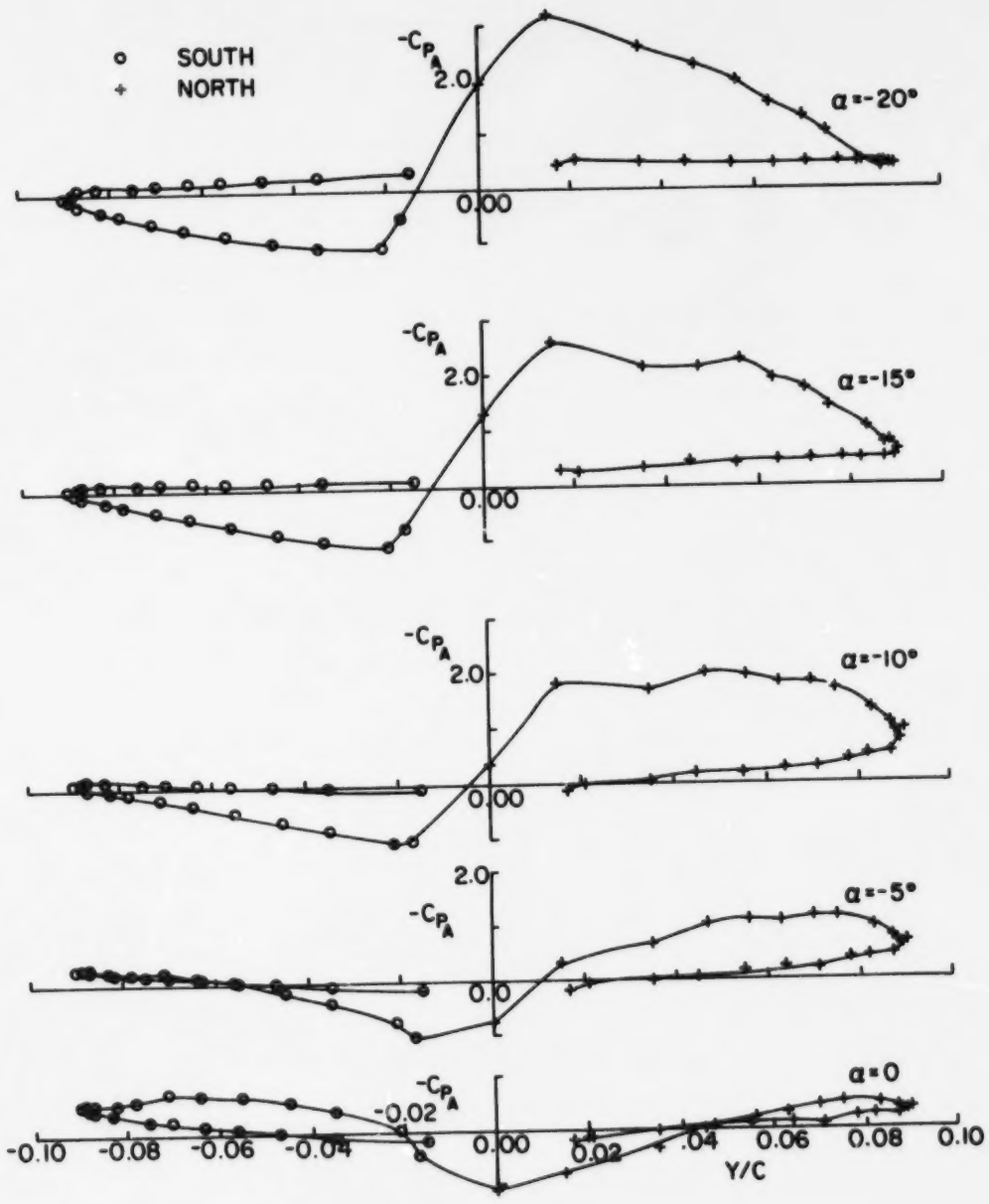

FIG. 12b: WING THICKNESSWISE PRESSURES DURING NEGATIVE HALF-CYCLE, $\alpha_m = \pm 30°$, $\frac{R\Omega}{V} = 2$, f = 0.55 hz (Cont'd)

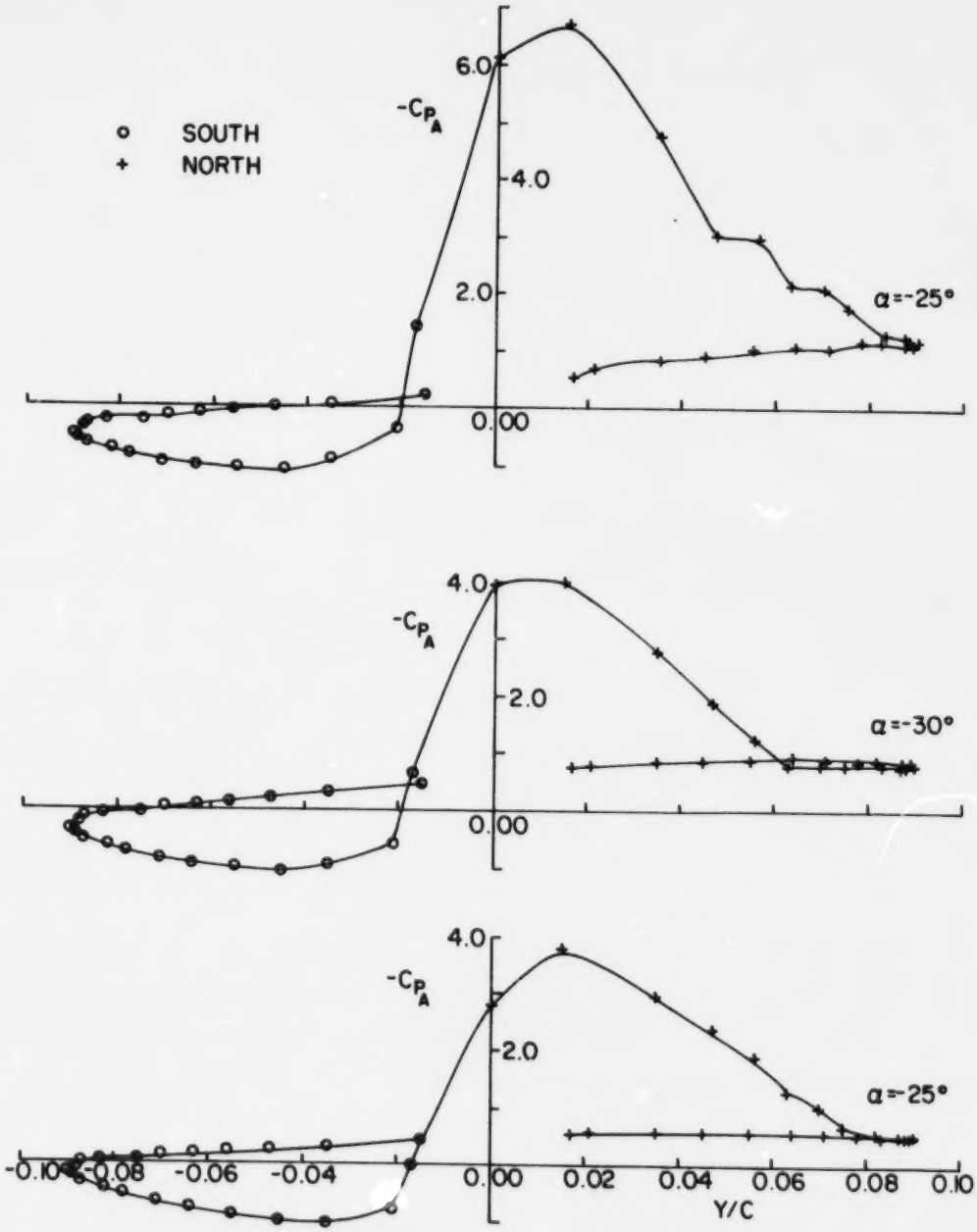

FIG. 12b: WING THICKNESSWISE PRESSURES DURING NEGATIVE HALF-CYCLE, $\alpha_m = \pm 30°$, $\frac{R\Omega}{V} = 2$, f = 0.55 hz (Cont'd)

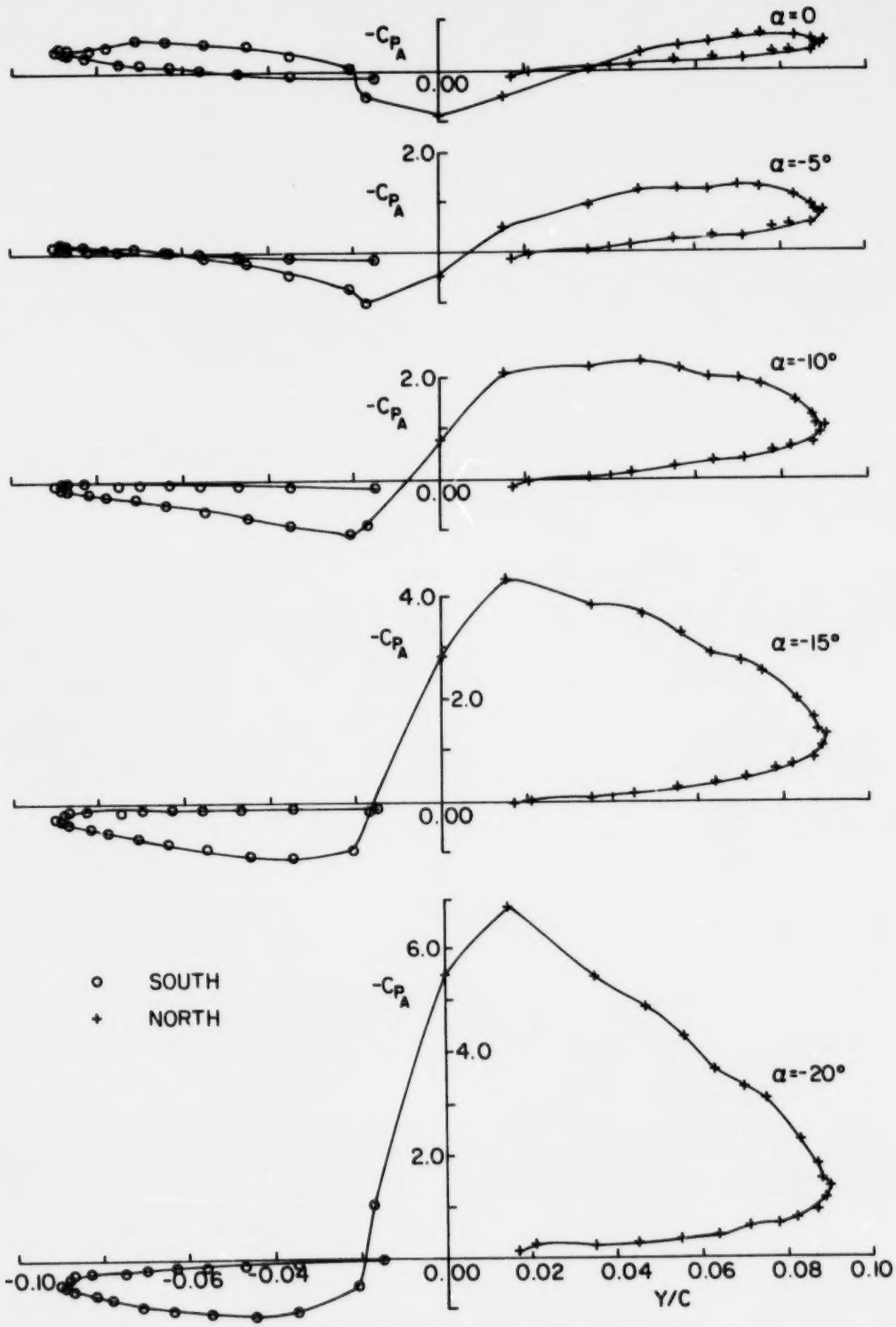

FIG. 12b: WING THICKNESSWISE PRESSURES DURING NEGATIVE HALF-CYCLE, $\alpha_m = \pm 30°$, $\frac{R\Omega}{V} = 2$, f = 0.55 hz

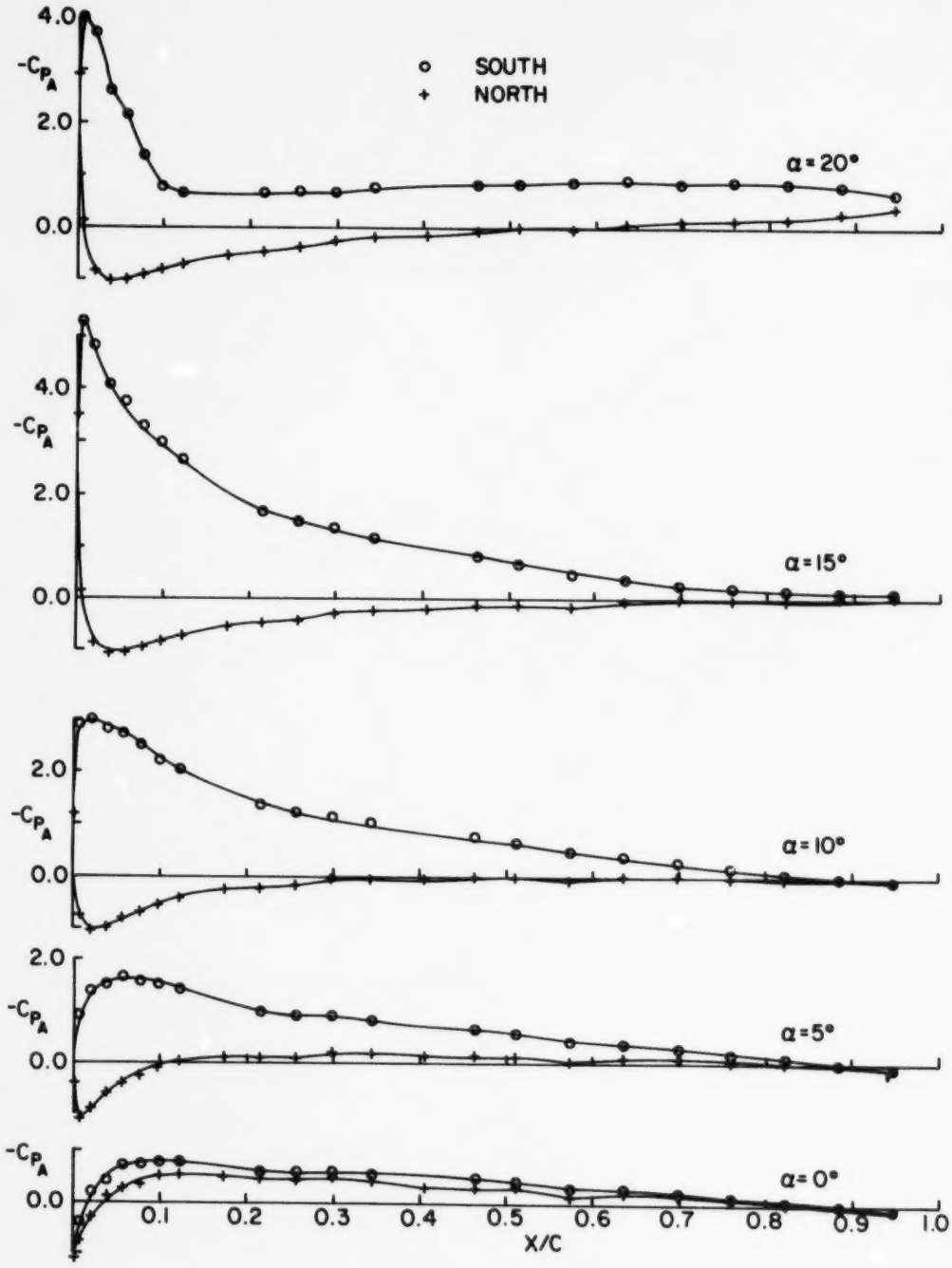

FIG. 13a: WING CHORDWISE PRESSURES DURING POSITIVE HALF-CYCLE, $\alpha_m = \pm 20°$, $\frac{R\Omega}{V} = 3$, f = 0.55 hz (Cont'd)

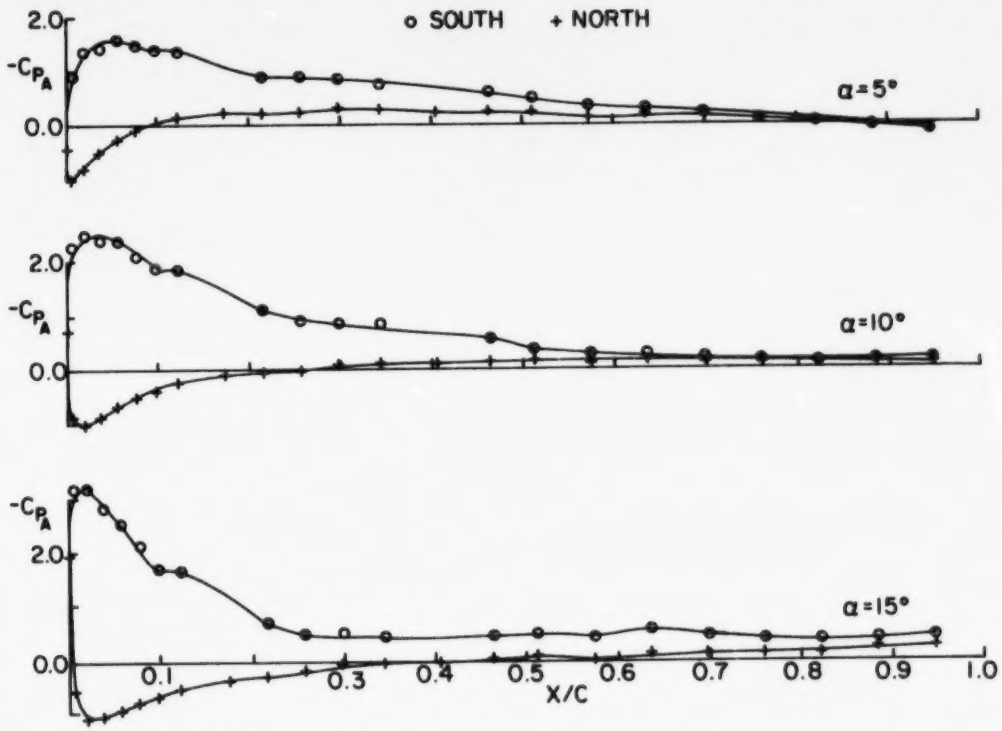

FIG. 13a: WING CHORDWISE PRESSURES DURING POSITIVE HALF-CYCLE,

$$\alpha_m = \pm 20°, \frac{R\Omega}{V} = 3, f = 0.55 \text{ hz}$$

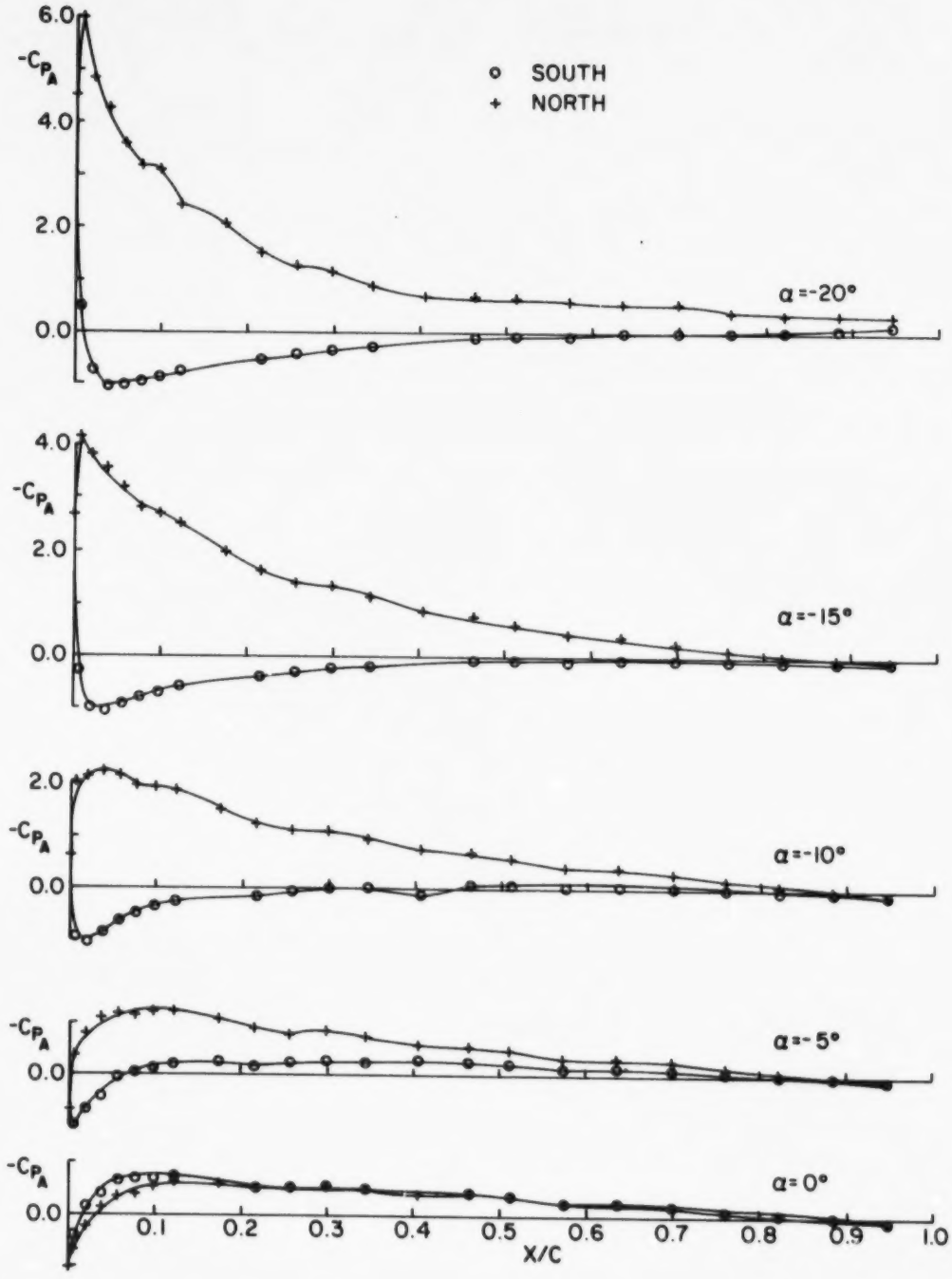

FIG. 13b: WING CHORDWISE PRESSURES DURING NEGATIVE HALF-CYCLE, $\alpha_m = \pm 20°$, $\frac{R\Omega}{V} = 3$, f = 0.55 hz (Cont'd)

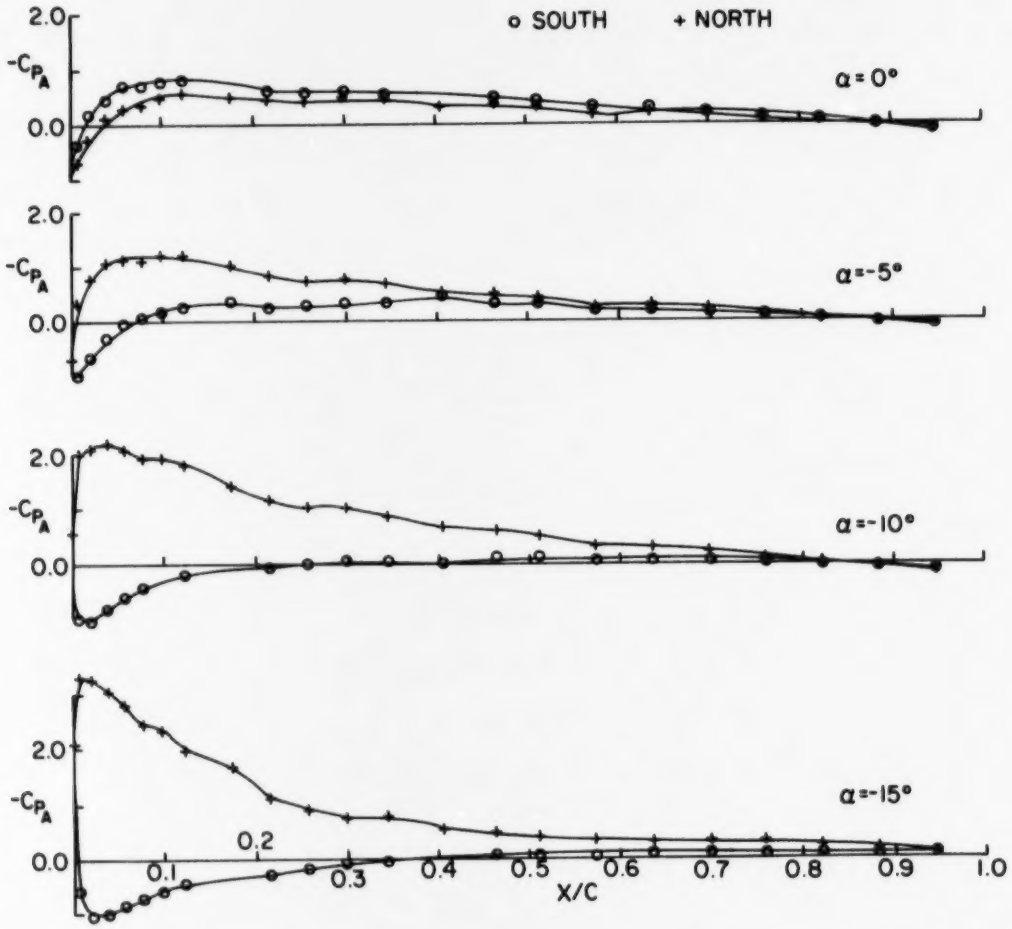

FIG. 13b: WING CHORDWISE PRESSURES DURING NEGATIVE HALF-CYCLE,

$$\alpha_m = \pm 20^\circ, \frac{R\Omega}{V} = 3, f = 0.55 \text{ hz}$$

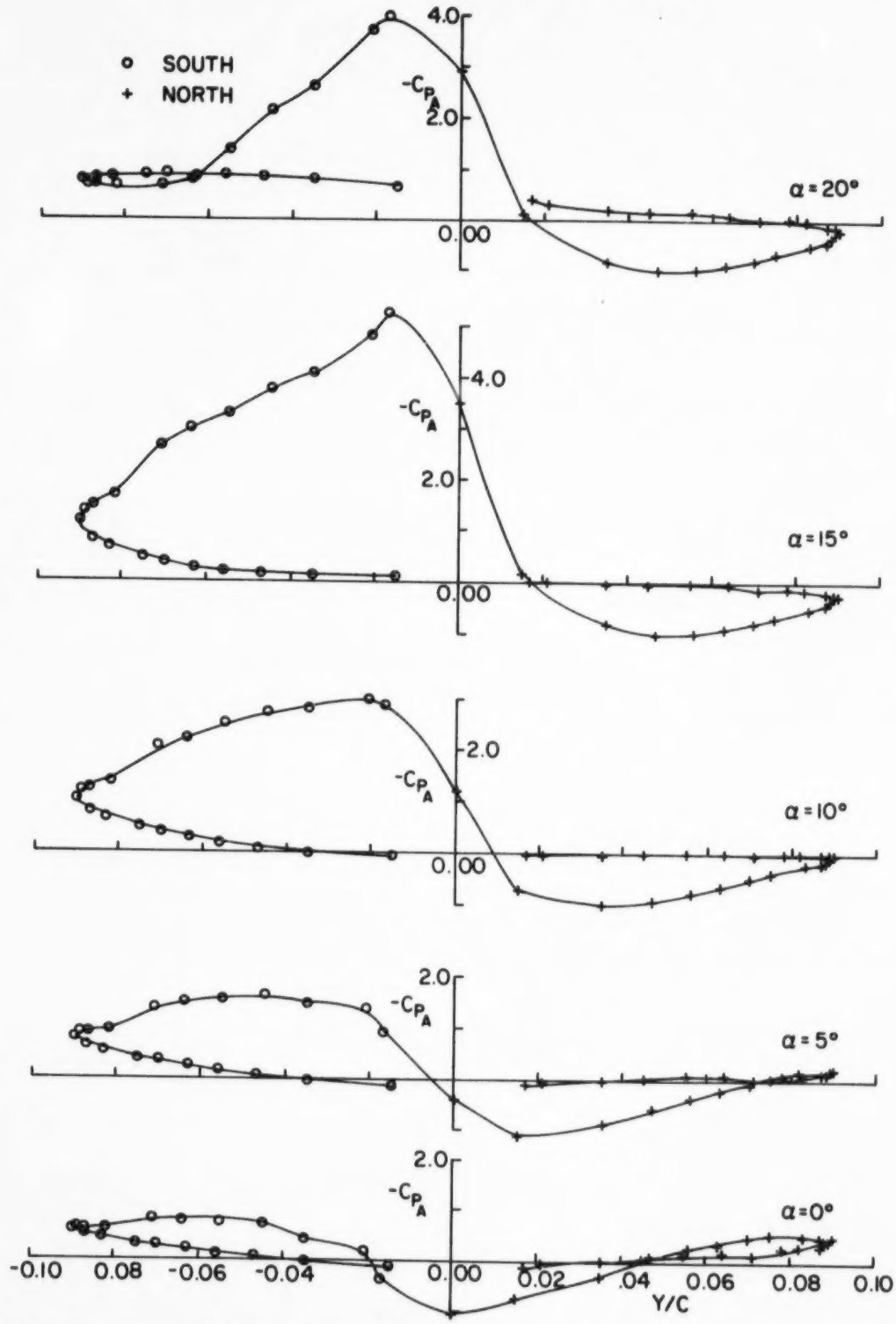

FIG. 14a: WING THICKNESSWISE PRESSURES DURING POSITIVE HALF-CYCLE, $\alpha_m = \pm 20°$, $\frac{R\Omega}{V} = 3$, f = 0.55 hz (Cont'd)

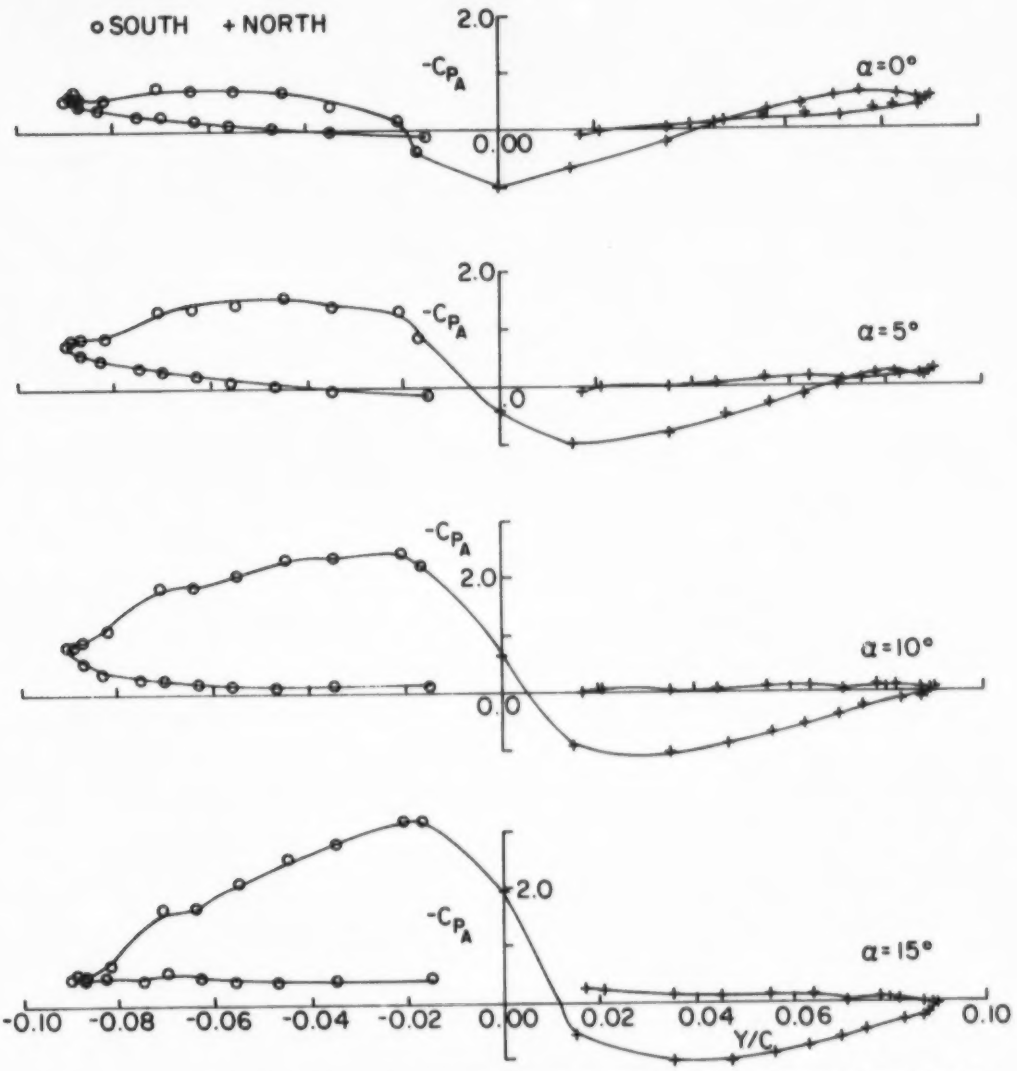

FIG. 14a: WING THICKNESSWISE PRESSURES DURING POSITIVE HALF-CYCLE, $\alpha_m = \pm 20°$, $\frac{R\Omega}{V} = 3$, f = 0.55 hz

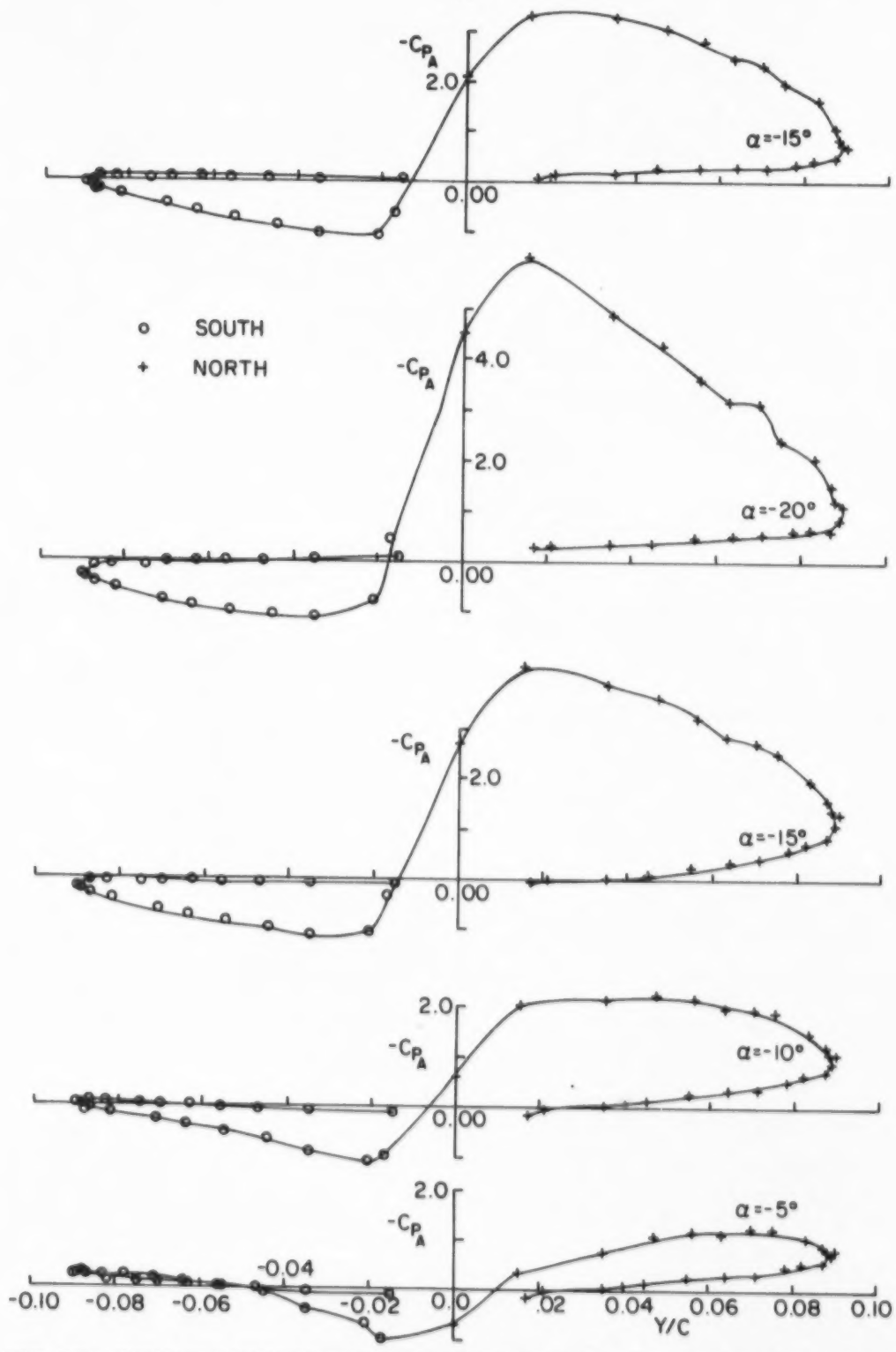

FIG. 14b: WING THICKNESSWISE PRESSURES DURING NEGATIVE HALF-CYCLE, $\alpha_m = \pm 20°$, $\frac{R\Omega}{V} = 3$, f = 0.55 hz (Cont'd)

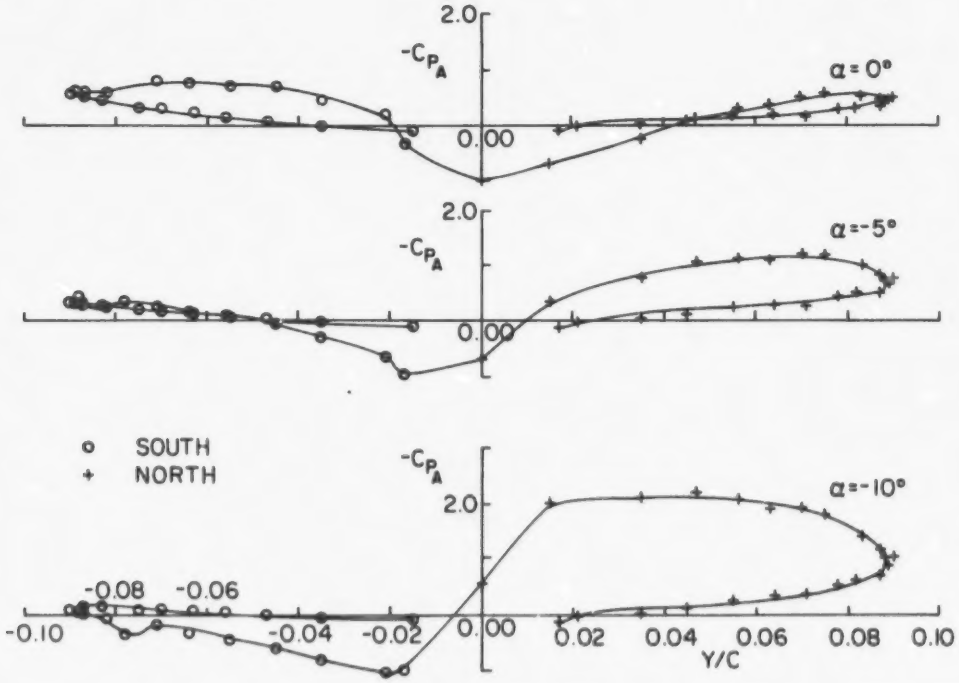

FIG. 14b: WING THICKNESSWISE PRESSURES DURING NEGATIVE HALF-CYCLE,

$$\alpha_m = \pm 20°, \frac{R\Omega}{V} = 3, f = 0.55\ hz$$

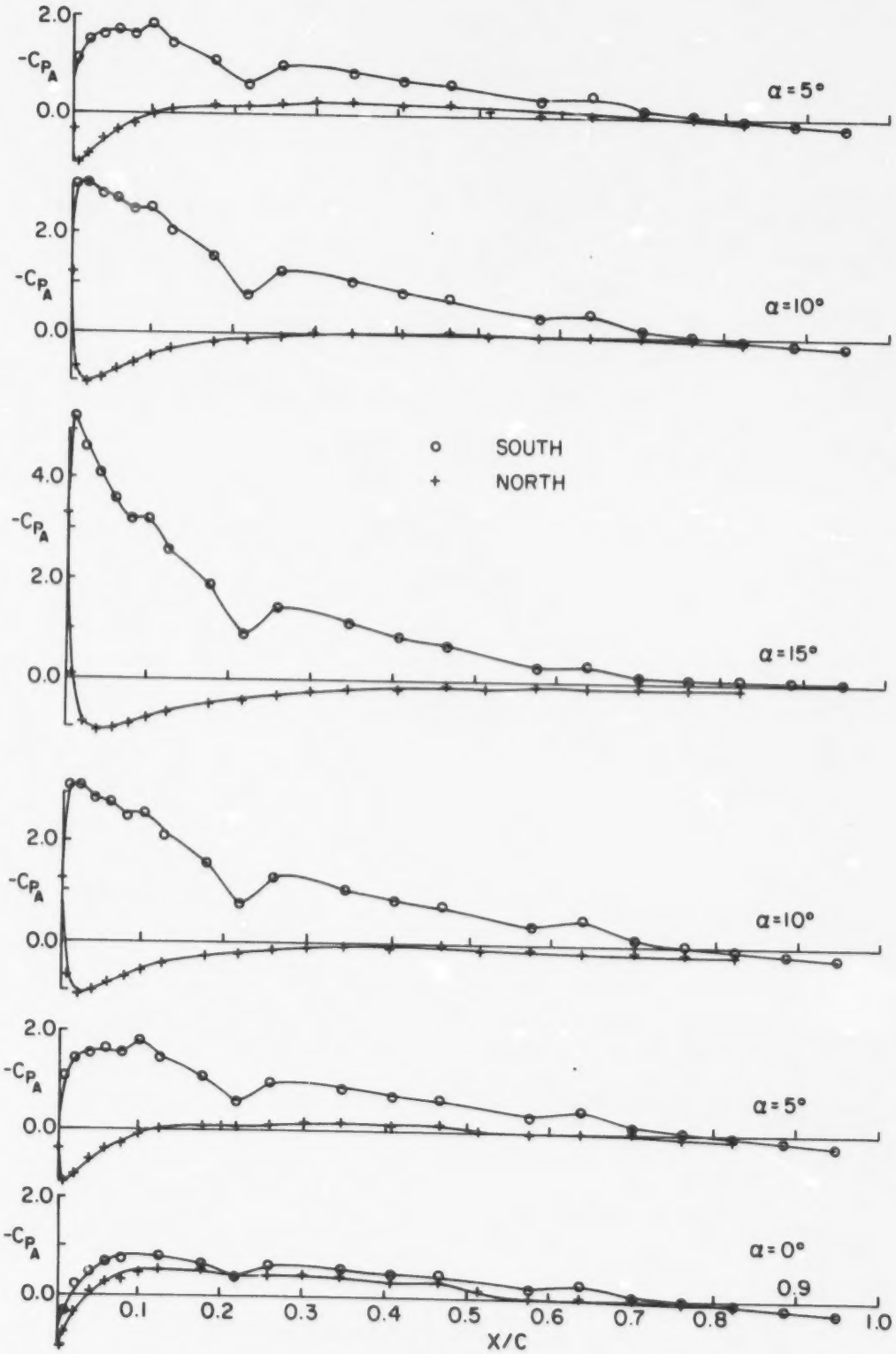

FIG. 15a: WING CHORDWISE PRESSURES DURING POSITIVE HALF-CYCLE,

$\alpha_m = \pm 15°$, $\frac{R\Omega}{V} = 4$, $f = 0.55$ hz

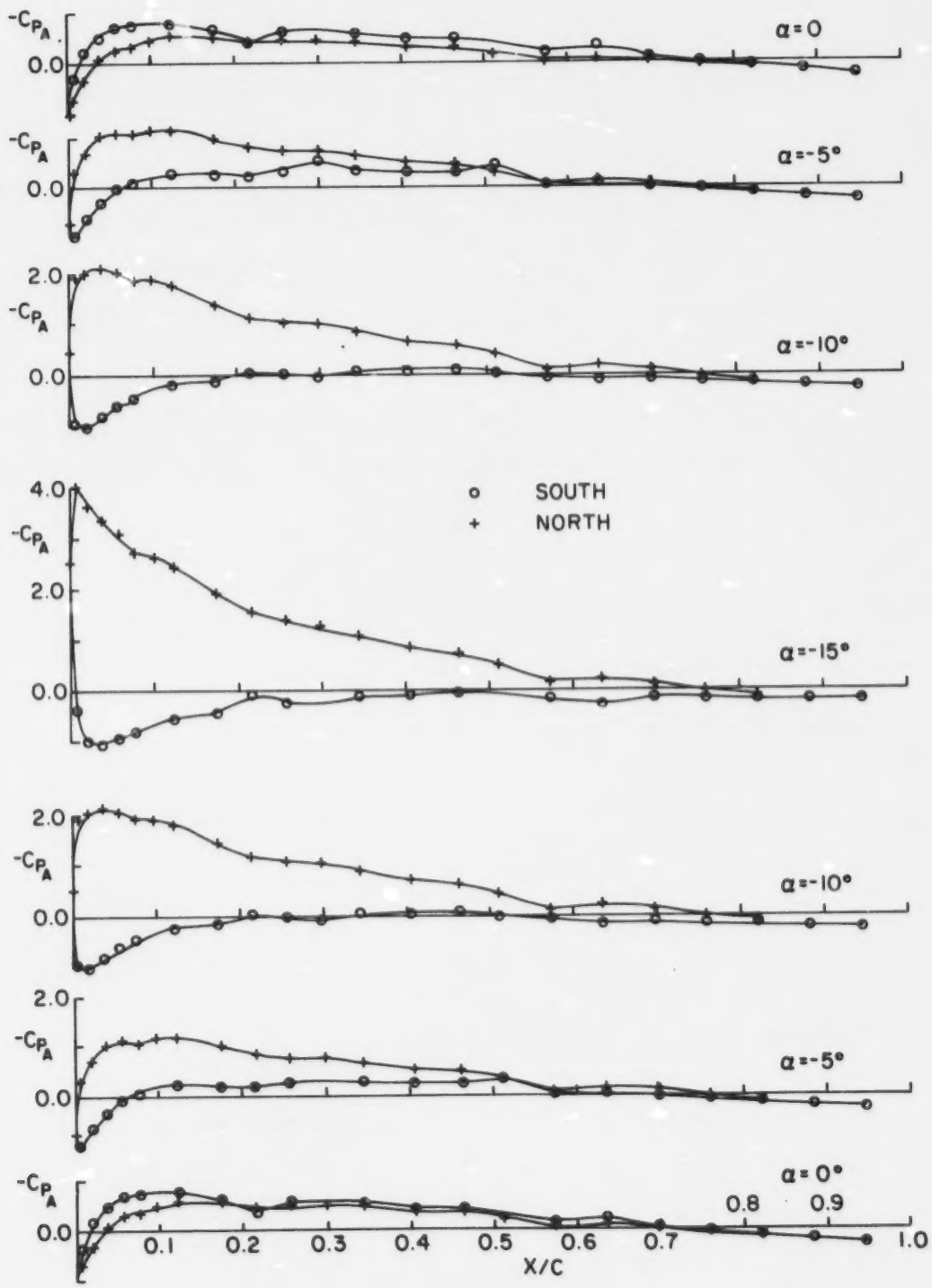

FIG. 15b: WING CHORDWISE PRESSURES DURING NEGATIVE HALF-CYCLE,

$\alpha_m = \pm 15°$, $\frac{R\Omega}{V} = 4$, $f = 0.55$ hz

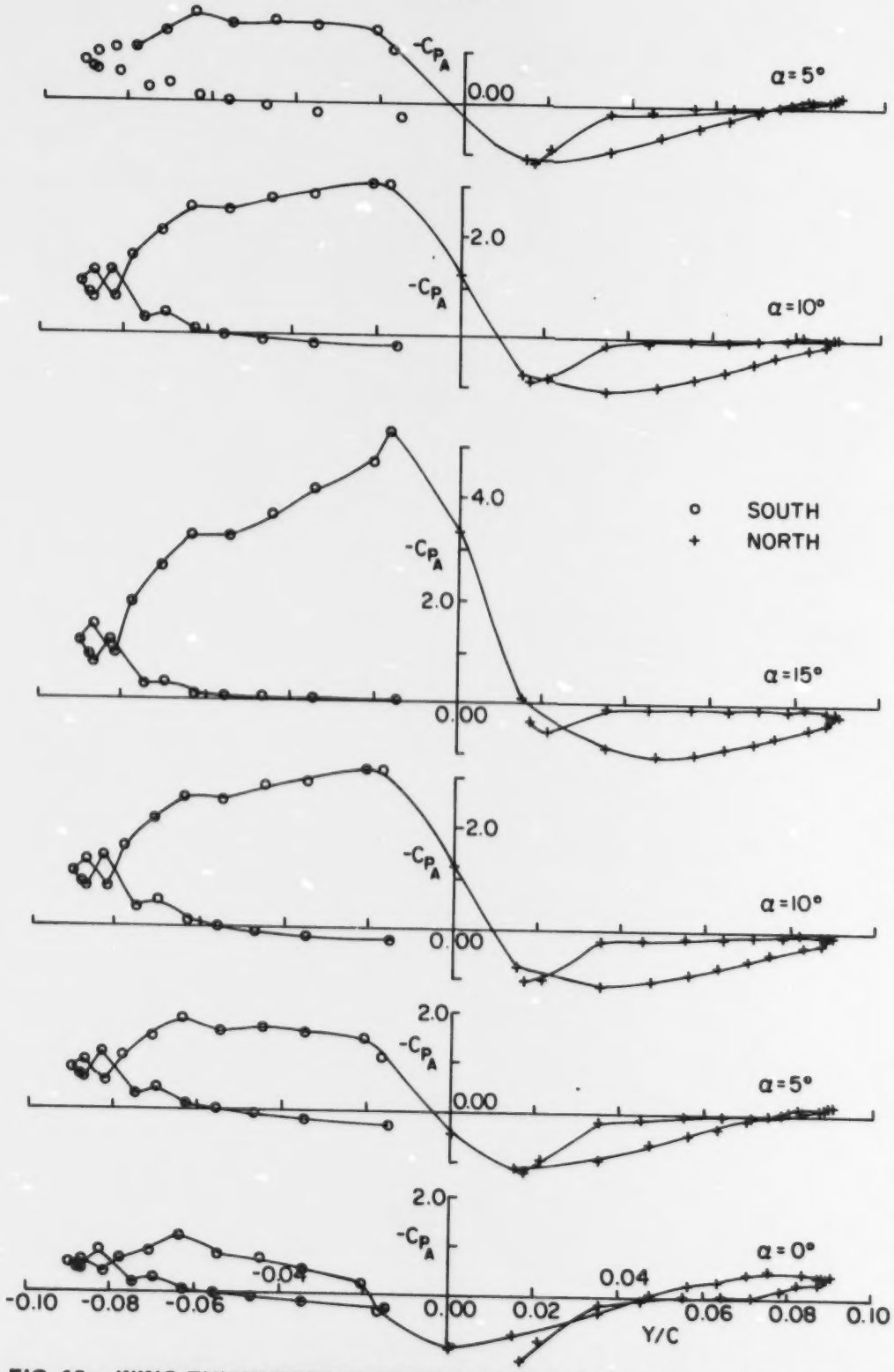

FIG. 16a: WING THICKNESSWISE PRESSURES DURING POSITIVE HALF-CYCLE, $\alpha_m = \pm 15°$, $\frac{R\Omega}{V} = 4$, $f = 0.55$ hz

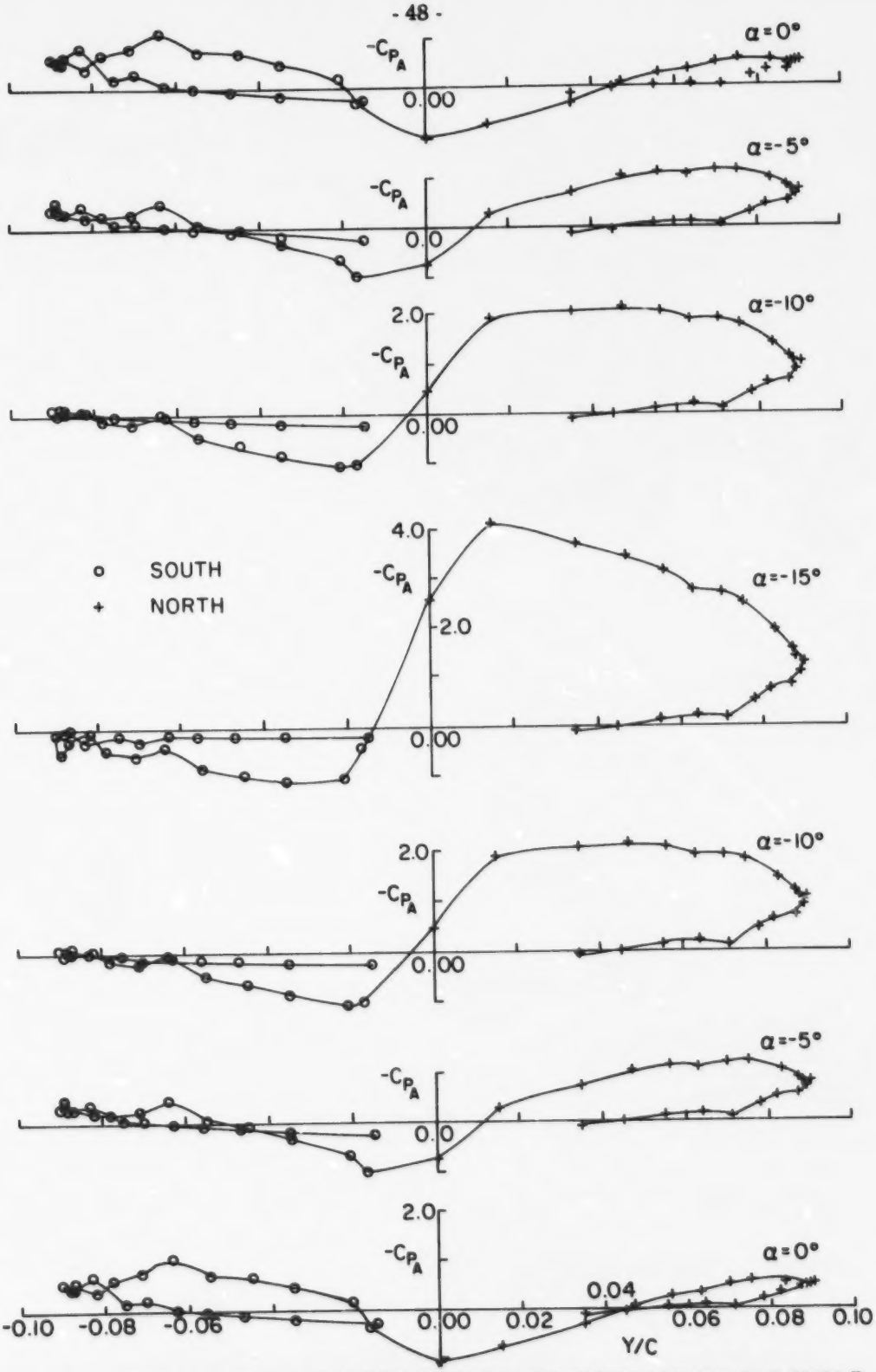

FIG. 16b: WING THICKNESSWISE PRESSURES DURING NEGATIVE HALF-CYCLE, $\alpha_m = \pm 15°$, $\frac{R\Omega}{V} = 4$, f = 0.55 hz

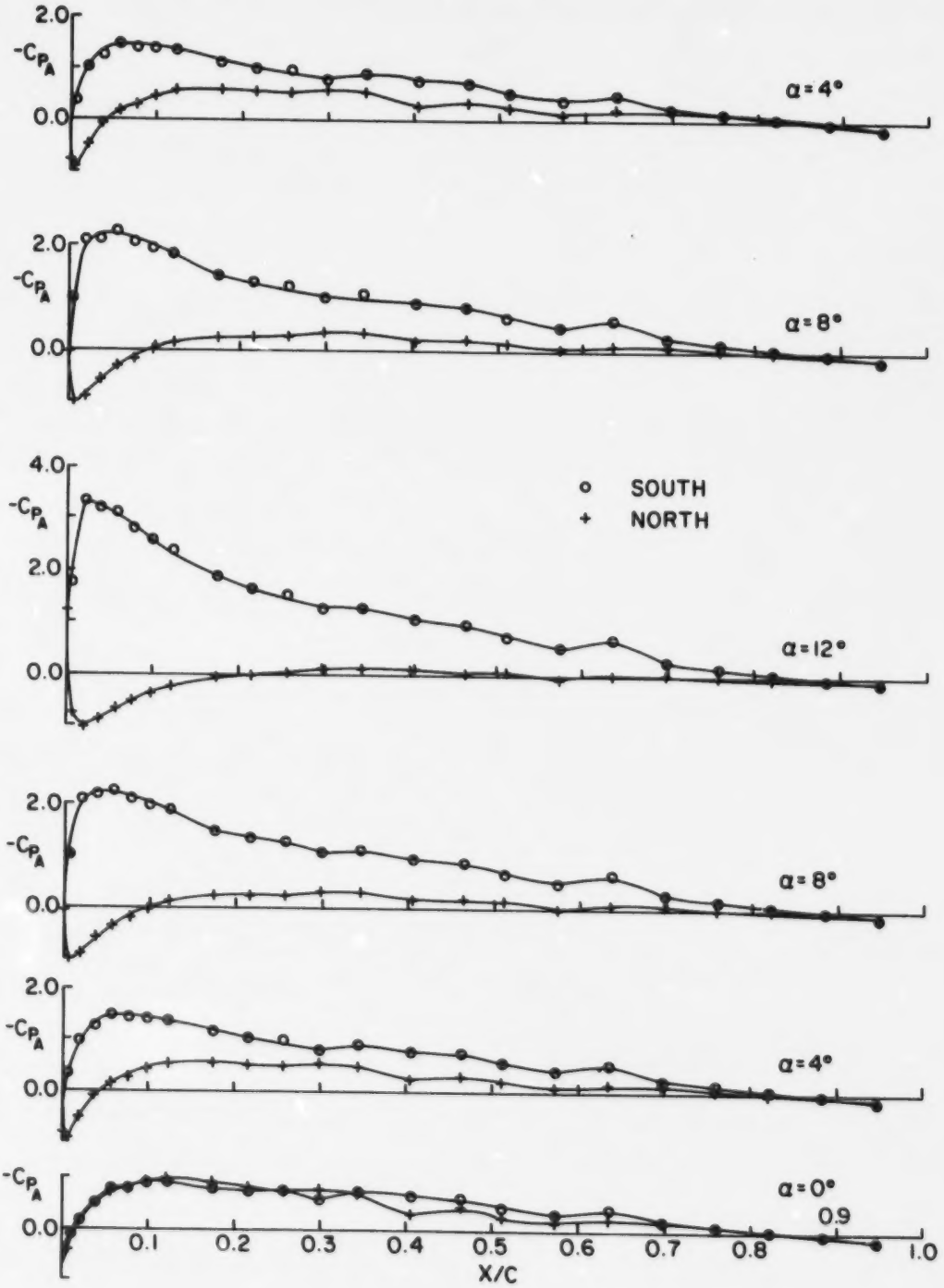

FIG. 17a: WING CHORDWISE PRESSURES DURING POSITIVE HALF-CYCLE, $\alpha_m = \pm 12°$, $\frac{R\Omega}{V} = 5$, f = 0.55 hz

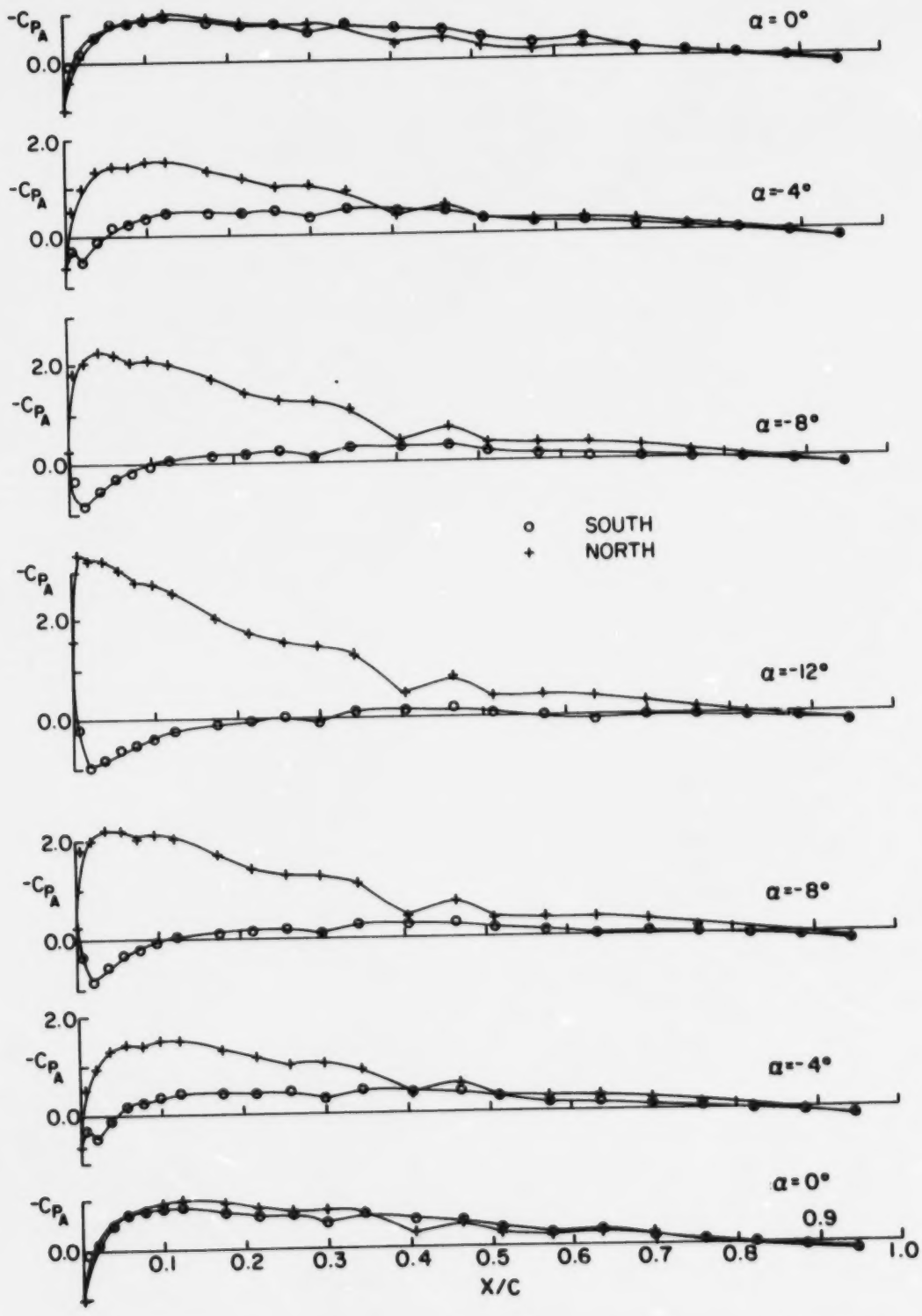

FIG. 17b: WING CHORDWISE PRESSURES DURING NEGATIVE HALF-CYCLE, $\alpha_m = \pm 12°$, $\frac{R\Omega}{V} = 5$, f = 0.55 hz

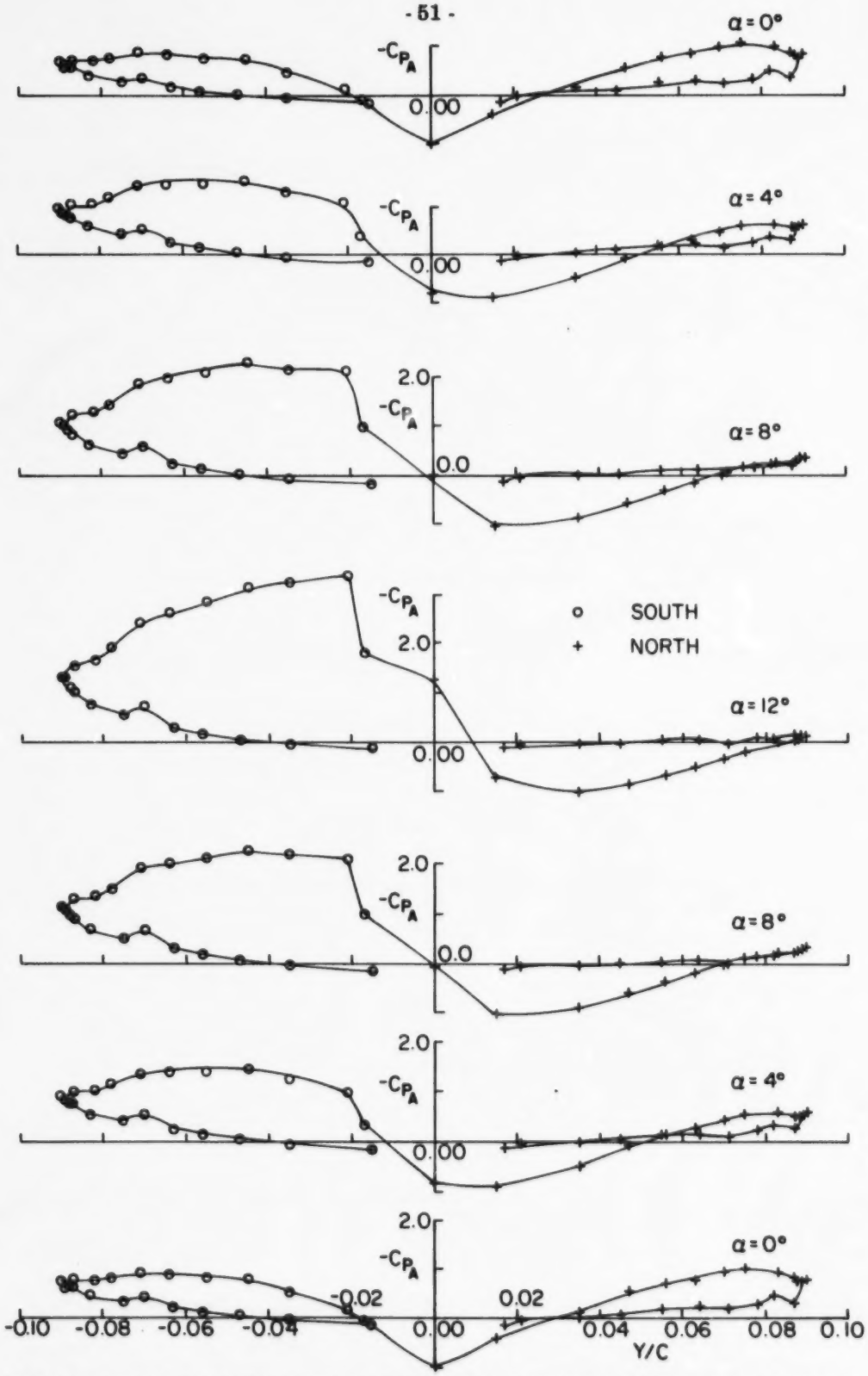

FIG. 18a: WING THICKNESSWISE PRESSURES DURING POSITIVE HALF-CYCLE, $\alpha_m = \pm 12°$, $\frac{R\Omega}{V} = 5$, f = 0.55 hz

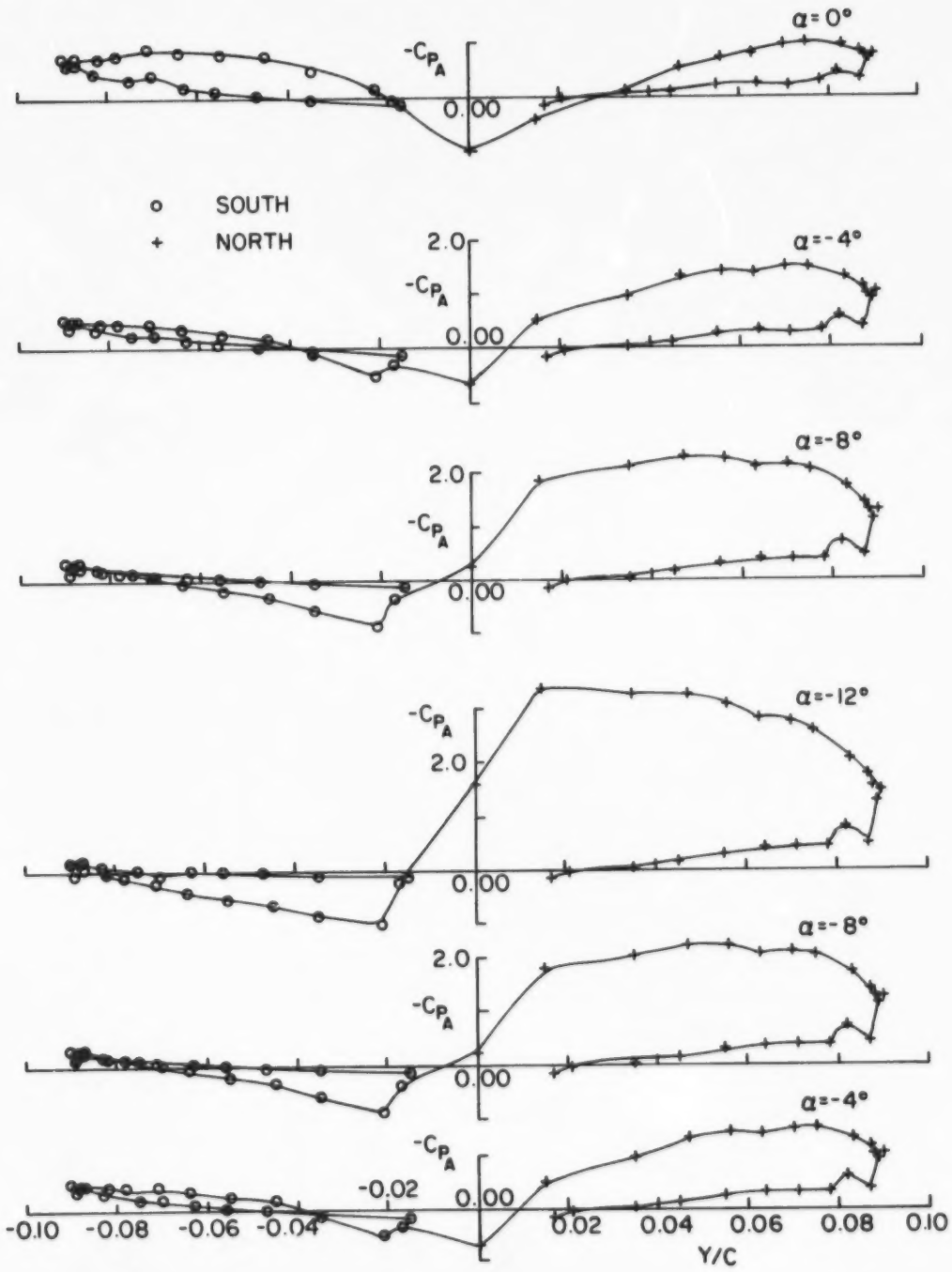

FIG. 18b: WING THICKNESSWISE PRESSURES DURING NEGATIVE HALF-CYCLE, $\alpha_m = \pm 12°$, $\frac{R\Omega}{V} = 5$, f = 0.55 hz

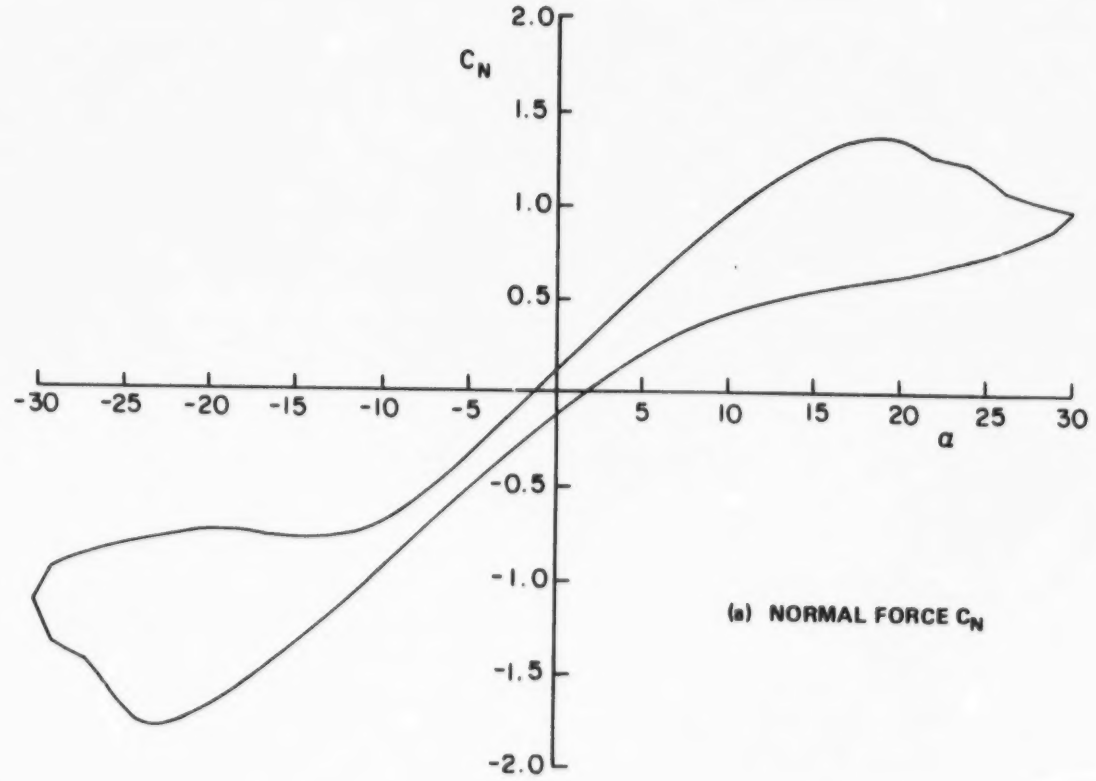

(a) NORMAL FORCE C_N

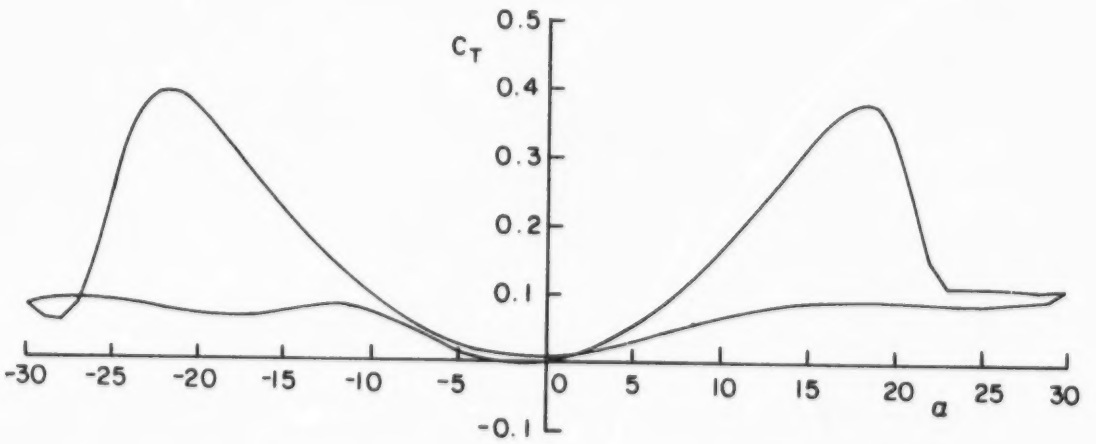

(b) CHORD FORCE C_T

FIG. 19: AIRFOIL FORCE COEFFICIENTS C_N, C_T, DERIVED FROM PRESSURE DISTRIBUTIONS $\frac{V_T}{V} = 2.0, \alpha max = \pm 30°, f = 0.55$ hz

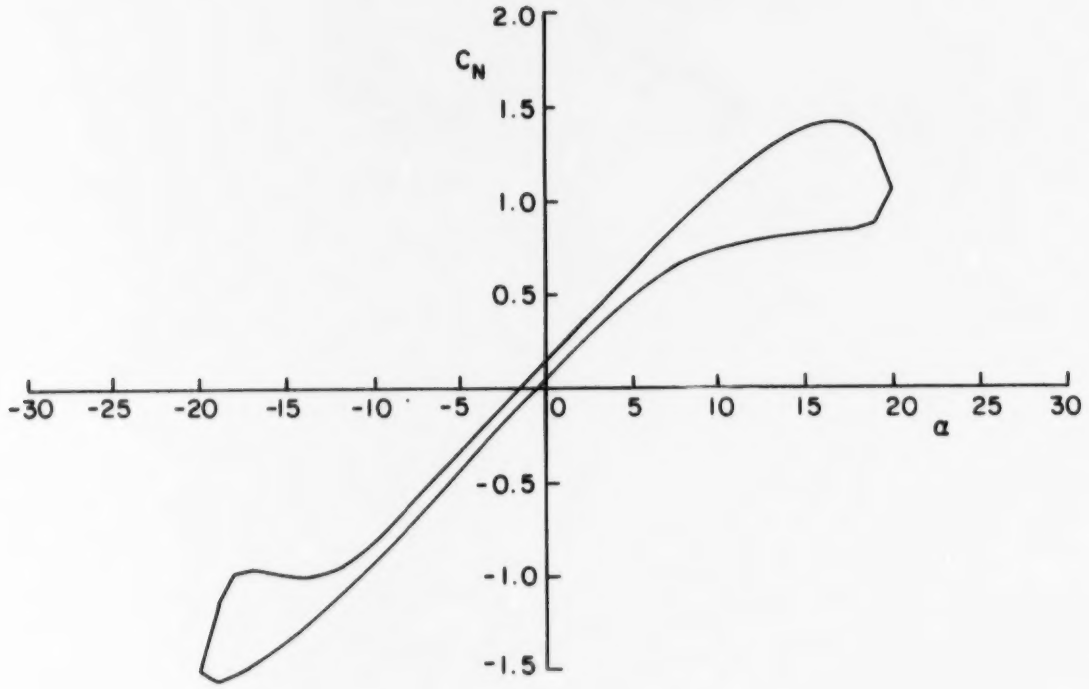

(a) NORMAL FORCE C_N

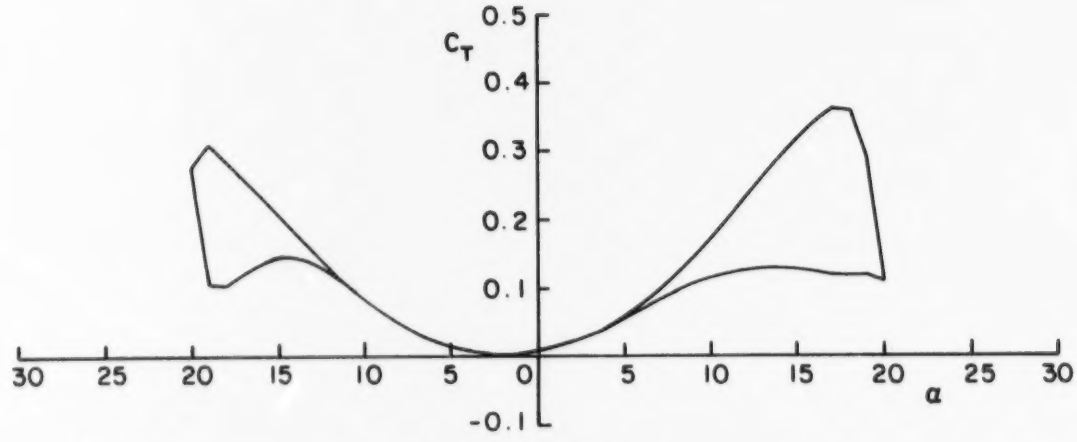

(b) CHORD FORCE C_T

FIG. 20: AIRFOIL FORCE COEFFICIENTS C_N, C_T, DERIVED FROM PRESSURE DISTRIBUTIONS $\frac{V_T}{V} = 3.0$, $\alpha max = \pm 20°$, f = 0.55 hz

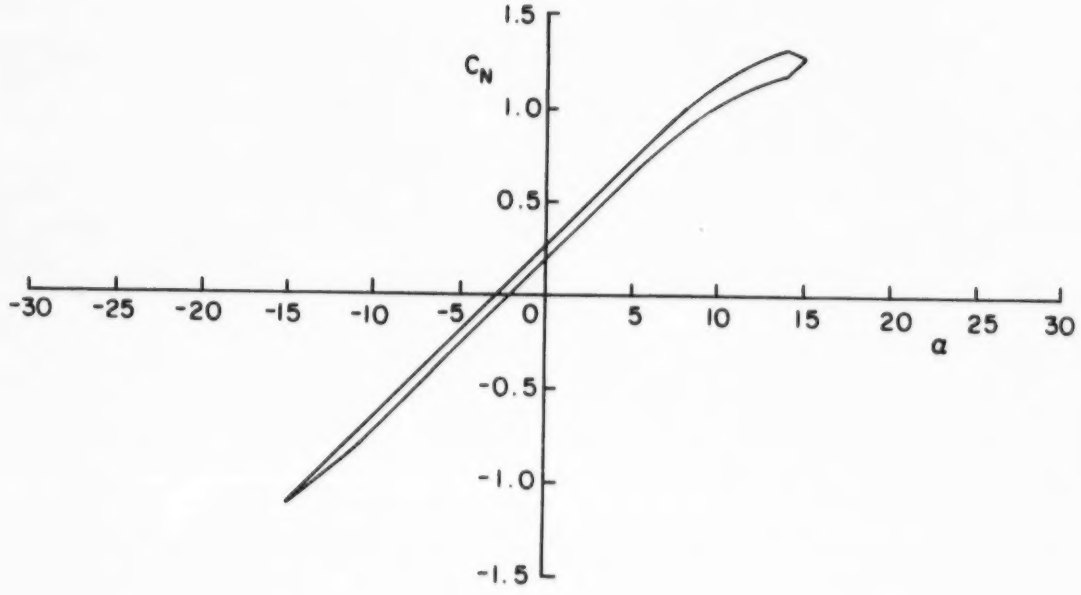

(a) NORMAL FORCE C_N

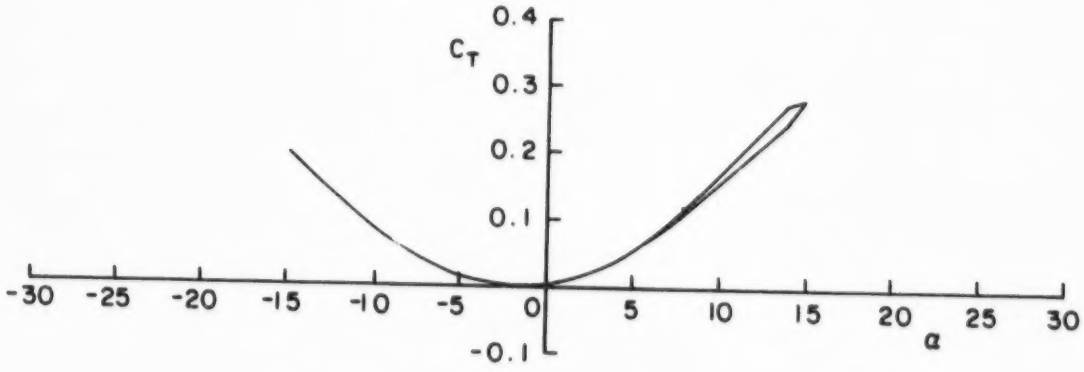

(b) CHORD FORCE C_T

FIG. 21: AIRFOIL FORCE COEFFICIENTS C_N, C_T, DERIVED FROM PRESSURE DISTRIBUTIONS $\frac{V_T}{V} = 4.0, \alpha max = \pm 15°, f = 0.55$ hz

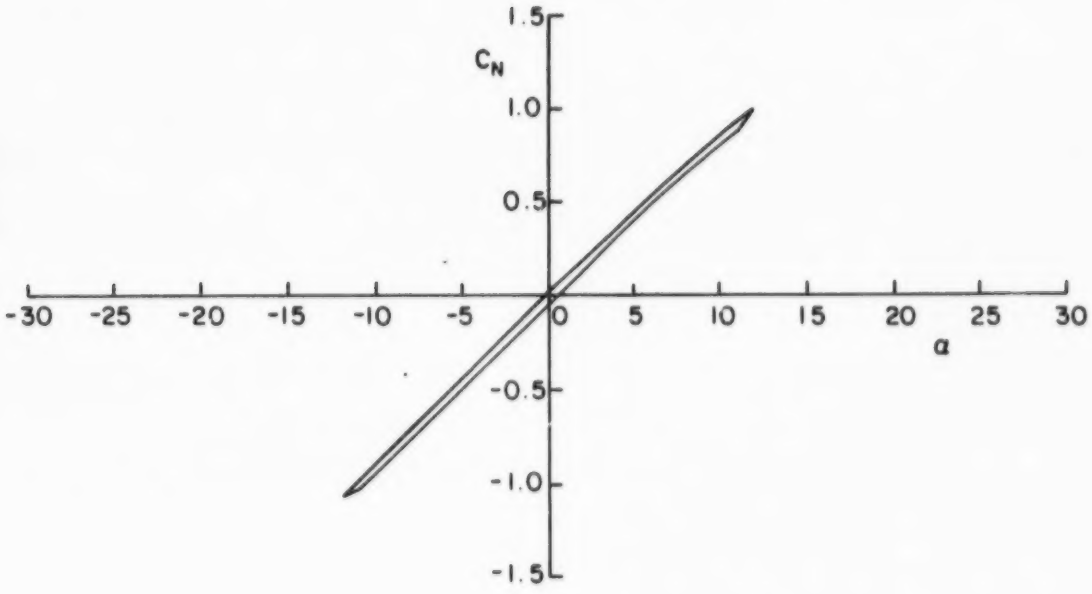

(a) NORMAL FORCE C_N

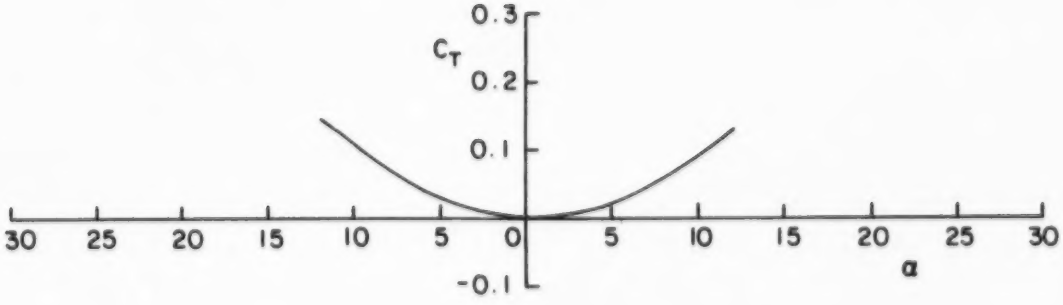

(b) CHORD FORCE C_T

FIG. 22: AIRFOIL FORCE COEFFICIENTS C_N, C_T, DERIVED FROM PRESSURE DISTRIBUTIONS $\frac{V_T}{V} = 5.0, \alpha max = \pm 15^\circ, f = 0.55$ hz

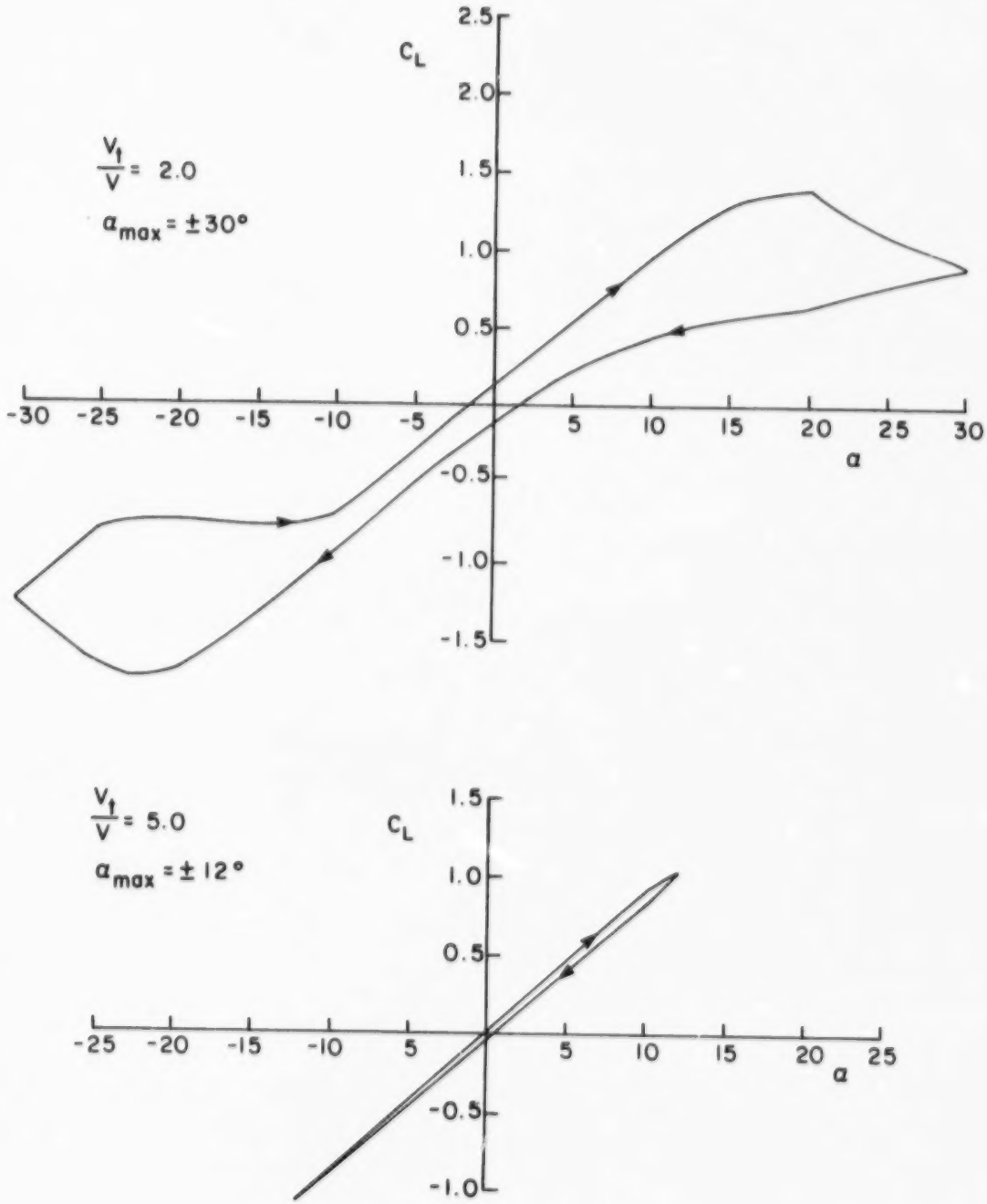

FIG. 23: OSCILLATING AIRFOIL LIFT COEFFICIENT C_L

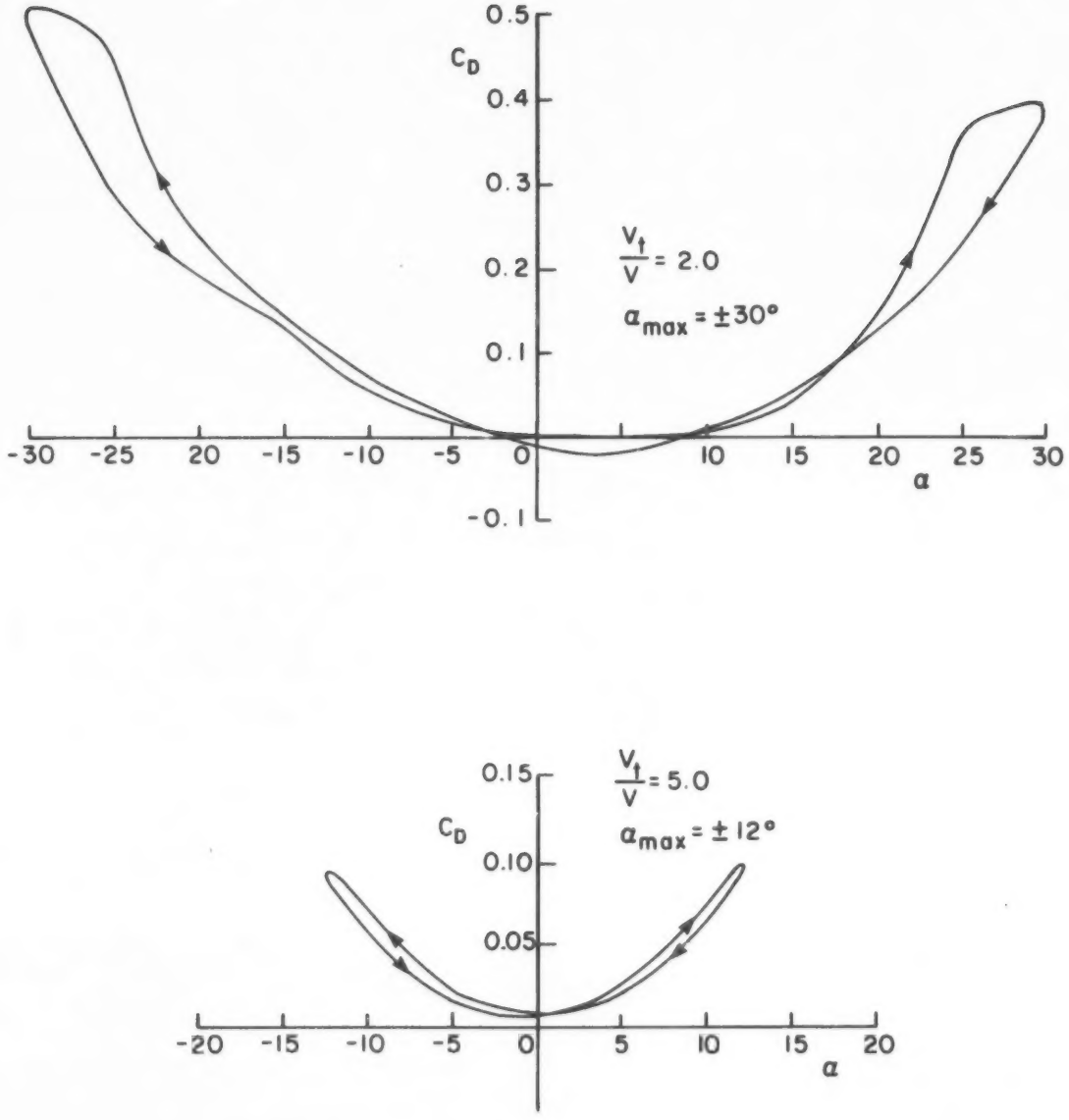

FIG. 24: OSCILLATING AIRFOIL DRAG COEFFICIENT C_D

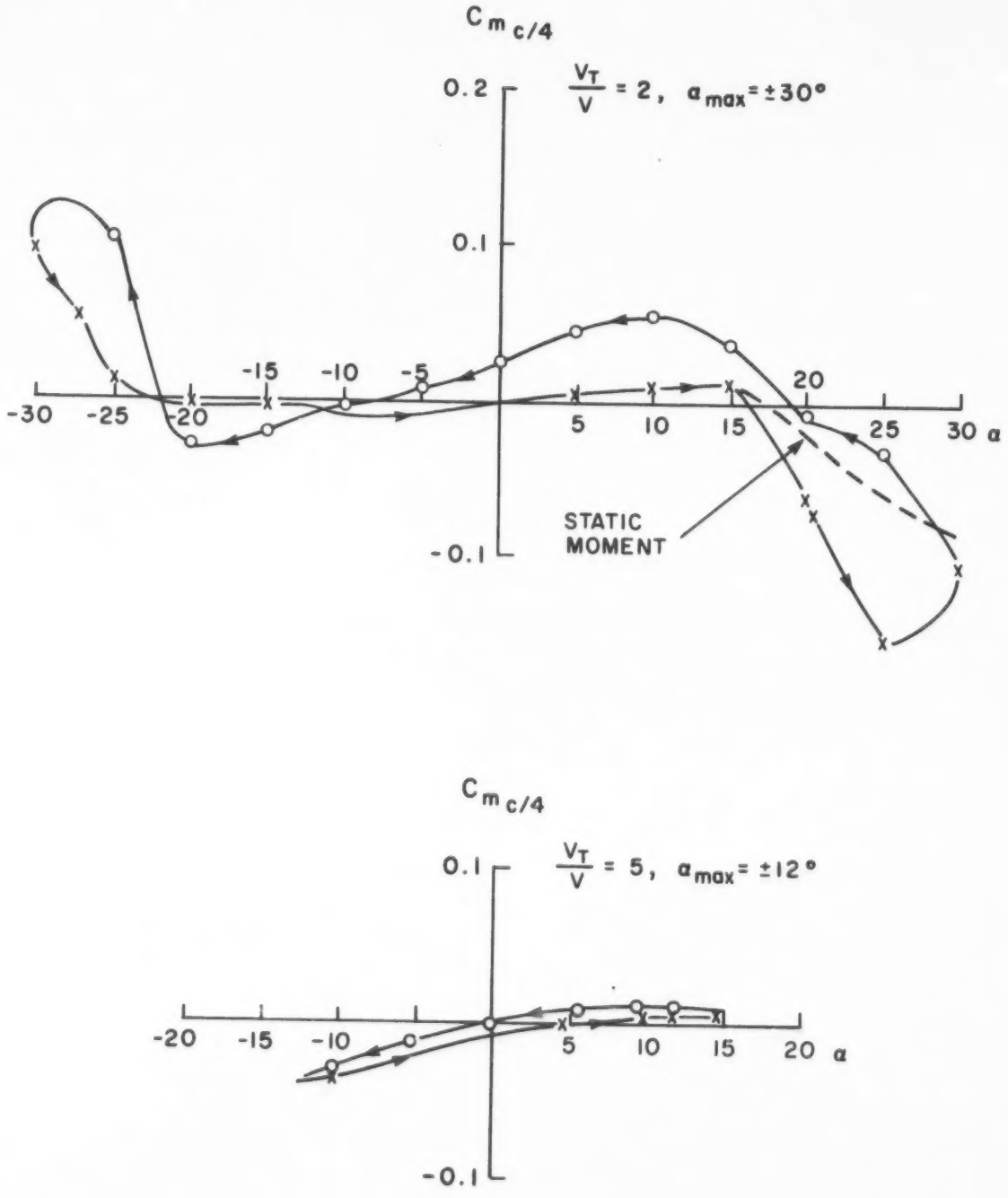

FIG. 25: PITCHING MOMENT COEFFICIENT ABOUT QUARTER-CHORD

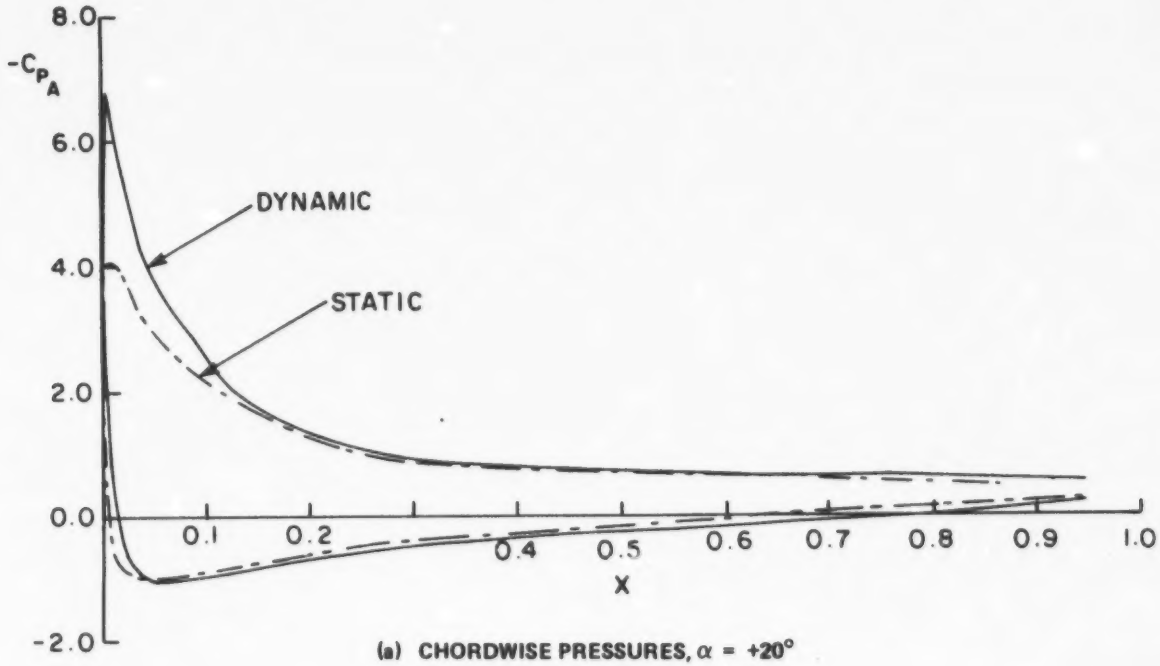

(a) CHORDWISE PRESSURES, α = +20°

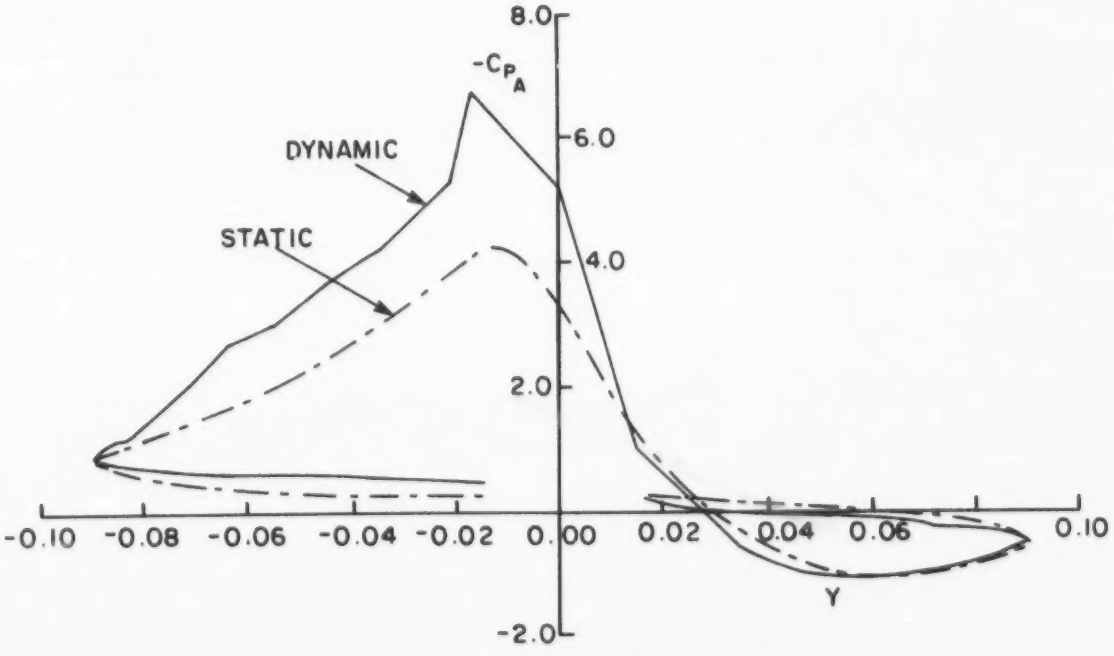

(b) THICKNESSWISE PRESSURES, α = +20°

FIG. 26: COMPARISON BETWEEN STATIC AND DYNAMIC WING PRESSURE DISTRIBUTIONS $\frac{V_T}{V}$ = 2.0, αmax = ±30°

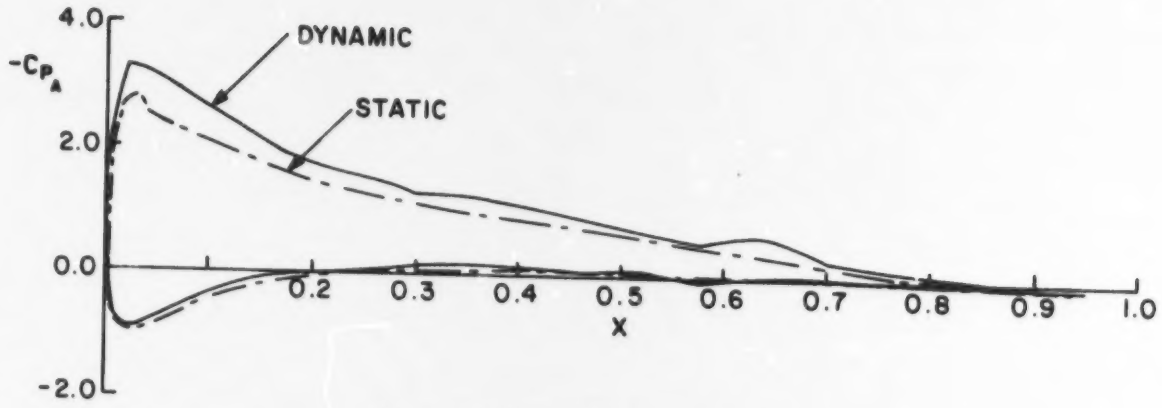

(a) CHORDWISE PRESSURES, α = 12°

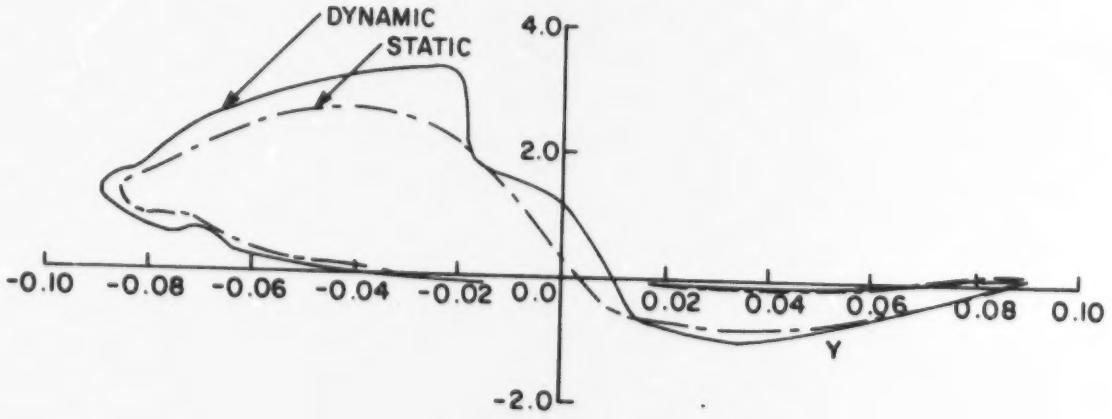

(b) THICKNESSWISE PRESSURES, α = 12°

FIG. 27: COMPARISON BETWEEN STATIC AND DYNAMIC WING PRESSURE DISTRIBUTIONS $\frac{V_T}{V}$ = 5.0, α_{max} = ±12°

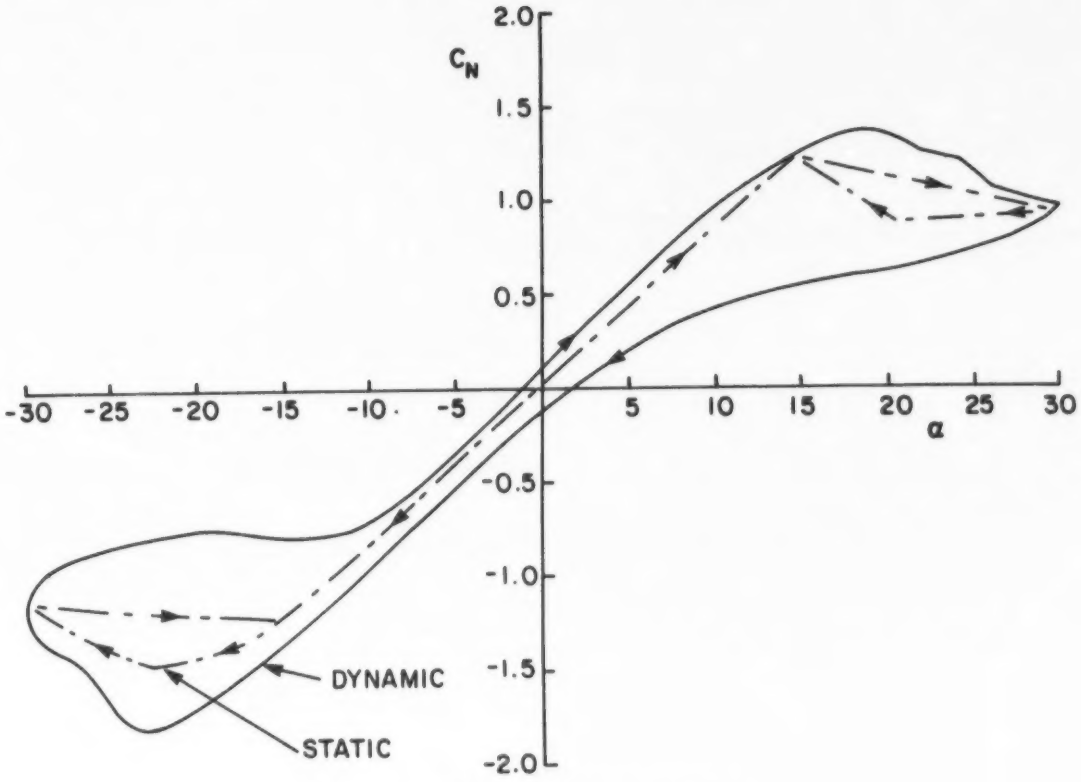

(a) NORMAL FORCE COEFFICIENT, C_N

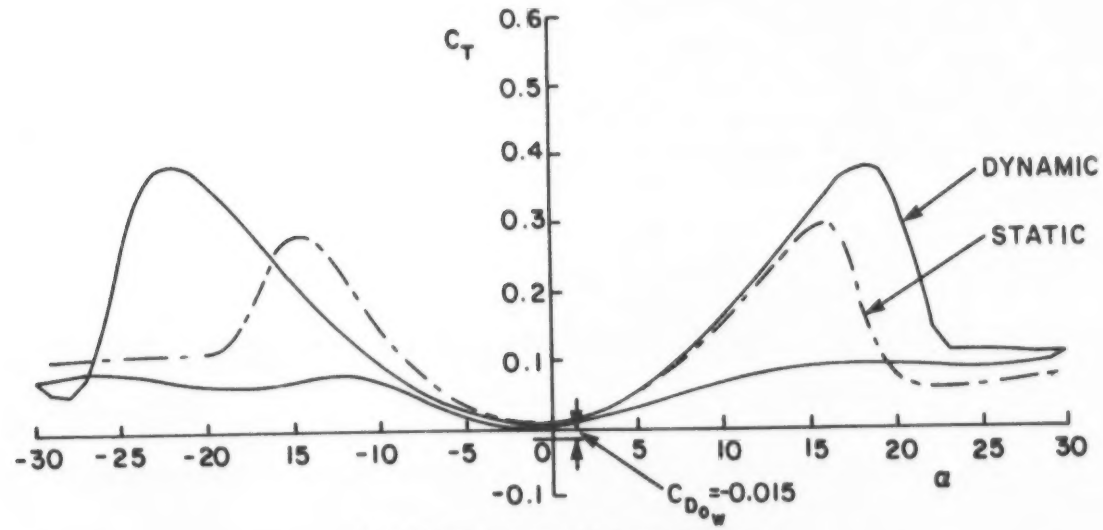

(b) CHORD FORCE COEFFICIENT, C_T

FIG. 28: COMPARISON BETWEEN STATIC AND DYNAMIC WING NORMAL AND CHORD FORCE COEFFICIENTS C_N, C_T, $\frac{V_T}{V}$ = 2.0, α_{max} = ±30°

REPORT DOCUMENTATION PAGE / PAGE DE DOCUMENTATION DE RAPPORT

REPORT/RAPPORT 1a NAE-AN-27	REPORT/RAPPORT 1b NRC No. 24262
REPORT SECURITY CLASSIFICATION CLASSIFICATION DE SÉCURITÉ DE RAPPORT 2 Unclassified	DISTRIBUTION (LIMITATIONS) 3 Unlimited

TITLE/SUBTITLE/TITRE/SOUS-TITRE

4 Wind Tunnel Investigation of Dynamic Stall of an NACA 0018 Airfoil Oscillating in Pitch

AUTHOR(S)/AUTEUR(S)

5 R.H. Wickens

SERIES/SÉRIE

6 Aeronautical Note

CORPORATE AUTHOR/PERFORMING AGENCY/AUTEUR D'ENTREPRISE/AGENCE D'EXÉCUTION

7 National Research Council Canada
National Aeronautical Establishment — Low Speed Aerodynamics Laboratory

SPONSORING AGENCY/AGENCE DE SUBVENTION

8

DATE 9 85-02	FILE/DOSSIER 10	LAB. ORDER COMMANDE DU LAB. 11	PAGES 12a 69	FIGS/DIAGRAMMES 12b 28

NOTES

13

DESCRIPTORS (KEY WORDS)/MOTS-CLÉS

14
1. Aerofoils — wind tunnel testing
2. Aerofoils — oscillations
3. Turbine blades — aerodynamic characteristics
4. NACA 0018 airfoil

SUMMARY/SOMMAIRE

15

This report presents aerodynamic data on an NACA 0018 airfoil oscillating in pitch in the NAE 2m X 3m Low Speed Tunnel. The purpose of the test was to simulate the dynamic aerodynamic behaviour of a Vertical Axis Wind Turbine blade section at the equatorial plane under the dynamic stall conditions which may occur at low ratios of tip speed to wind speed.

Measurements were made of wing surface pressure time histories at various chordwise locations, during a complete cycle of oscillation. The dynamic effects on nose suction pressures were seen to increase their magnitude and to delay flow breakdown to a higher angle of attack.

Integration of wing pressures furnished normal and chordwise forces during the angle of attack cycle. The behaviour of these parameters showed that dynamic stall for wing angles of attack up to 30 degrees, occurred about 5 degrees later than for the equivalent steady flow case. This phenomenon resulted in an increase in normal force of about 20% and an increase in chordwise force of about 40% when the wing is pitching to 30 degrees.